

June 2017

Vol. 10 No. 1
ISSN 2005-9043

Technical Reviews

Bio / Medical

Chemical and Structural Modifications of
RNAi Therapeutics

Materials / Systems

Highly Conductive 2D Layered
Materials for Electromagnetic
Interference Shielding

Energy / Environment

Improving the Performance and
Stability of Flexible Planar-Heterojunction
Perovskite Solar Cells
Using Polymeric Hole-Transport Material



Contents

Foreword	03
Bio / Medical	
Technical Review	
Chemical and Structural Modifications of RNAi Therapeutics	04
Feature Articles	
Approximating Bone ECM: Crosslinking Directs Individual and Coupled Osteoblast/Osteoclast Behavior	21
Improvement of the Sensitivity in Bead-Based Electrochemical Impedance Spectroscopy (BEIS) Biosensor Using Microwells	30
Materials / Systems	
Technical Review	
Highly Conductive 2D Layered Materials for Electromagnetic Interference Shielding	39
Feature Articles	
A Disordered Array of Plasmonic Metal Nanoparticles for Strong Upconversion Luminescence and Highly-Sensitive Near-Infrared Photodetector	47
An Alternative Patterning Process for the Realization of Large-Area, Full-Color, Active Quantum Dot Displays	52
Energy / Environment	
Technical Review	
Improving the Performance and Stability of Flexible Planar-Heterojunction Perovskite Solar Cells Using Polymeric Hole-Transport Material	57
Feature Articles	
Potential Risks of TiO ₂ and ZnO Nanoparticles Released from Sunscreens into Outdoor Swimming Pools	66
Ion Conducting Nafion Membranes with a Porous Structure	71
Research Highlights	
Recent Publications	77
New Patents	80
KIST News	83
A Sign of the Times	87
Interview	92
About the Cover	97

Foreword

Scientific circles throughout the world are busy preparing for a new industrial revolution. The concept of a Fourth Industrial Revolution, first promulgated by the founder of the World Economic Forum, is that new technologies will change the way we live by integrating the physical, digital and biological worlds. This revolution coincides perfectly with the new directions we are taking here at KIST at the start of our next 50 years.

Though now widely embraced in theory, the Fourth Industrial Revolution has prompted varying responses in different parts of the world. In the West, the focus has been on the resurrection of manufacturing industries. For example, Germany's basic strategy is to bring factories currently scattered throughout the world back to Germany and accomplish an industrial revival by using "smart factories" to modernize production. China is preparing by developing new industries. It recognizes the new industrial revolution as an opportunity to improve its competitiveness across all industrial sectors but is focusing investment in certain key areas such as biosciences, agriculture, natural resources, and energy. Other Asian countries, including Korea and Japan, are more focused on artificial intelligence and robotic science.

KIST has positioned itself well to take advantage of the opportunities inherent in the Fourth Industrial Revolution. It is actively engaged in convergence studies spanning various important fields. This research ranges from robotics to new materials, as well as artificial intelligence involving artificial neuromorphic semiconductors and quantum computing. Of course, energy will be at the heart of many of the new technologies, so the institute is continuing to develop innovative power sources through advancements in battery and alternative energy technologies.

This issue of *KISToday* reflects the impressive scope of our work in areas that are an integral part of the new industrial revolution. Whether it be a new material to make electronic devices safer, new ways to grow bone, or new systems to improve farm productivity, our scientists are at the front and center of scientific advances that will dramatically change the way we live.

Dr. Byung Gwon LEE
President of KIST



Chemical and Structural Modifications of RNAi Therapeutics



Sun Hwa KIM
Center for Theragnosis,
Biomedical Research
Institute
sunkim@kist.re.kr

Introduction

RNA interference (RNAi) is a highly potent and specific gene suppression process at the post-transcriptional level [1, 2]. Short double-stranded RNA, referred to as small interfering RNA (siRNA), is responsible for RNAi-based gene silencing. When siRNA is generated through endogenous intracellular Dicer processing of long double-stranded RNA, or synthetic siRNA is delivered into a cytoplasmic region, it is incorporated into RNA-induced silencing complex (RISC) machinery and then degrades the sense (passenger) strand. The activated RISC recognizes specific target mRNA by complementary sequence and cleaves the target mRNA at the opposite of position 10 from the 5' end of the antisense (guide) strand [3]. siRNA is considered a next-generation drug because it can suppress the expression of virtually all genes with high specificity, including previously undruggable targets. Over the last few decades, the therapeutic potential of siRNA has been demonstrated for the treatment of genetic diseases, viral infections, and cancer [4, 5].

Numerous RNAi-based drugs, in the form of naked siRNA and siRNA with delivery vehicles, have been undergoing clinical trials for the treatment of various diseases (Table 1). However, most of them are still in the Phase I testing process (safety testing), and very few have entered or are scheduled to enter Phase II/III (efficacy testing). The development of RNAi therapeutics still suffers from practical problems, such as the easy degradation of siRNA *in vivo*, unwanted off-target effects, and

Table 1 Clinical trials of RNAi therapeutics.

Drug name	Target sequence	Target disease	Phase	Status	Company
Atu027	PKN3	Advanced solid tumors	I	Completed	Silence Therapeutics GmbH
15NP	P53	Acute renal failure	I	Completed	Quark Pharmaceuticals
TD101	Keratin6A	Pachyonychia congenita	I	Completed	Pachyonychia Congenita Project
siG12D LODER	KRAS	Pancreatic tumor	I	Completed	Silenseed Ltd.
CALAA-01	RRM2	Solid tumor	I	Terminated	Calando Pharmaceuticals
TKM-PLK1	PKL1	Hepatic metastases	I	Completed	Tekmira Pharmaceuticals Corporation
TKM-ApoB	ApoB	Hyper-cholesterolemia	I	Terminated	Tekmira Pharmaceuticals Corporation
ALN-VSP02	VEGF, KSP	Solid tumor	I	Completed	Alnylam Pharmaceuticals
siRNA-EphA2-DOPC	EphA2	Advanced cancers	I/II	Not yet recruiting	M.D. Anderson Cancer Center
EZN-2968	HIF-1	Liver metastases	I	Completed	Sataris Pharma and Enzon Pharmaceuticals
AGN 211745	VEGF	Age-related macular degeneration	I/II	Completed	Allergan
PF-04523655	PTP-801	Choroidal neovascularization, Diabetic macular edema	II	Completed	Quark Pharmaceuticals
Bevasiranib	VEGF	Age-related macular degeneration	III	Withdrawn	OPKO Health, Inc.

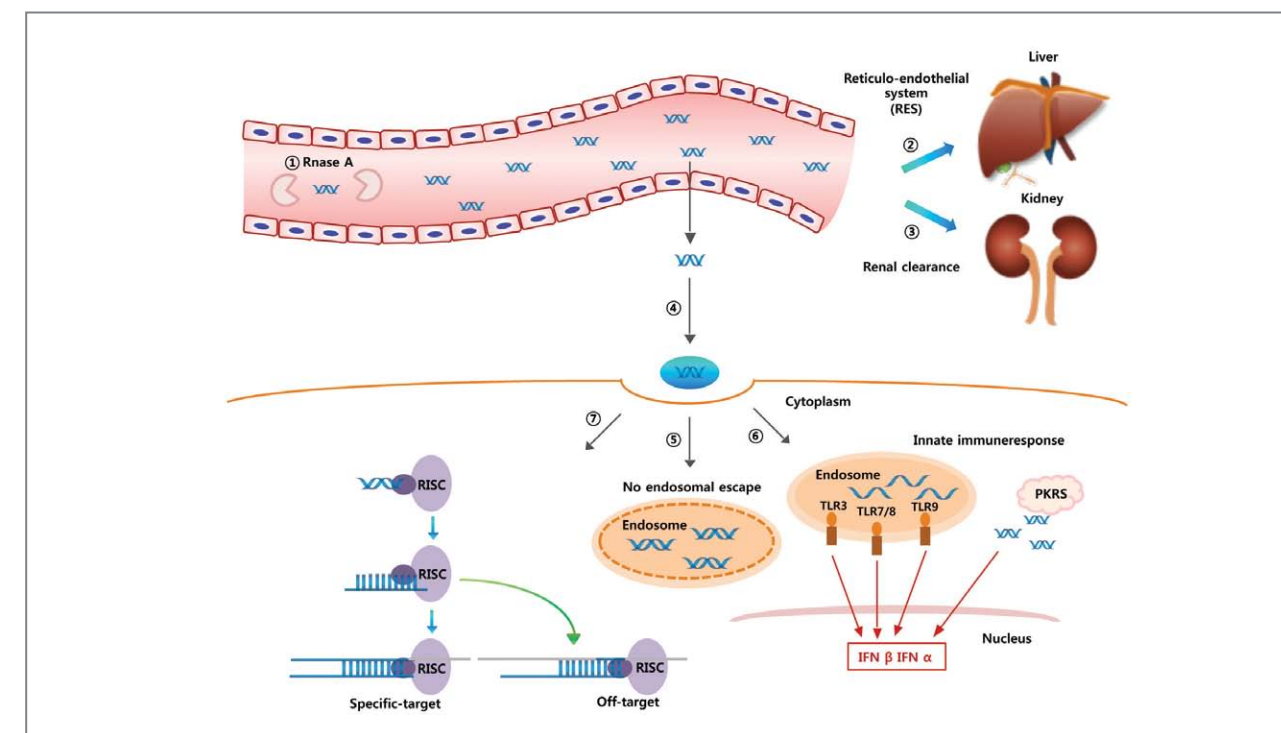


Figure 1 Inherent problems and delivery barriers of synthetic siRNA *in vivo*. ① siRNAs are influenced by enzymatic degradation in the blood system. Also, siRNAs can be rapidly eliminated from circulating blood by ② the reticuloendothelial system (RES) and ③ renal clearance. In the siRNA delivery system, current drawbacks include: ④ poor transport across cell membranes and ⑤ endosomal entrapment. ⑥ siRNAs trapped in endosome can induce unwanted TLR-mediated immune responses, and external cytoplasmic RNAs can activate immune cells through PKRS. Finally, ⑦ siRNA can cause off-targeting mRNA degradation, leading to unintended transcription and translation suppression.

immunogenicity [6]. The effective delivery of siRNAs to target tissues and cells is also a critical problem. To overcome these issues, structural and chemical modification of siRNA itself, as well as the development of efficient delivery systems, are considered promising strategies.

Challenges in the clinical translation of RNAi therapeutics

The inherent problems associated with the clinical potential of siRNA fall mainly into three categories: *in vivo* instability, off-target effects, and immunogenicity (Figure 1). These shortcomings reduce the therapeutic efficacy of siRNA therapeutics and induce unwanted side effects.

The easy enzymatic degradation of siRNA from *in vivo* body fluids is considered a major obstacle to its clinical application. Due to its vulnerability to nuclease degradation, native siRNA has a short half-life of less than ~15 min in serum. To improve serum stability, siRNA can be chemically modified to prevent enzymatic degradation. Alternatively, the use of gene carriers can prevent the access of nucleases to siRNA, subsequently leading to enhanced stability.

It has been reported that synthetic siRNA can induce unwanted gene silencing, referred to as off-target effects, through two types of pathways: (1) miRNA-like pathways and (2) sense strand-mediated pathways. miRNA naturally suppresses the translation of mRNA through binding to the 3'-untranslated region (UTR) of the target mRNA with partial homology [7]. Similarly, the siRNA antisense strand can interact with the 3'-UTR of mRNA with partial homology. Translational inhibition by siRNA occurs from imperfect matching with the 3'-UTR rather than mRNA degradation by Argonaute-2 and consequently leads to suppression of unintended genes. The sense strand of siRNA can participate in the gene silencing process instead of the antisense strand [8]. Incorporation of the sense strand in RISC can cause down-regulation of unwanted gene expressions. The

preferential loading of the antisense strand in RISC via chemical/structural modification can circumvent this type of off-target effect.

The innate immune response to exogenous double stranded RNA is categorized as Toll-like receptor (TLR)-mediated and non-TLR-mediated immune responses. Three types of TLR (TLR3, TLR7, and TLR8) among 13 TLRs are involved in TLR-mediated immune reactions. TLR3 shows length-dependent activity [9]; dsRNAs longer than 21-23nt can stimulate a TLR-mediated immune response, though the length threshold is dependent on cell type. TLR7 and TLR8 sense the nucleotide sequence; both of them are stimulated by GU-rich motifs, whereas AU-rich motifs primarily activate TLR8. The latter group of immune responses includes the activation of dsRNA-dependent protein kinase R (PKR) and retinoic acid inducible protein (RIG-1). PKR is activated by dsRNA longer than 30 bp in a sequence-independent manner. The activation of RIG-1 is not sequence-specific but length-dependent [10]. Further, the siRNA overhang can reduce the RIG-1-mediated immune response. The modification of TLR-activatable motifs or the alteration of the interactions between RNA and immune-related proteins has been proposed as a potential strategy to avoid siRNA-triggered immune reactions.

In order to play a role as a therapeutic agent, siRNA should be delivered to target tissue, be internalized into specific cell types, and be placed at the cytosol. However, effective siRNA delivery has been undermined by short blood circulation time, lack of target specificity, and difficulty in cellular uptake. Endosomal escape is also a significant barrier to siRNA delivery (Figure 1).

Short blood circulation time may be caused by enzymatic degradation, renal clearance, or capture by the reticuloendothelial system (RES). The rapid renal clearance of naked siRNA occurs upon systemic administration because small molecules less than 50 kDa are excreted through the kidneys [11]. Phagocytic cells in RES also contribute to the removal of foreign nucleic acids as well as gene carriers [12]. The pharmacokinetics of siRNA can be improved by chemical modification of siRNA itself through inhibition of enzymatic degradation

and incorporation with efficient delivery vehicles by protecting siRNA from nuclease attack and preventing renal clearance and phagocytosis in RES.

Many researchers have investigated the introduction of nanovehicle systems, specific cell targeting molecules, or both, to siRNA as a way to efficiently deliver it to targeted tissue. When siRNA is transported by nanocarriers, the resulting nanoparticles can accumulate in tumor tissues through immature leaky blood vessels. Inefficient lymphatic drainage in tumor tissues also accounts for the prolonged retention of nanovehicles; this is referred to as enhanced permeability and retention (EPR) effects [13]. By taking advantage of EPR effects, siRNA nanocarriers can be selectively delivered to tumor tissues. The incorporation of targeting molecules, such as antibodies, aptamers, and ligands for cell surface receptors, enables the recognition of specific types of cells [14].

The intracellular entrance of siRNA is hampered by its large size (~15 kDa) and high negative charge [11]. Positively charged carriers help not only nanosized particle formation but also the crossing of the negatively charged cell membrane. The introduction of receptor-binding ligands into siRNA or its carriers improves target specificity through receptor-mediated endocytosis. Cell penetrating peptides (CPPs) have also been widely used to enhance the cellular uptake of siRNA [15]. When siRNA is taken up by endocytosis, it needs to escape from the endosomes/lysosomes which contain nucleases in order to enter cytosol. Considering the acidic environment of late endosomes, siRNA carriers having pH-responsive proton sponge effects or membrane disruption activities can enhance the endosomal escape of siRNA [16].

The intrinsic problems and delivery issues described above can be partially overcome by chemical modification at a specific position or sequence of the nucleic acids and by structural alteration [17]. A variety of chemical modification strategies and siRNA structural variants have been developed and proven capable of improving serum stability, minimizing off-target effects, and reducing immune responses.

siRNA's delivery issues, such as short blood circulation time, lack of targeting moieties, and difficulty in subcellular localization, can be overcome by using effective carriers. The delivery vehicle can protect siRNA from nuclease attack and from detection by macrophages. Nanoparticle formation by gene carriers and the further introduction of targeting molecules can improve the delivery efficiency of siRNA into specific target tissues and cells. Gene carriers can be used in two ways: direct conjugation of the carrier with siRNA and complex formation between the carrier and siRNA. The former generally includes covalent linkage between siRNA and its carriers. Lipophilic molecules or polymers prolong the blood circulation of siRNA, and aptamers are used to provide targeting efficacy to siRNA. These latter groups used in siRNA delivery systems have been extensively focused on cationic carriers. Considering the stiff structure and low charge density of siRNA, however, it has been necessary to enhance its physicochemical properties in an effort to improve the interaction between siRNA and gene carriers; thus, various siRNA polymerization strategies have been proposed in the last decade.

Chemical modification of RNAi therapeutics

The most common backbone modification of siRNA is the substitution of non-bridging phosphate oxygen for sulfur (phosphorothioate, PS) (Figure 2). Previous reports have shown that PS modification of antisense oligonucleotides results in improved nuclease resistance and favorable pharmacokinetics [18]. Similarly, siRNA with PS modification has exhibited high serum stability and high blood concentration soon after injection [19]. Moderate PS modification of siRNA improved gene silencing activity, although the effects were highly position-dependent; PS modified siRNA at the positions of 3, 5, and 17 from the 5'-end of the sense strand showed high silencing effects by improving RISC loading of the antisense strand [20]. However, a high

degree of PS modification can lead to severe toxic effects, presumably attributable to the non-specific binding to cellular membrane proteins; siRNA with 50% PS content (PS modification in every second nucleotide) shows cytotoxicity and reduced cell growth [21]. The substitution of two non-bridging oxygen atoms with sulfurs, known as phosphodithioate (PS2), also results in enhanced serum stability and higher gene silencing activity in a position-dependent manner [22]. Alternative backbone modifications include boranophosphate substitution, obtained by introduction of BH₃ group in place of non-bridging phosphate oxygen. This modification thermodynamically destabilizes siRNA with the decrease of T_m (0.5-0.8°C per modification) [23]. Boranophosphate modification results in siRNA potency when the seed region of the antisense strand is not modified, leading to enhanced serum stability of siRNA [24].

Ribose 2'-OH is also an attractive modification site because 2'-OH is not necessary for recognition by RNAi machinery or for the mRNA cleavage process by activated RISC [25]. Chemical modification of ribose 2'-OH involves the substitution of 2'-OH with another

chemical group, such as 2'-O-methyl (2'-OMe), 2'-F, or 2'-H (Figure 2). 2'-OMe modification improves the resistance to enzymatic digestion and thermal stability (0.5-0.7°C increase in T_m per modification) [26]. When the antisense strand or both strands of siRNA are fully modified with 2'-OMe, the RNAi activity is completely abolished, whereas the same modification in the sense strand does not modulate the gene silencing efficacy [27]. In contrast, the substitution of 2'-OH with fluorine (2'-F) can be accepted in both antisense and sense strands without the loss of gene silencing activity [25, 28]. The 2'-F modification enhances serum stability as well as the binding affinity of siRNA duplex (~1°C increase in T_m per modification) [25, 29, 30]. 2'-H modification, DNA itself, is also well-tolerated in siRNA duplex, particularly in the sense strand and at the end region (3'-overhangs or 5'-end of the antisense strand) [31, 32].

An alternative strategy for the 2'-OH modification is the intramolecular linkage of 2'-oxygen to 4'-carbon. The bridged nucleic acids contain the linkage between the 2' and 4' positions of the ribose ring via the methylene bridge (locked nucleic acid, LNA) or ethylene bridge (ethylene-bridged nucleic acid, ENA) (Figure 2). LNA modification locks the sugar ring in 3'-endo conformation, which increases in T_m by 2-10°C per modification [33]. Furthermore, this modification is highly position-sensitive; the introduction of LNA modification at the 10, 12, and 14 positions of the antisense strand abolishes RNAi activity due to the steric and conformational change near the cleavage site [34]. LNA modifications at the 3'-overhangs protect siRNA from the 3' exonucleases, subsequently leading to improved serum stability [34].

The chemical modifications described above can be used to make siRNA more suitable for clinical applications. Considering that several nucleases catalyze the nucleophilic attack of 2'-OH and the hydrolysis of the inter-phosphate linkage in siRNA, modification of the ribose 2'-OH position improves serum stability. In particular, 2'-OMe and 2'-F modification of nuclease-sensitive regions, such as UA and CA motifs, dramatically enhances resistance to nuclease digestion

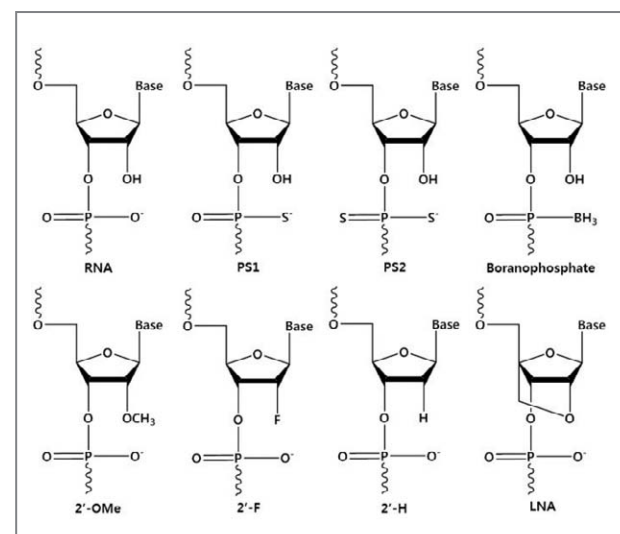


Figure 2 Popular chemical modifications of siRNA. RNA, ribonucleic acid; PS1, Phosphothioate; PS2, Phosphodithioate; 2'-OMe, 2'-O-methyl; 2'-F, 2'-fluoro; 2'-H, 2'-deoxy; and LNA, locked nucleic acid.

[26, 35, 36]. The combination of different modification strategies results in highly stable siRNA *in vivo*. Successful examples include modified siRNA consisting of sense strand with 2'-F on pyrimidine, 2'-H on purines, and 5' and 3'-inverted abasic end caps, and antisense strand with 2'-OMe on purines and PS at the 3'-terminus [37]. The 3'-overhangs are also susceptible to exonuclease attack, but by chemically modifying the 2nt 3'-overhangs, for example by using LNA modification, siRNA degradation in serum can be reduced [34].

Off-target effects of siRNA via miRNA-like pathways are dependent on seed region homology with the 3'-UTR of mRNA. Although *in silico* siRNA-mRNA sequence matching prediction may reduce this type of off-target effect, it cannot be fully avoided. According to published literature, chemical modification of the antisense strand modulates undesired gene silencing effects; 2'-OMe modification at position 2 of the antisense strand and introduction of 8 DNA in the antisense strand seed region reduces the down-regulation of non-target gene expression [38, 39]. An increase in the incorporation selectivity of antisense strand into RISC can modulate off-target effects resulting from the contribution of the sense strand in the gene silencing process. Considering that phosphorylation of the 5'-terminus is required for RISC activation, the 5'-end modification of the sense strand via 5'-OMe or LNA reduces its participation in the RNAi mechanism [40, 41].

Exogenous RNA molecules can elicit immune responses mediated by the TLR family or PKR, and these exogenous siRNA-triggered immune responses can be reduced or eliminated by applying several modification strategies. Concerning the incorporation of U-rich motif in TLR activation, modification at the ribose 2'-OH position of uridine residue minimizes siRNA immunogenicity [42]. Introduction of alternating 2'-OMe modification in the sense strand reduces cytokine induction without loss of gene silencing activity [43]. LNA modification of the sense strand also blocks TLR activation [44]. The activation of cytoplasmic PKR after intracellular delivery of siRNA can be abrogated by the reduction of hydrogen bonding between the RNA

minor groove and PKR domain; chemical modification for hydrogen bonding alteration, such as 2'-H or 2'-F modification, reduces PKR activation [45].

Structural variants of RNAi therapeutics

Many different structural variants of RNAi-based therapeutics have been reported to improve the intrinsic properties of siRNAs. This suggests that the natural RNAi pathway machinery can tolerate various structurally different siRNA variants. The first successful sequence-specific gene silencing using chemically synthesized exogenous siRNA in mammalian cells was demonstrated by Tuschl and colleagues without causing innate immune responses [46, 47]. The siRNA has a 19 base paired duplex with 3'-end 2nt overhangs at both sense and antisense strands (19 + 2 traditional siRNA) and is the most widely used structural form of siRNA (Figure 3A). The 19 + 2 siRNA has a structural similarity to nature's endogenous Dicer product.

Designing highly potent gene-suppressing RNAi triggers is an important strategy for successful clinical application of RNAi therapeutics. In efforts to find RNAi triggers that work efficiently at low concentrations, Dicer substrates were found by two groups. Kim et al. found that long synthetic 27-mer duplex RNA without overhangs can be substantially more efficient in gene silencing than the corresponding traditional 21-mer siRNA (Figure 3B) [48]. Siolas et al. also identified a synthetic short hairpin RNA (shRNA) as a potent mediator of RNAi (Figure 3C) [49]. These shRNAs are composed of 29 base-paired stems with 2nt 3'-overhangs and 4nt loops. Both 27-mer RNA duplex and 29-mer shRNA were processed to 21- or 22-mer siRNA by Dicer *in vitro*. It was reported that Dicer is involved in not only cleaving long double stranded RNAs but also RISC loading of processed RNA and RICS assembly [50, 51]. The improved potency of these RNAi triggers may be attributed to the fact that they are Dicer substrates. Dicer processing may enhance the loading and incorporation

of siRNA into RISC, thereby increasing gene silencing efficiency. Furthermore, the Dicer-substrate RNA did not induce innate immune responses, such as interferon production and PKR activation.

It has been reported that an exogenously introduced high concentration of siRNA can cause a saturation of cellular RNAi proteins, which would hinder the endogenous RNAi pathway and cause toxicity. In addition, the extent of unwanted off-target effects are proportional to the siRNA treatment concentration [52]. Therefore, these highly potent mediators of gene silencing can facilitate the clinical use of RNAi therapeutics.

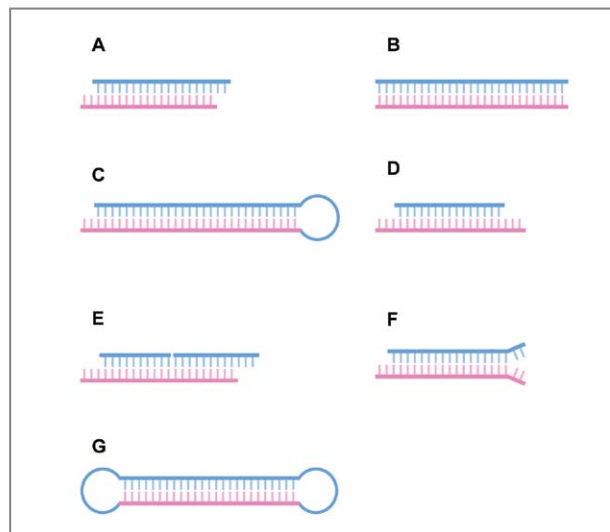


Figure 3 Schematic diagrams of structural variants of siRNA. (A) Conventional siRNA of 19+2. (B) 27-mer long dsRNA Dicer substrate. (C) 29-mer short hairpin RNA (D) Asymmetric siRNA. (E) Internally segmented siRNA. (F) Fork-shaped siRNA. (G) Dumbbell-shaped circular RNA.

Incorporation of sense strand into RISC is one of the main undesired off-targeting effects of RNAi-based therapeutics [53]. Novel designs of siRNA structural variants to reduce off-target effects have been suggested by Sun et al. [54]. They investigated whether asymmetric RNA duplexes with various lengths could induce gene silencing and found that asymmetric RNA duplexes with a short 15nt sense strand having both 3' and 5' antisense

overhangs could mediate gene silencing (Figure 3D). The asymmetric interfering RNA (aiRNA) was incorporated into RISC effectively and inhibited target gene expression sequences specifically. More importantly, the sense strand mediated off-target effects were reduced compared with conventional siRNAs, which may be attributed to the nature of the structural asymmetry. They speculated that the asymmetric structure leads to preferential incorporation of antisense strand into RISC rather than short sense strand, which resulted in reduced sense strand mediated off-target effects.

Along with the aiRNA, a novel design of small internally segmented interfering RNA (sisiRNA) also showed decreased off-target effects caused by the loading of sense strand into RISC (Figure 3E) [55]. The sisiRNA had an intact antisense strand and a sense strand which was divided into two segments. Because incorporation of segmented sense strand into RISC was excluded and only antisense strand could be loaded into RISC, this structural siRNA variant showed reduced off-target effects and increased target specificity.

Fork-shaped siRNA having a 1 ~ 4nt mismatch at the 3'-end of the sense strand is another structure that has shown increased target specificity while maintaining gene silencing activity (Figure 3F) [56]. Reporting suggests that the mismatched part may make the antisense strand more favored for incorporation into RISC. Investigations demonstrated that the thermodynamically less stable 5'-end of siRNA is preferentially incorporated into RISC during strand selection [57, 58]. These reports show that structure-based asymmetry represents another way to reduce off-target effects in addition to the chemical modifications discussed earlier.

Natural RNAs rapidly degrade in biological fluid. Chemical modification can enhance siRNA stability, although it often causes toxicity or decreases gene silencing activity. A method to increase RNA stability using natural RNA was proposed by Abe et al. [59]. An additional loop was added into shRNA using T4 RNA ligase, which resulted in a dumbbell-shaped circular RNA structure (Figure 3G). Due to its endless structure, dumbbell-shaped RNA showed higher stability when

treated with exonuclease compared with the linear form of siRNA. In addition, the RNA dumbbell was processed more slowly and exhibited prolonged RNAi activity.

As evidenced by the reports discussed above, structural variants of siRNA can improve potency, reduce off-target effects, and increase stability, but more study of RNAi mechanisms is needed to optimize siRNA structure.

siRNA conjugate system

The introduction of lipophilic molecules, such as cholesterol and α -tocopherol, can improve the pharmacokinetic properties as well as cellular uptake of siRNA (Figure 4A) [60]. Cholesterol-conjugated siRNA (Chol-siRNA) exhibited prolonged blood circulation time ($t_{1/2}$ of 95 min) compared to naked siRNA ($t_{1/2}$ of 6 min) after systemic administration, presumably due to enhanced binding to serum proteins [61]. This enhanced pharmacokinetics resulted in the increase of specific gene

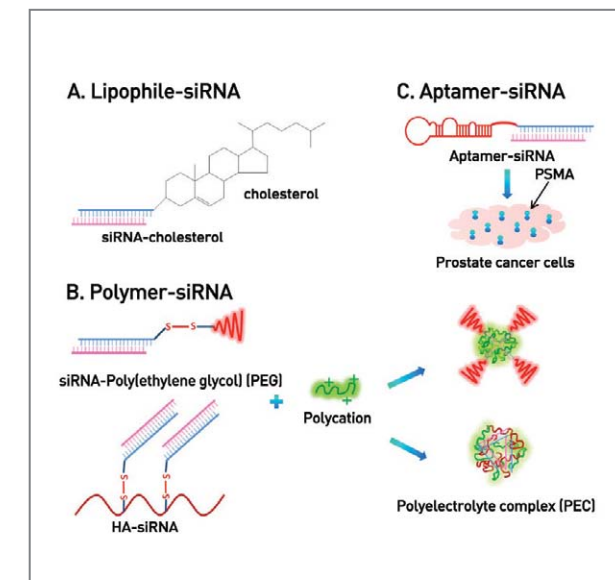


Figure 4 Schematic diagrams of siRNA conjugate system. (A) Cholesterol-siRNA conjugate. (B) Polymer-siRNA conjugate, containing bioreducible disulfide linkage. The polymer-siRNA conjugate can form a stable polyelectrolyte complex with polycation. (C) Aptamer-siRNA chimera. PSMA-specific A10 aptamer is linked to siRNA.

silencing efficacy; Chol-siRNA against apolipoprotein B (apoB) led to the down-regulation of the target mRNA in liver and jejunum and a decreased level of plasma apoB protein and serum cholesterol. Since lipoprotein particles, including both high-density lipoprotein (HDL) and low-density lipoprotein (LDL), play a critical role in cholesterol transport *in vivo*, the delivery of Chol-siRNA may be facilitated when Chol-siRNA is preassembled with HDL or LDL. In previous research, Chol-siRNA with HDL was delivered into liver, gut, kidney, and steroidogenic organs, whereas LDL directed the Chol-siRNA primarily into liver [62]. The binding with HDL or LDL further enhanced the cellular uptake of Chol-siRNA via the HDL- or LDL-receptor, respectively.

The conjugation of lipophilic molecules can be used as a targeting moiety for siRNA delivery to specific tissue. Considering that α -tocopherol (vitamin E) is incorporated into lipoproteins and travels into the liver for hepatic uptake, α -tocopherol-conjugated siRNA (Toc-siRNA) was delivered specifically into the liver [63]. Toc-siRNA targeting apoB achieved the reduction of liver apoB mRNA expression and serum triglyceride/cholesterol levels. Furthermore, neither interferon induction nor other side effects were observed after systemic administration of Toc-siRNA.

In order to avoid capture by RES, poly(ethylene glycol) (PEG) can be introduced to provide stealth effects, resulting in prolonged blood circulation time. The half-life of siRNA was increased from 5 min to 1 h after conjugation with 20kDa PEG, and the distribution of PEG-siRNA in liver, kidney, spleen, and lung was observed without significant degradation [64]. When PEG-siRNA conjugate was complexed with cationic polyethylenimine (PEI), negatively charged siRNA and positively charged PEI formed a nanosized polyelectrolyte core and hydrophilic PEG was present on the nanoparticle surface (Figure 4B) [65, 66]. The resultant PEG-siRNA/PEI nanocomplex exhibited enhanced serum stability and excellent tumor targeting efficacy without any induction of interferon. When siRNA targeting vascular endothelial growth factor (VEGF) was used, the local or systemic administration

of PEG-siRNA/PEI complex achieved a reduction of microvessel formation and suppression of tumor growth [66]. When the polymer end was decorated with targeting moiety, such as folate or lactose, the delivery of PEG-siRNA into specific cell types was further improved [67, 68].

Hyaluronic acid (HA), a natural polymer having biocompatibility and binding affinity to CD44, has also been widely used as a siRNA carrier. Recently, HA-siRNA conjugate containing cleavable disulfide bonds was developed [69, 70]. The HA conjugation led to the enhancement of serum stability and the formation of a compact nanocomplex with cationic carriers (Figure 4B). Further, HA-siRNA/PEI nanocomplex was efficiently internalized into cells via CD44 receptor-mediated endocytosis and down-regulated the target gene expression in cancer cells. Given the abundance of HA receptors in the liver, HA-siRNA conjugate was delivered specifically into the liver and inhibited the target gene expression after systemic administration [70].

Aptamers are nucleic acids having high affinity and specificity to target molecules; thus, it has been extensively studied as a targeting ligand in biomedical applications. Aptamer-siRNA chimera exhibit high specificity in binding to target protein-expressing cells. For example, prostate-specific membrane antigen (PSMA) targeting A10 aptamer was used to specifically deliver siRNA into PSMA-expressing cells and tumors (Figure 4C) [71, 72]. A10 aptamer-siRNA chimera bound to PSMA on cell surfaces and mediated intracellular uptake. After intracellular translocation, A10 aptamer-siRNA chimera was processed by Dicer and released active siRNA. When A10 aptamer-siRNA chimera targeting polo-like kinase 1 (plk1) was systemically administrated, specific gene suppression and tumor growth inhibition were observed in a PSMA-expressing tumor [72]. The incorporation of PEG into A10 aptamer-siRNA chimera further enhanced the pharmacokinetic and pharmacodynamics properties of the chimera [71]. Similarly, nucleolin-targeting aptamer has been considered as a promising tumor-targeting molecule because of the over expression of nucleolin on various cancer cells [73]. Combination treatment of nucleolin

aptamer-siRNA chimeras against snail family zinc finger 2 (SLUG) and neuropilin 1 (NRP1) synergistically inhibited the invasion of lung cancer cells and tumor-induced angiogenesis.

Microstructured RNAi therapeutics

Efficient and safe delivery of siRNA to target tissues and cells is one of the most critical problems for the therapeutic application of siRNAs. A diversity of siRNA delivery carriers based on polymers, lipids, and nanoparticles have been developed to enhance delivery of siRNA [74]. Cationic polymers can form condensed polyelectrolyte complexes with anionic nucleic acid by electrostatic interactions. Furthermore, because synthetic cationic polymers have the advantage of facile introduction of functional moieties and modification of its structure and molecular weight, they have been widely used as nucleic acid delivery carriers [75].

Nonetheless, siRNA delivery using cationic polymers is much more difficult than plasmid DNA delivery due to the different intrinsic physicochemical properties of the siRNA. The persistence length of dsRNA is approximately ~ 70 nm (corresponding to ~ 260 bp) [76]; therefore, siRNA of ~ 21 bp behaves like a rigid rod. In addition, siRNA, with its 42 negative charges, has a much lower spatial charge density than plasmid DNA which has more than several thousand negative charges per molecule. The rigidity and low charge density of siRNA make it very difficult to form small, stable, and condensed nanocomplexes via electrostatic interaction with cationic polymers.

Cellular uptake and *in vivo* biodistribution of nanoparticles are highly dependent on the shape, size, and surface properties of the nanoparticles. It is well known that stable, compact, and small nanoparticles are more efficiently taken up by cells [77]. Therefore, making stable, compact, and small nanocomplexes of siRNA with cationic polymer carriers is a prerequisite for successful siRNA delivery. Although it is also possible to make more stable and compact complexes if larger

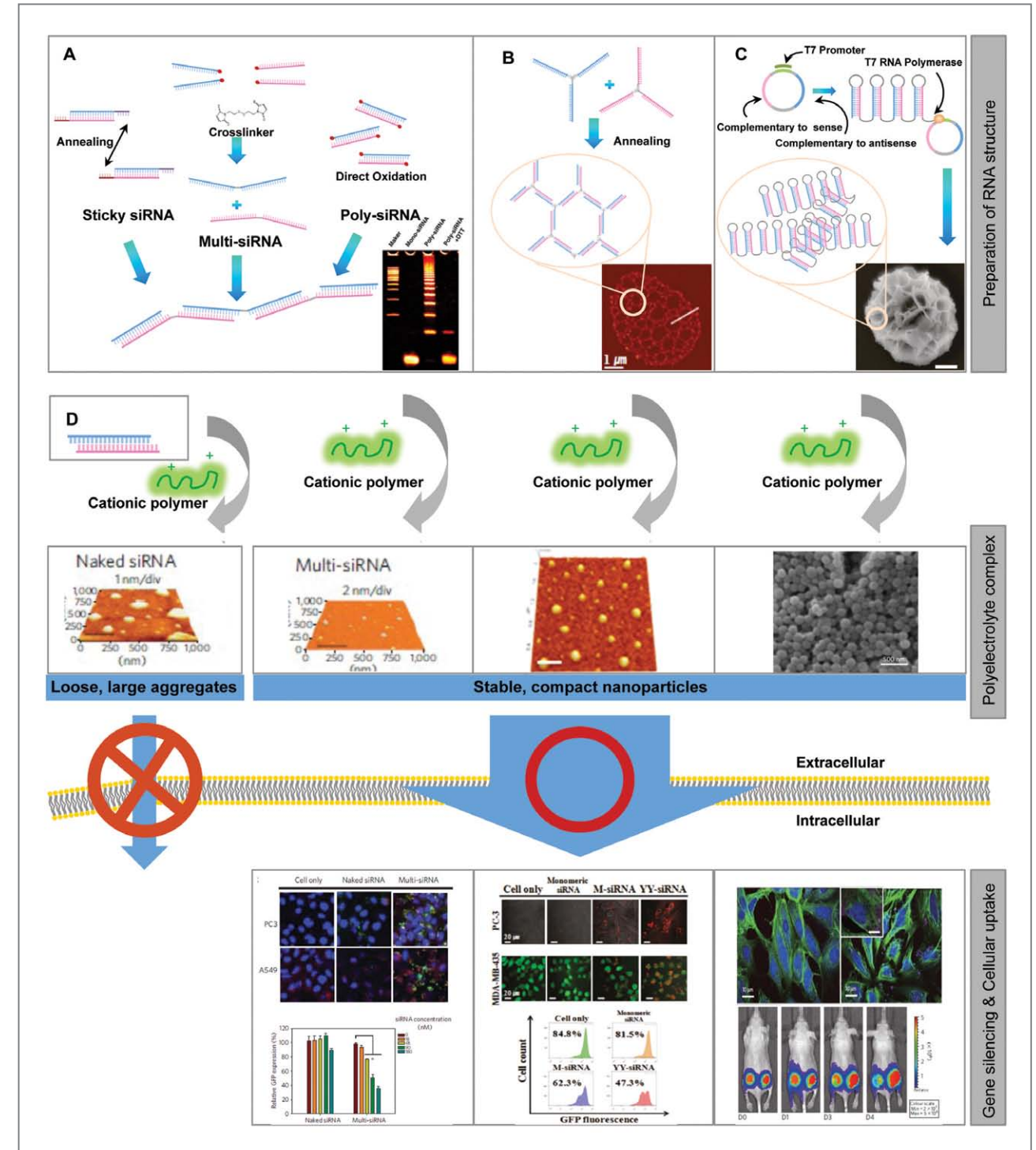


Figure 5 Structured siRNAs for efficient condensation and delivery (Preparation-upper, Polyelectrolyte complex-middle, Gene silencing/ Cellular uptake-bottom). (A) Polymerized siRNAs via complementary annealing, chemical crosslinker, or direct oxidation of thiol groups. (B) siRNA microhydrogel. (C) RNAi microsponge. (D) Conventional siRNA. Reprinted with permission from Ref. [80] Copyright 2010 Nature Publishing Group; Ref. [81] Copyright 2010 Elsevier; Ref. [85] Copyright 2011 American Chemical Society; and Ref. [86] Copyright 2012 Nature Publishing Group.

amounts of high molecular weight cationic polymeric carriers are used, toxicity is also contingent on the concentration and structure of polymers [78]. Recently, structural modification of siRNA itself has been reported, along with chemical modification of carriers, to develop efficient delivery systems without causing toxicities and immune responses.

A gene-like structure was constructed by connecting several siRNAs together to increase the charge density of the siRNAs [79]. Short additional complementary A₅₋₈/T₅₋₈ overhangs were introduced into the 3'-ends of siRNA (called sticky siRNA) and siRNA concatemers were constructed by hybridizing the complementary sticky siRNAs in aqueous solution (Figure 5A). When complexed with PEI, a widely used cationic polymer, the long concatemer sticky siRNA exhibited improved complex stability and protection of siRNAs. The sticky siRNA/PEI complexes resulted in enhanced gene suppression in cultured A549 cells and *in vivo* mouse models. The enhanced stability and delivery efficacy of the complexes were attributed to the increased charge density of long concatemer siRNA structures, which enabled more efficient electrostatic interactions with cationic PEI. This study demonstrated that increasing the size of siRNA like pDNA can improve complex stability and delivery efficacy despite a concern with thermal stability because the sticky siRNA concatemers with A₅/T₈ overhangs have a low melting point ($T_m < 10^\circ\text{C}$).

To solve this problem of thermal instability of the sticky siRNA, two independent groups investigated the chemical crosslinking of several siRNAs together to increase the size of siRNA [80, 81]. Mok et al. synthesized multimerized siRNA (multi-siRNA) using dithio-bis-maleimidoethane (DTME), a cleavable chemical crosslinker (Figure 5A) [80]. Thiol-modified sense or antisense strands at the 3' end were reacted with DTME to form sense and antisense dimeric strands. The prepared dimeric sense and antisense strands were hybridized by complement base pairing to produce multi-siRNAs. In another report, Lee et al. also synthesized polymerized siRNA (poly-siRNA) without using chemical crosslinkers. Poly-siRNA was prepared by

direct oxidation of siRNAs with thiol-modified at the 5'-end of both sense and antisense strands (Figure 5A) [81].

The synthesized multi-siRNAs/poly-siRNAs displayed ladder-like band patterns on polyacrylamide electrophoresis analysis, which implied that mixtures of multi-siRNAs/poly-siRNAs with various degrees of crosslinking were obtained. When treated with reducing reagents of dithiothreitol or glutathione, multi-siRNAs/poly-siRNAs were cleaved into monomeric-siRNAs, which are active components of RNAi. It is well known that intracellular cytosol is more reductive than extracellular environments [82]. Therefore, it was anticipated that monomeric-siRNA would be generated by cleavage of disulfide bonds in the reductive cytosolic environments after cellular uptake of the multi-siRNAs/poly-siRNAs.

According to morphological analyses, multi-siRNA formed more stable and compact nanocomplexes with linear PEI (LPEI), a more biocompatible cationic carrier than branched PEI (bPEI), whereas monomeric-siRNA/LPEI complexes were composed of unstable, large, and loose aggregates. The more stable and compact complex formation was largely attributed to increased charge density and introduction of flexible linkage of multi-siRNA, which enabled more efficient electrostatic interaction and entanglement with cationic polymers. Thus, substantially more multi-siRNA/LPEI complexes entered into cells, and as a consequence, significantly enhanced gene silencing was observed compared to monomeric-siRNA/LPEI complexes, *in vitro* PC3 cells and *in vivo* PC3 xenograft mouse models (Figure 5).

Nonspecific immune responses are a consideration for the clinical application of long siRNAs since they can be elicited by long double-stranded RNAs. The multi-siRNA/LPEI complexes did not induce significant undesired INF- α induction when treated into peripheral blood monocyte cells or ICR mice. Furthermore, sequence-specific mRNA degradation was confirmed through reverse transcription-polymerase chain reaction (RT-PCR) and rapid amplification of cDNA ends (RACE). These results imply that cleavable linkage between siRNAs and regeneration of short monomeric-siRNA

after cellular uptake of multi-siRNA may prevent the induction of immune responses.

Linear forms of gene-like structural modification of siRNA have led to the development of three-dimensional siRNA microstructures. Although many 3D structures made of DNA and RNA have been reported, few of these have exhibited biological activities [83, 84]. Microhydrogels made of networked siRNAs were introduced by Hong et al. (Figure 5B) [85]. These 3D siRNA microhydrogels were synthesized by hybridizing Y-shaped sense strand with Y-shaped antisense strand. A trifunctional chemical crosslinker, tris-(2-maleimidoethyl)amine (TMEA), was reacted with a thiol group at the 3'-end of the sense or antisense strand to synthesize Y-shaped single-stranded RNAs. Dimeric sense or antisense strands were also prepared by reacting 3' thiol-modified sense or antisense strands with a bifunctional chemical crosslinker, 1, 8-bis(maleimidodiethylene) glycol (BM(PEG)₂). By controlling the ratios of Y-shaped and dimeric RNAs, various micrometered siRNA hydrogels with different pore sizes were obtained in aqueous solution through complement base pair annealing.

The siRNA-based microhydrogels were efficiently form stable, ~100 nm of nanocomplexes upon interacting with a cationic polymer LPEI. Furthermore, the nanoscale complexes showed not only superior cellular uptake but also greatly enhanced gene suppression in breast cancer cells (Figure 5). Substantially increased charges as well as flexibility of the siRNA microhydrogels enabled efficient condensation with cationic LPEI polymers. The siRNA microhydrogels were processed by Dicer and the processed product participated in sequence-specific gene inhibition even though no cleavable bond was introduced in the microhydrogels.

In addition to chemical reactions, biological enzymatic reactions were also used to prepare RNA 3D microstructures. Single-stranded circular DNA encoding of both sense and antisense strands of siRNA was used as a template for rolling circle transcription (RCT) to produce long polymers of hairpin RNA repeats (Figure 5C) [86]. Due to the *in vitro* enzymatic RCT process,

a large amount of tandem repeats of hairpin RNA transcripts could be obtained efficiently. Interestingly, the RNA tandem repeats self-assembled into pleated sheets, which subsequently formed sponge-like microspheres (RNAi microsphere). The RNAi microsphere itself formed a highly dense structure without additional cationic materials.

Considering molecular weight and concentration, more than a half million copies of hairpin RNAs were included in a single RNAi microsphere. The tandem repeat of RNA was designed to generate ~21nt siRNA under Dicer processing, and it was confirmed that RNAi microsphere was cleaved after treatment with recombinant Dicer. Owing to the much higher negative charge of RNAi microsphere, cationic PEI polymer interacted readily with RNA particles and formed ~200 nm condensed nanoparticles. The compact nanoparticle complexes exhibited superb cellular uptake and specific gene silencing (Figure 5). It is worth noting that very few RNAi/PEI particles were needed to induce similar gene silencing efficiencies compared to conventional nanoparticle delivery systems. The RNAi microsphere system provides an easy method for large production and high loading of siRNA using biological enzymatic reactions.

DNA/RNA nanoparticle-based RNAi therapeutics

DNA or RNA structural nanotechnology is the design, construction, and application of nucleic acid nanostructures using specific base pairing and programmability of nucleic acids [84, 87]. This bottom-up self-assembly process based on DNA/RNA nanotechnology has been used for various therapeutic applications.

The Guo group constructed RNA-based nanoparticles through packaging RNA (pRNA) engineering and tried to apply the RNA nanoparticles to biomedical applications via functionalization with therapeutic molecules. pRNA is a component of the bacteriophage phi29 DNA packing

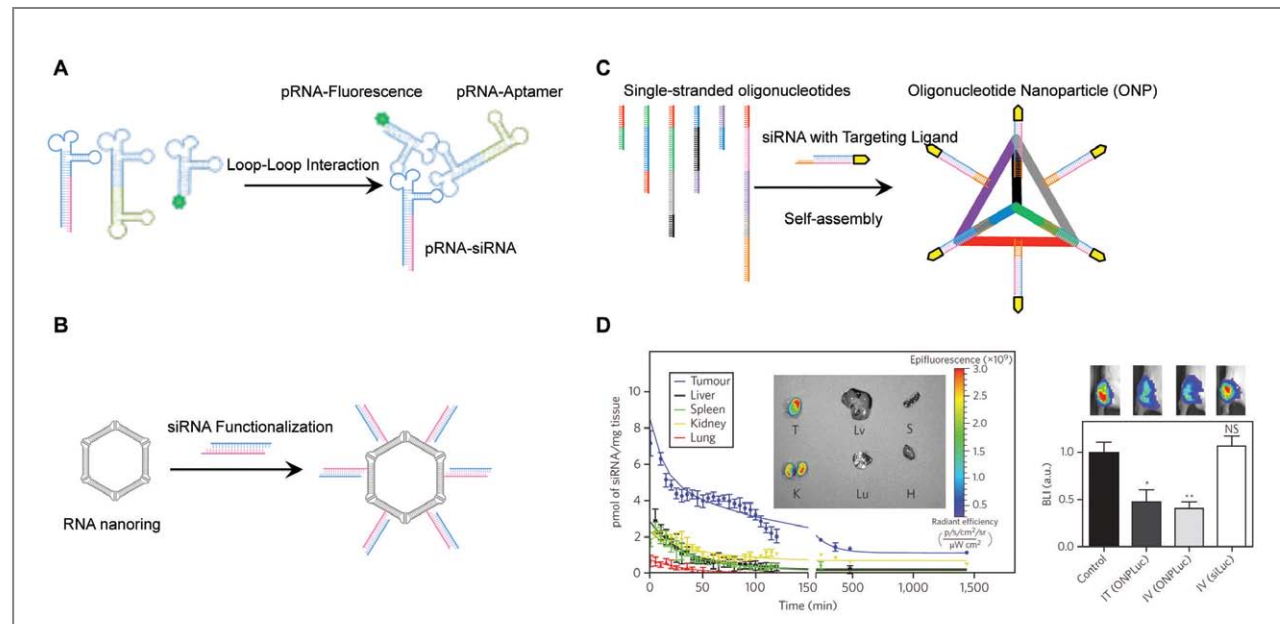


Figure 6 siRNA delivery nanoparticles based on DNA/RNA nanostructures. (A) pRNA trimers harboring siRNA, aptamer, and fluorescent molecules. (B) Hexameric RNA nanoring functionalized with siRNA. (C) Self-assembled tetrahedron oligonucleotide nanoparticle bearing 6 siRNAs with targeting ligand. (D) Pharmacokinetics/biodistribution and luciferase gene silencing efficiency of ONPs in KB tumor-bearing mice. Reprinted with permission from Ref. [93] Copyright 2012 Nature Publishing Group.

motor possessing two distinct domains. One is a dsRNA helical domain with 3'- and 5'-ends and the other is an interlocking domain with two loops (right hand and left hand). The two loops have homology to each other, which enables the pRNA to form dimer, trimer, and oligomeric structures by intermolecular bindings.

Using interlocking loops, trimeric pRNA nanoparticles were prepared (Figure 6A) [88]. Chimeric pRNAs were produced by replacing the helical domain with siRNA, aptamer, or folate. The reengineering of the helical domain did not hinder the formation of trimeric pRNA nanoparticles. Trimeric pRNA nanoparticles harboring pRNA-siRNA, pRNA-CD4 aptamer, and pRNA-fluorescent molecules were treated to CD4 overexpressing cells to examine target-specific co-delivery of all the components at the same time. All three functional molecules were delivered to the specific target at the same time and showed gene silencing activities. Dicer treatment of chimeric pRNA-siRNA also produced in ~21nt siRNA, which implied that gene silencing was

achieved through intracellular Dicer-processed siRNAs. The advantage of trimeric pRNA nanoparticles is their ability to carry multiple siRNAs or other functional moieties at the same time.

RNA nanorings functionalized with siRNAs were constructed with high yield using RNAI and RNAII modules [89, 90]. RNAI and RNAII are transcripts of plasmid that control the replication of ColE1 plasmid of Escherichia coli [91]. The RNAI/II can form a so called inverse kissing-loop complex, mediated by specific loop-loop interaction. The Shapiro group carefully designed 6-loop sequence-modified RNA modules that were able to self-assemble into ~15 nm hexameric nanoring (Figure 6B). The RNA nanoring was further functionalized with 6 siRNAs to use as a siRNA delivery system. Dicer treatment of the nanoring harboring siRNA produced siRNA of ~21nt in length which could enter the RNAi pathway. When the RNA nanoring with siRNAs was transfected into cells, efficient target gene inhibition was achieved. Because six siRNAs can be incorporated into

a single RNA nanoring, multiple genes can be targeted at the same time for synergistic effects or six different regions of one gene can be targeted for more efficient gene silencing. Precise stoichiometric control of siRNA is thus another attractive quality of RNA nanotechnology-based delivery systems.

Conventional drug delivery systems based on polymers or lipids have heterogeneous sizes, shapes, and compositions which make it difficult to predict the pharmacokinetics and pharmacodynamics of drugs *in vivo* [92]. To overcome these limitations, Lee et al. proposed siRNA delivery nanoparticles which are molecularly identical in size and shape by utilizing DNA nanotechnology [93]. Carefully designed six DNA strands were self-assembled into homogeneous tetrahedron oligonucleotide nanoparticle (ONP) using sequence-specific complementary base pairing. Each edge of the ONP had a single stranded overhang which was complementary to the overhang sequence of siRNA, thereby accommodating six siRNAs in a single ONP (Figure 6C). The ONP showed a homogeneous structure of ~26.8 nm in size when measured using dynamic light scatter (DLS). This size of ONP was expected to encourage accumulation near tumor tissues by taking advantage of EPR effects while also avoiding renal clearance. ONPs harboring six siRNAs which were functionalized with folate at the end were treated into folate-overexpressing KB cells *in vitro* without any cationic carriers. They exhibited efficient gene silencing in spite of the absence of cationic carriers. The ONPs were intravenously injected into a KB xenograft mouse to examine the *in vivo* behavior of the particles. The ONPs showed ~4 times longer blood circulation time than parental siRNA and mainly accumulated in the tumor site (Figure 6D). Furthermore, effective target gene silencing in the tumor was achieved without cationic carriers, and no significant increased production of INF- α was observed. The influence of targeting ligand spatial orientation and density on cellular uptake and gene silencing was also investigated by taking advantage of the precise structural control of ONPs. It is important to understand the relationship between cellular uptake and

ligand density and orientation, but it is difficult to figure out experimentally with conventional nanoparticles.

The DNA/RNA nanotechnology-based siRNA delivery particles have several outstanding features as compared to conventional polymeric or liposomal delivery systems. First, the uniform size and shape of these nanostructures can be constructed on demand. Second, the stoichiometry and geometry of ligands or therapeutic molecules can be precisely controlled. Third, multiple siRNAs can be incorporated in one nanoparticle for targeting multiple genes or several regions of one gene, which will improve therapeutic efficacy. Lastly, DNA and RNA are biomaterials and considered less toxic and immunogenic than non bio-based materials. Although some challenges remain, such as endosomal escape, production cost, stability, and a more precise understanding of DNA/RNA folding, DNA/RNA nanostructure-based particles represent a promising new type of delivery system.

Conclusion

siRNA has received considerable attention due to its highly potent and sequence-specific gene silencing ability. Despite its promising therapeutic potential, however, many barriers remain to its clinical application, particularly as regards its inherent properties and issues associated with the delivery of siRNA-based drugs. Research has been underway for some time to develop safe and efficient siRNA delivery systems. In addition, chemical and structural modifications of siRNA itself are being investigated to improve its physicochemical properties in order to enhance stability, reduce off-target effects, and minimize immunogenicity. Other studies are looking at the development of siRNA conjugates with the construction of nucleic acid microstructures or nanostructures to achieve advances in siRNA delivery properties. By integrating a rational design of siRNA with efficient delivery systems, it is anticipated that existing hurdles to the clinical use of siRNA therapeutics can be overcome.

References

- [1] Dykxhoorn D.M., Novina C.D., Sharp P.A., *Nat. Rev. Mol. Cell Biol.*, 4 (2003) 457-467.
- [2] Fire A., Xu S., Montgomery M.K., Kostas S.A., Driver S.E., Mello C.C., *Nature*, 391 (1998) 806-811.
- [3] Hannon G.J., *Nature*, 418 (2002) 244-251.
- [4] de Fougères A., Vornlocher H.P., Maraganore J., Lieberman J., *Nat. Rev. Drug Discov.*, 6 (2007) 443-453.
- [5] Dykxhoorn D.M., Palliser D., Lieberman J., *Gene Ther.*, 13 (2006) 541-552.
- [6] Pecot C.V., Calin G.A., Coleman R.L., Lopez-Berestein G., Sood A.K., *Nat. Rev. Cancer*, 11 (2011) 59-67.
- [7] Lai E.C., *Nat. Genet.*, 30 (2002) 363-364.
- [8] Wei J.-X., Yang J., Sun J.-F., Jia L.-T., Zhang Y., Zhang H.-Z., Li X., Meng Y.-L., Yao L.-B., Yang A.-G., *PLoS One*, 4 (2009) e5382.
- [9] Kleinman M.E., Yamada K., Takeda A., Chandrasekaran V., Nozaki M., Baffi J.Z., Albuquerque R.J.C., Yamasaki S., Itaya M., Pan Y., Appukkuttan B., Gibbs D., Yang Z., Kariko K., Ambati B.K., Wilgus T.A., DiPietro L.A., Sakurai E., Zhang K., Smith J.R., Taylor E.W., Ambati J., *Nature*, 452 (2008) 591-597.
- [10] Hornung V., Ellegast J., Kim S., Brzózka K., Jung A., Kato H., Poeck H., Akira S., Conzelmann K.-K., Schlee M., Endres S., Hartmann G., *Science*, 314 (2006) 994-997.
- [11] Whitehead K.A., Langer R., Anderson D.G., *Nat. Rev. Drug Discov.*, 8 (2009) 129-138.
- [12] Juliano R., Bauman J., Kang H., Ming X., *Mol. Pharm.*, 6 (2009) 686-695.
- [13] Fang J., Nakamura H., Maeda H., *Adv. Drug Del. Rev.*, 63 (2011) 136-151.
- [14] Ku S.H., Kim K., Choi K., Kim S.H., Kwon I.C., *Adv. Healthcare Mater.*, 3 (2014) 1182-1193.
- [15] Vivès E., Schmidt J., Pèlegri A., *Biochim. Biophys. Acta*, 1786 (2008) 126-138.
- [16] Gary D.J., Puri N., Won Y.-Y., *J. Control. Release*, 121 (2007) 64-73.
- [17] Bramsen J.B., Kjems J., *Front. Genet.*, 3 (2012) 154.
- [18] Agrawal S., Temsamani J., Tang J.Y., *Proc. Natl. Acad. Sci. USA*, 88 (1991) 7595-7599.
- [19] Braasch D.A., Paroo Z., Constantinescu A., Ren G., Öz O.K., Mason R.P., Corey D.R., *Bioorg. Med. Chem. Lett.*, 14 (2004) 1139-1143.
- [20] Li Z.-Y., Mao H., Kallick D.A., Gorenstein D.G., *Biochem. Biophys. Res. Commun.*, 329 (2005) 1026-1030.
- [21] Harborth J., Elbashir S.M., Vandeburgh K., Manninga H., Scaringe S.A., Weber K., Tuschl T., *Antisense Nucleic Acid Drug Dev.*, 13 (2003) 83-105.
- [22] Yang X., Sierant M., Janicka M., Peczek L., Martinez C., Hassell T., Li N., Li X., Wang T., Nawrot B., *ACS Chem. Biol.*, 7 (2012) 1214-1220.
- [23] Zhang J., Wu Y.O., Xiao L., Li K., Chen L.L., Sirois P., *Mol Biotechnol.*, 37 (2007) 225-236.
- [24] Hall A.H.S., Wan J., Shaughnessy E.E., Ramsay Shaw B., Alexander K.A., *Nucleic Acids Res.*, 32 (2004) 5991-6000.
- [25] Chiu Y.-L., Rana T.M., *RNA*, 9 (2003) 1034-1048.
- [26] Choung S., Kim Y.J., Kim S., Park H.-O., Choi Y.-C., *Biochem. Biophys. Res. Commun.*, 342 (2006) 919-927.
- [27] Kraynack B.A., Baker B.F., *RNA*, 12 (2006) 163-176.
- [28] Braasch D.A., Jensen S., Liu Y., Kaur K., Arar K., White M.A., Corey D.R., *Biochemistry*, 42 (2003) 7967-7975.
- [29] Layzer J.M., McCaffrey A.P., Tanner A.K., Huang Z., Kay M.A., Sullenger B.A., *RNA*, 10 (2004) 766-771.
- [30] Allerson C.R., Sioufi N., Jarres R., Prakash T.P., Naik N., Berdeja A., Wanders L., Griffey R.H., Swayze E.E., Bhat B., *J. Med. Chem.*, 48 (2005) 901-904.
- [31] Hogrefe R.I., Lebedev A.V., Zon G., Pirolo K.F., Rait A., Zhou Q., Yu W., Chang E.H., *Nucleosides, Nucleotides and Nucleic Acids*, 25 (2006) 889-907.
- [32] Pirolo K.F., Rait A., Zhou Q., Hwang S.H., Dagata J.A., Zon G., Hogrefe R.I., Palchik G., Chang E.H., *Cancer Res.*, 67 (2007) 2938-2943.
- [33] Petersen M., Wengel J., *Trends Biotechnol.*, 21 (2003) 74-81.
- [34] Elmén J., Thonberg H., Ljungberg K., Frieden M., Westergaard M., Xu Y., Wahren B., Liang Z., Ørum H., Koch T., Wahlestedt C., *Nucleic Acids Res.*, 33 (2005) 439-447.
- [35] Turner J.J., Jones S.W., Moschos S.A., Lindsay M.A., Gait M.J., *Mol. Biosys.*, 3 (2007) 43-50.
- [36] Volkov A.A., Kruglova N.Y.S., Meschaninova M.I., Venyaminova A.G., Zenkova M.A., Vlassov V.V., Chernolovskaya E.L., *Oligonucleotides*, 19 (2009) 191-202.
- [37] Morrissey D.V., Blanchard K., Shaw L., Jensen K., Lockridge J.A., Dickinson B., McSwiggen J.A., Vargeese C., Bowman K., Shaffer C.S., Polisky B.A., Zinnen S., *Hepatology*, 41 (2005) 1349-1356.
- [38] Jackson A.L., Burchard J., Leake D., Reynolds A., Schelter J., Guo J., Johnson J.M., Lim L., Karpilow J., Nichols K., Marshall W., Khvorova A., Linsley P.S., *RNA*, 12 (2006) 1197-1205.
- [39] Ui-Tei K., Naito Y., Zenno S., Nishi K., Yamato K., Takahashi F., Juni A., Saigo K., *Nucleic Acids Res.*, 36 (2008) 2136-2151.
- [40] Chen P.Y., Weinmann L., Gaidatzis D., Pei Y., Zavolan M., Tuschl T., Meister G., *RNA*, 14 (2008) 263-274.
- [41] Mook O.R., Baas F., de Wissel M.B., Fluiter K., *Mol. Cancer Ther.*, 6 (2007) 833-843.
- [42] Eberle F., Giebler K., Deck C., Heeg K., Peter M., Richert C., Dalpke A.H., *J. Immunol.*, 180 (2008) 3229-3237.
- [43] Hamm S., Latz E., Hangel D., Müller T., Yu P., Golenbock D., Sparwasser T., Wagner H., Bauer S., *Immunobiology*, 215 (2010) 559-569.
- [44] Hornung V., Guenther-Biller M., Bourquin C., Ablasser A., Schlee M., Uematsu S., Noronha A., Manoharan M., Akira S., de Fougères A., Endres S., Hartmann G., *Nat. Med.*, 11 (2005) 263-270.
- [45] Nallagatla S.R., Bevilacqua P.C., *RNA*, 14 (2008) 1201-1213.
- [46] Elbashir S.M., Harborth J., Lendeckel W., Yalcin A., Weber K., Tuschl T., *Nature*, 411 (2001) 494-498.
- [47] Elbashir S.M., Lendeckel W., Tuschl T., *Genes Dev.*, 15 (2001) 188-200.
- [48] Kim D.H., Behlke M.A., Rose S.D., Chang M.S., Choi S., Rossi J.J., *Nat. Biotechnol.*, 23 (2005) 222-226.
- [49] Siolas D., Lerner C., Burchard J., Ge W., Linsley P.S., Paddison P.J., Hannon G.J., Cleary M.A., *Nat. Biotechnol.*, 23 (2005) 227-231.
- [50] Lee Y.S., Nakahara K., Pham J.W., Kim K., HeZ.Y., Sontheimer E.J., Carthew R.W., *Cell*, 117 (2004) 69-81.
- [51] Sontheimer E.J., *Nat. Rev. Mol. Cell Biol.*, 6 (2005) 127-138.
- [52] Persengiev S.P., Zhu X.C., Green M.R., *RNA Biol.*, 10 (2004) 12-18.
- [53] Jackson A.L., Linsley P.S., *Nature Reviews Drug Discovery*, 9 (2010) 57-67.
- [54] Sun X.G., Rogoff H.A., Li C.J., *Nat Biotechnol.*, 26 (2008) 1379-1382.
- [55] Bramsen J.B., Laursen M.B., Damgaard C.K., Lena S.W., Babu B.R., Wengel J., Kjems J., *Nucleic Acids Res.*, 35 (2007) 5886-5897.
- [56] Hohjoh H., *FEBS Lett.*, 557 (2004) 193-198.
- [57] Khvorova A., Reynolds A., Jayasena S.D., *Cell*, 115 (2003) 209-216.
- [58] Schwarz D.S., Hutvagner G., Du T., Xu Z.S., Aronin N., Zamore P.D., *Cell*, 115 (2003) 199-208.
- [59] Abe N., Abe H., Ito Y., Am J., *Chem. Soc.*, 129 (2007) 15108-15109.
- [60] Raouane M., Desmaële D., Urbinati G., Massaad-Massade L., Couvreur P., *Bioconj. Chem.*, 23 (2012) 1091-1104.
- [61] Soutschek J., Akinc A., Bramlage B., Charisse K., Constien R., Donoghue M., Elbashir S., Geick A., Hadwiger P., Harborth J., John M., Kesavan V., Lavine G., Pandey R.K., Racie T., Rajeev K.G., Rohl I., Toudjarska I., Wang G., Wuschko S., Bumcrot D., Kotliansky V., Limmer S., Manoharan M., Vornlocher H.-P., *Nature*, 432 (2004) 173-178.
- [62] Wolfrum C., Shi S., Jayaprakash K.N., Jayaraman M., Wang G., Pandey R.K., Rajeev K.G., Nakayama T., Charrise K., Ndungo E.M., Zimmermann T., Kotliansky V., Manoharan M., Stoffel M., *Nat. Biotechnol.*, 25 (2007) 1149-1157.
- [63] Nishina K., Unno T., Uno Y., Kubodera T., Kanouchi T., Mizusawa H., Yokota T., *Mol. Ther.*, 16 (2008) 734-740.
- [64] Iversen F., Yang C., Dagnæs-Hansen F., Schaffert D.H., Kjems J., Gao S., *Theranostics*, 3 (2013) 201-209.
- [65] Kim S.H., Jeong J.H., Lee S.H., Kim S.W., Park T.G., *J. Control. Release*, 116 (2006) 123-129.
- [66] Kim S.H., Jeong J.H., Lee S.H., Kim S.W., Park T.G., *J. Control. Release*, 129 (2008) 107-116.
- [67] Oishi M., Nagasaki Y., Itaka K., Nishiyama N., Kataoka K., Am J., *Chem. Soc.*, 127 (2005) 1624-1625.
- [68] Dohmen C., Frohlich T., Lachelt U., Rohl I., Vornlocher H.P., Hadwiger P., Wagner E., *Mol. Ther. Nucleic Acids*, 1 (2012) e7.
- [69] Jang Y.L., Ku S.H., Lee S.J., Park J.H., Kim W.J., Kwon I.C., Kim S.H., Jeong J.H., *J. Nanosci. Nanotechnol.*, 14 (2014) 7388-7394.
- [70] Park K., Yang J.-A., Lee M.-Y., Lee H., Hahn S.K.,

- Bioconj. Chem.*, 24 (2013) 1201-1209.
- [71] Dassie J.P., Liu X.-y., Thomas G.S., Whitaker R.M., Thiel K.W., Stockdale K.R., Meyerholz D.K., McCaffrey A.P., McNamara Ii J.O., Giangrande P.H., *Nat. Biotechnol.*, 27 (2009) 839-846.
- [72] McNamara J.O., Andrechek E.R., Wang Y., Viles K.D., Rempel R.E., Gilboa E., Sullenger B.A., Giangrande P.H., *Nat. Biotechnol.*, 24 (2006) 1005-1015.
- [73] Lai W.-Y., Wang W.-Y., Chang Y.-C., Chang C.-J., Yang P.-C., Peck K., *Biomaterials*, 35 (2014) 2905-2914.
- [74] Whitehead K.A., Langer R., Anderson D.G., *Nat Rev Drug Discov*, 9 (2010) 412-412.
- [75] Akita H., Harashima H., *Expert Opin. Drug Del.*, 5 (2008) 847-859.
- [76] Kebbekus P., Draper D.E., Hagerman P., *Biochemistry-U.S.*, 34 (1995) 4354-4357.
- [77] Mok H., Park T.G., *Biopolymers*, 89 (2008) 881-888.
- [78] Lv H.T., Zhang S.B., Wang B., Cui S.H., Yan J., *J Control Release*, 114 (2006) 100-109.
- [79] Bolcato-Bellemin A.L., Bonnet M.E., Creusatt G., Erbacher P., Behr J.P., *P Natl Acad Sci USA*, 104 (2007) 16050-16055.
- [80] Mok H., Lee S.H., Park J.W., Park T.G., *Nat Mater*, 9 (2010) 272-278.
- [81] Lee S.Y., Huh M.S., Lee S., Lee S.J., Chung H., Park J.H., Oh Y.K., Choi K., Kim K., Kwon I.C., *J. Control. Release*, 141 (2010) 339-346.
- [82] Meng F.H., Hennink W.E., Zhong Z., *Biomaterials*, 30 (2009) 2180-2198.
- [83] Rothmund P.W.K., *Nature*, 440 (2006) 297-302.
- [84] Pinheiro A.V., Han D.R., Shih W.M., Yan H., *Nat. Nanotechnol.*, 6 (2011) 763-772.
- [85] Hong C.A., Lee S.H., Kim J.S., Park J.W., Bae K.H., Mok H., Park T.G., Lee H., *J. Am. Chem. Soc.*, 133 (2011) 13914-13917.
- [86] Daubendiek S.L., Ryan K., Kool E.T., *J. Am. Chem. Soc.*, 117 (1995) 7818-7819.
- [87] Guo P.X., *Nat. Nanotechnol.*, 5 (2010) 833-842.
- [88] Khaled A., Guo S.C., Li F., Guo P.X., *Nano Lett.*, 5 (2005) 1797-1808.
- [89] Grabow W.W., Zakrevsky P., Afonin K.A., Chworos A., Shapiro B.A., Jaeger L., *Nano Lett*, 11 (2011) 878-887.

- [90] Afonin K.A., Kireeva M., Grabow W.W., Kashlev M., Jaeger L., Shapiro B.A., *Nano Lett.*, 12 (2012) 5192-5195.
- [91] Eguchi Y., Tomizawa J., *Cell*, 60 (1990) 199-209.
- [92] Petros R.A., DeSimone J.M., *Nat. Rev. Drug Discov.*, 9 (2010) 615-627.
- [93] Lee H., Lytton-Jean A.K.R., Chen Y., Love K.T., Park A.I., Karagiannis E.D., Sehgal A., Querbes W., Zurenko C.S., Jayaraman M., Peng C.G., Charisse K., Borodovsky A., Manoharan M., Donahoe J.S., Truelove J., Nahrendorf M., Langer R., Anderson D.G., *Nat. Nanotechnol.*, 7 (2012) 389-393.

Note

This article and images are drawn from “Chemical and structural modifications of RNAi therapeutics” in *Advanced Drug Delivery Reviews*, 104 (2016), pp 16~28.



Feature Articles

Approximating Bone ECM: Crosslinking Directs Individual and Coupled Osteoblast/Osteoclast Behavior



Min Tai HWANG

Center for Biomaterials
Biomedical Research
Institute
mph@kist.re.kr



Kwi Deok PARK

Center for Biomaterials
Biomedical Research
Institute
kpark@kist.re.kr

Introduction

The extracellular matrix (ECM) is a collection of numerous components which collectively provide a wide range of functionality. Apart from providing structural support, the ECM is also a conduit for cell-cell communication [1] and a repository for growth factors [2-4]. Perhaps most importantly, the ECM imparts a distinct environment optimized for the residence of cells in a context-dependent manner. In this regard, bone ECM provides a niche for osteoblasts (OB) and osteoclasts (OC), two primary cell types that function to maintain homeostasis of the bone. Specifically, OBs form bone matrix via calcium phosphate deposition onto a collagenous matrix in which the crosslinking of collagen fibrils via extracellular lysyl oxidase (LOX) precedes and regulates the manner of mineral deposition [5, 6]. Such LOX-mediated intra/intermolecular covalent crosslinking of collagen and elastin increases the density of bone ECM, thereby leading to a relatively compact ECM [7]. On the other hand, OC-mediated bone resorption, which precedes OB activity, progresses via the secretion of hydrogen ions and various cathepsins/matrix metalloproteinases (MMPs) [8] into the bone ECM, ultimately resulting in a relatively loose ECM with fewer collagen crosslinks [9]. Put simply, the bone ECM profile is an aggregate product of OB and OC activity.

Given that cells exist within ECM, studies examining the effect of microenvironmental cues on cell behavior are garnering attention [10, 11], particularly as regards ECM stiffness [12], ligand availability [13], and

topography [14]. However, granted that a reductionist approach to the examination of an individual cue offers crucial information in and of itself, it should be noted that a single cue alone is not sufficient to determine cell fate. Indeed, MSCs have been shown to exhibit increased differentiation on stiff substrates when coated with collagen type I as compared to collagen type IV, laminin, or fibronectin [15]. From this perspective, current methods that coat a substrate with a single ECM protein fall short of detailing the full range of biological, chemical, and physical properties of natural ECM. Equally important, polyacrylamide, used in many stiffness-mediated studies, presents a non-physiological elastic force as opposed to the viscoelastic behavior of natural ECM [16]. In essence, the ability to examine the effect of bone ECM phenotype on its resident cells within the context of a physiologically relevant microenvironment is highly attractive.

Herein, we generate preosteoblast-derived ECM (PDM), which consists of a natural self-assembled ECM network [17], and emulate physiological LOX-mediated ECM crosslinking via genipin. As a natural crosslinking agent that forms intra/intermolecular collagen crosslinks [18], genipin is conventionally used in regenerative applications as a biocompatible alternative to glutaraldehyde-based acellular tissue fixation [19]. In essence, a novel platform with variable crosslinking densities of PDM is used to represent different bone ECM profiles, upon which individual OB/OC behavior is observed. Furthermore, given the intricately coupled activity of OBs and OCs [20, 21], we examine how ECM crosslinking affects OB-/OC-derived osteocoupling markers. Put together, we approximate the varying phenotypes of bone ECM and report on the preferential maturation of OBs and OCs on compact and loose PDM, respectively. Finally, we identify ECM crosslinking density as a new mode by which osteocoupling occurs.

Results

Crosslinked PDM exhibits different ECM profiles

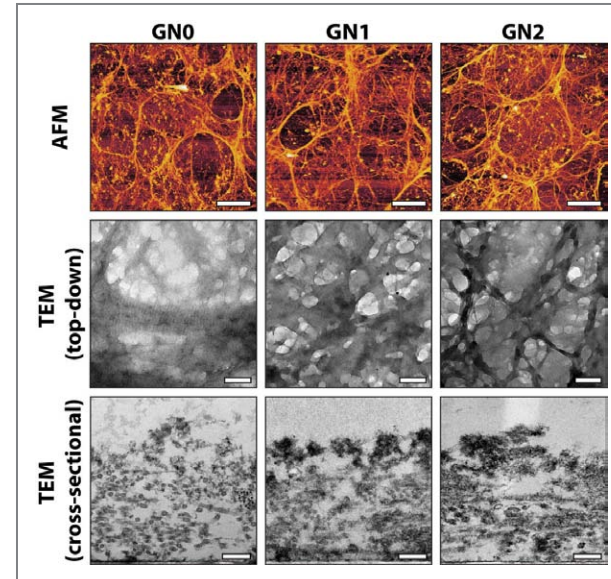


Figure 1 Genipin-treated PDM exhibit different ECM profiles. PDM (GN0, GN1, GN2) exhibit increasing density with an increase in genipin concentration as assessed via AFM (top row, scale bar: 20 μm) and TEM (top view: middle row, scale bar: 200 nm; cross-sectional view: bottom row, scale bar: 100 nm).

The ECM plays a number of fundamental roles in the bone milieu, including those in development [22] and stem cell maintenance [23]. Not surprisingly, decellularized natural ECM has emerged as a promising material in a variety of regenerative applications [24]. Importantly, given that cell phenotype determines the composition of secreted ECM [17] and the type of differentiation that is optimal on the ECM [25], we generate preosteoblast (pOB)-derived ECM (PDM) to mimic the structure and functionality of the environment in which OBs/OCs reside. Specifically, MC3T3 cells are cultured on plastic coverslips in growth media for 8 days, after which samples are decellularized to leave behind the pOB-derived ECM. The PDM is subsequently treated with deoxyribonuclease/ribonuclease to ensure complete decellularization. Finally, PDM is crosslinked to varying degrees via the addition of genipin (GN0 – 0% w/v; GN1 – 1% w/v; GN2 – 2% w/v) as a means to mimic the natural ECM crosslinking activity of LOX [6, 26]. Increased ECM crosslinking is apparent at

both the micro and nano level, as assessed via atomic force microscopy (AFM) (Figure 1, top row) and cryo transmission electron microscopy (cryo-TEM) (Figure 1, middle row), respectively. Untreated GN0 PDM has the lowest ECM density presumably due to the removal of uncrosslinked collagen chains weakly associated to the ECM – multiple washes are used during PDM preparation. Cross-sectional cryo-TEM images of PDM further corroborate the increased ECM density, though overall thickness remains relatively constant at approximately 800 nm (Figure 1, bottom row). Finally, AFM measurements indicate a significant increase in the stiffness of PDM with increasing genipin concentration; uncrosslinked PDM has a stiffness of 0.24 ± 0.11 kPa, while the intermediate and most compact PDM measure 2.24 ± 1.10 kPa and 3.21 ± 1.90 kPa, respectively. Similarly, the roughness of PDM increases with genipin concentration. It should be noted that our PDM platform lacks calcium phosphate mineralization of ECM, which normally follows LOX-mediated bone ECM crosslinking [7]. Our platform is therefore representative of early-stage bone ECM located in proximity to the bone surface rather than the interior of bone.

Cells respond to biocompatible PDM via mechanotransduction

Immunofluorescence against fibronectin and collagen indicates that distinguishing ECM epitopes are preserved throughout the crosslinking process (Figure 2A). It should be noted that our group also observed laminin, vitronectin [17], and other minor components such as perlecan, fibulin-2, and emilin-1 for uncrosslinked PDM. We then examine how cells respond morphologically to varying ECM crosslinking density. Immunofluorescence images demonstrate that MC3T3 cells cultured on loose PDM (e.g., GN0) have diffuse actin while those cultured on progressively more compact PDM (e.g., GN1 and GN2) show signs of stress fiber formation (Figure 2B, top row). Image analysis indicates that MC3T3 cells cultured on GN0 have a small aspect ratio while those cultured on GN2 exhibit a simultaneous increase

in aspect ratio and decrease in cell size (Figure 2C). To examine if cells are responding to variable ECM crosslinking via mechanotransductive pathways, we then add 50 μM blebbistatin to inhibit the activity of

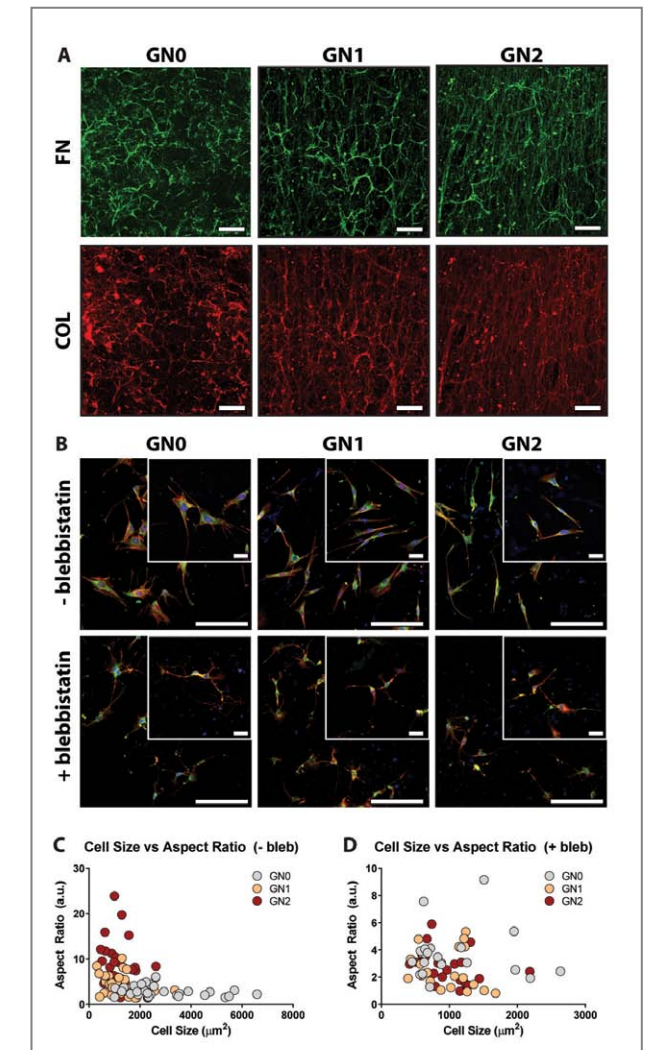


Figure 2 Cells respond to various biocompatible PDMs via mechanotransduction. (A) Immunofluorescence of various PDMs shows bioactive ECM epitopes (green: fibronectin, red: collagen). Scale bars: 100 μm . (B) Immunofluorescence images of MC3T3 cells 24 hrs post-seeding show that round cells on uncrosslinked ECM (GN0) become increasingly elongated on crosslinked ECM (GN1 and GN2). The addition of 50 μM blebbistatin attenuates such ECM crosslinking-dependent changes (red: f-actin, green: vinculin, blue: nuclei). Scale bars: 200 μm ; 50 μm (inset). (C) Cells cultured on GN0 have varying sizes with a small aspect ratio but progressively transition toward smaller-sized cells with a large aspect ratio on GN1 and GN2. (D) Blebbistatin inhibits the activity of non-muscle myosin II, resulting in an attenuation of ECM crosslinking-dependent changes.

non-muscle myosin II, a central component through which cells sense the stiffness of their environment. The addition of blebbistatin results in an attenuation of substrate-dependent morphological changes (Figure 2B, bottom row and 2D). Put together, our data suggests that cells respond to various PDM cues, of which stiffness-mediated mechanotransduction is one particular pathway.

Osteoblast maturation progressively increases on compact PDM

Preosteoblastic MC3T3 cells are differentiated on various PDMs to examine the effect of ECM crosslinking on OB maturation. Cell proliferation for all groups

remains non-significant to one another at both 12 and 60 hrs post-seeding (Figure 3A), indicating that differences in cell proliferation are not responsible for differences among groups observed in subsequent differentiation studies. Transcript levels of RUNX2, the master control gene for osteoblastogenesis, are assessed after three days of differentiation and are statistically the highest on GN2 (Figure 3B). Transcript levels for alkaline phosphatase (ALP) and osteocalcin (OCN), other OB maturation markers, show a similar trend, in which increased transcript levels are observed with increasing ECM crosslinking. ALP protein levels, an early marker for OB maturation, are assessed after one week of differentiation and are significantly lower for GN0 than for GN1 or

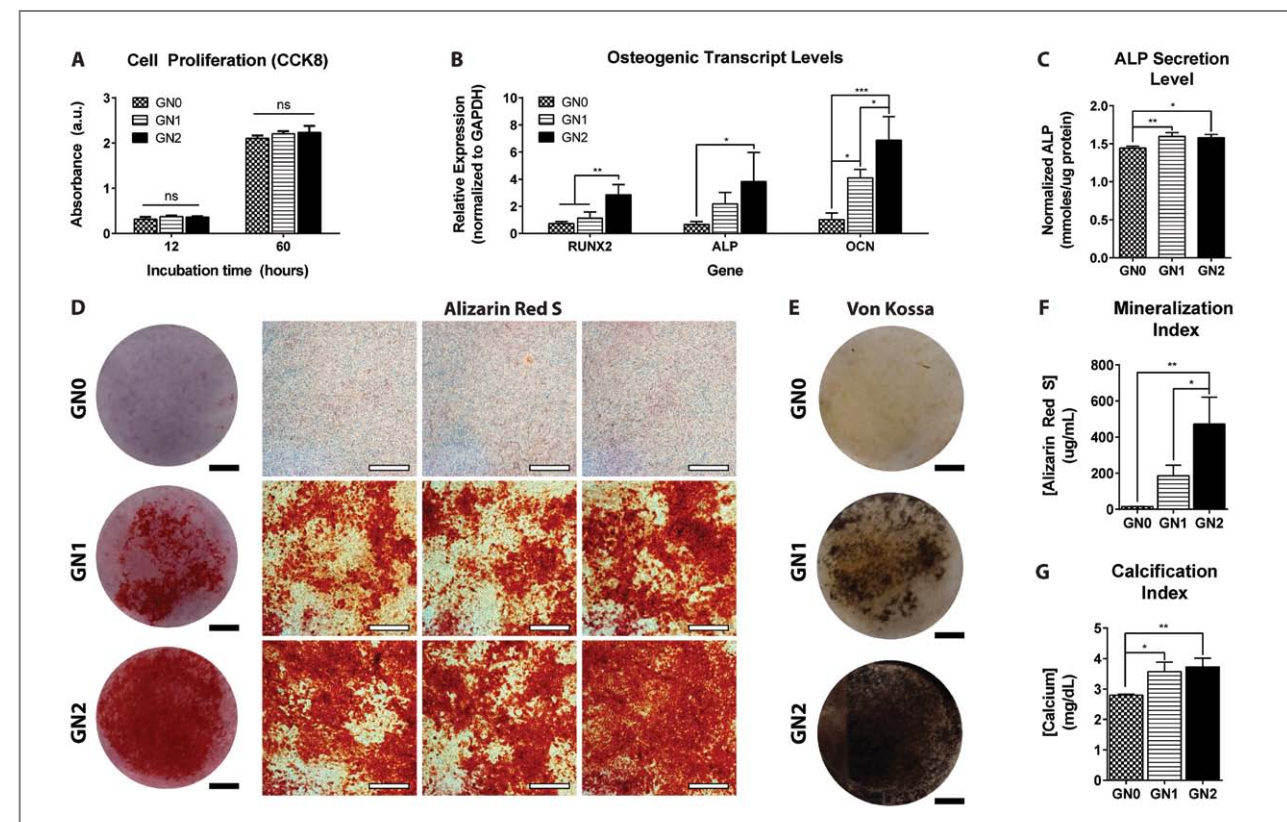


Figure 3 Osteoblast maturation progressively increases on compact PDM. (A) MC3T3 proliferation is assessed via CCK-8 at 12 and 60 hrs post-seeding. (B) OB-specific transcript levels (RUNX2: runt-related transcription factor 2; ALP: alkaline phosphatase; OCN: osteocalcin) are examined after 3 days of maturation. (C) ALP protein expression is assessed after 1 week of OB maturation. (D) Samples are examined for calcium mineralization via Alizarin Red S staining (left column: low-magnification images). Scale bars: 5 mm (low magnification); 500 μ m (close-up). (E) Samples are examined for phosphate mineralization via von Kossa staining. Scale bar: 5 mm. (F) Alizarin Red S samples are dissolved and measured for absorbance at 405 nm. (G) Calcium deposition is directly quantified via a colorimetric assay. Mean \pm SD for all graphs and n=3 for all experiments.

GN2 (Figure 3C). Similarly, OB-mediated mineralization increases with ECM crosslinking. Low magnification Alizarin Red S stains clearly show an increase in calcium deposition (red) on more compact PDM, further corroborated by representative close-up images of each sample (Figure 3D). An increase in phosphate deposition is also observed, as assessed via von Kossa stains (Figure 3E). Finally, calcium deposition is quantified both indirectly and directly. Absorbance readings of dissolved Alizarin Red S samples provide a semi-quantitative measure of mineralization and indicate significantly increased OB mineralization on GN2 as compared to GN0 or GN1 (Figure 3F). Direct measurements of calcium deposition, taken via a colorimetric assay, indicate a higher level of osteoblastogenesis for pOBs cultured on more compact PDM (Figure 3G). These results are interesting in the context of MSCs, which show a bias towards osteogenesis when cultured on stiff (i.e., 25-40 kPa) collagen-coated polyacrylamide gels [27-29]. While our findings corroborate an increased level of osteogenesis on progressively stiffer PDM, our results indicate that OB maturation occurs on ECM with much lower values of stiffness (i.e., 3.21 kPa). These results highlight the importance of a comprehensive ECM microenvironment, further underscored when considering that collagen-coated polyacrylamide substrates confer a non-physiological elastic environment as opposed to the viscoelastic behavior of natural ECM [16]. These results may also represent specific areas within the bone; remodeling of cancellous bone occurs at the boundary between bone and marrow in which the unmineralized matrix of trabecular bone would be softer than the surrounding cortical bone [30].

Osteoclast maturation progressively increases on loose PDM

The effect of ECM crosslinking on OCs, the counter cell type to OBs that together regulate bone remodeling, is examined by differentiating macrophage preosteoclastic RAW264.7 cells on various PDMs. Given that OCs are derived from hematopoietic stem cells, which give rise to immune cells such as macrophages

and neutrophils, early levels of matrix metalloproteinase 9 (MMP-9) secretion are assessed as an indicator of inflammation, and therefore, PDM immunogenicity. ELISA readings after two days of culture indicate that a non-significant amount of MMP-9 is secreted from RAW264.7 cells cultured on PDM compared to those in the control group (120 ± 7.96 pg/mL) which consists of cells cultured on tissue culture-treated plastic alone (Figure 4A). Transcript levels for nuclear factor of activated T-cells (NFATC1), a principal transcriptional mediator for osteoclastogenesis, are assessed after four days of differentiation and are statistically higher on GN0 than on GN1 or GN2 (Figure 4B). Similarly, transcript levels for OC maturation markers: tartrate-resistant acid phosphatase (ACP5), matrix metalloproteinase 9 (MMP9), and cathepsin K (CTSK), are statistically the highest on GN0 PDM (Figure 4C). Mature OCs, assessed after 7 days of differentiation, are morphologically identified by an actin ring around the periphery of a multinucleated cell formed by the fusion of mononuclear precursor OCs; a larger number of nuclei is an indicator of progressed differentiation and maturity [31]. Immunofluorescence imaging (red: f-actin, blue: nuclei) demonstrates that OC maturation occurs more readily on relatively loose GN0 than on more compact GN1 or GN2 (Figure 4D). Interestingly, apart from variances observed in OC number, we also report that ECM crosslinking affects OC size, in which larger OCs are observed on less compact PDM (Figure 4E). GN0 yields larger OCs with up to 40 nuclei per cell while the vast majority of OCs on GN2 have 3-5 nuclei, suggesting that increased ECM crosslinking limits pOC maturation to a partially differentiated early-fusion phenotype. While the mechanism by which pOCs sense ECM density to modulate their differentiation is not yet clear, proteins involved in the fusion of pOCs, such as dendritic cell-specific transmembrane protein (DC-STAMP) [32], could play a role. Finally, staining against tartrate-resistant acid phosphatase (TRAP), an essential protein involved in OC function [33], illustrates that OC maturation is highest on loose PDM, progressively diminishing with increasing ECM crosslinking (Figure 4F). Quantification of TRAP+ multinucleated (≥ 3 nuclei) OCs indeed indicates that OC

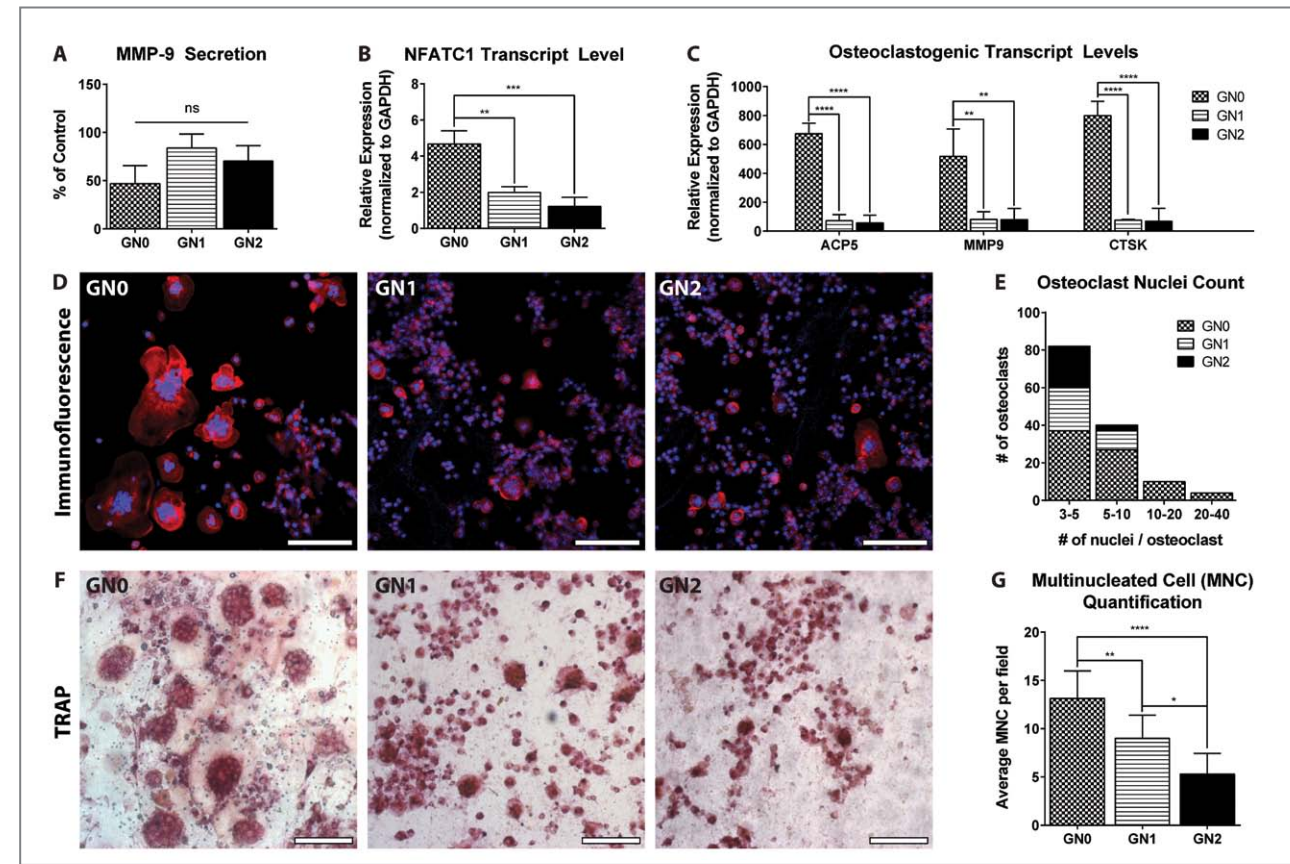


Figure 4 Osteoclast maturation progressively increases on loose PDM substrates. (A) MMP-9 levels of RAW264.7 cells are assessed via ELISA; control cells cultured on tissue culture plastic secrete 120 ± 7.96 pg/mL MMP-9. (B), (C) OC-specific transcript levels (NFATc1: nuclear factor of activated T-cells, ACP5: tartrate-resistant acid phosphatase; MMP9: matrix metalloproteinase 9; CTSK: cathepsin K) are examined after 4 days of maturation. (D) Immunofluorescence images of OCs are taken after 7 days of differentiation (red: f-actin, blue: nuclei). Scale bar: 50 μ m. (E) Immunofluorescence images are analyzed to demonstrate the effect of crosslinking density on the number and size of OCs. (F) Tartrate-resistant acid phosphatase (TRAP; purple) is visualized as a marker of OC maturation. Scale bar: 100 μ m. (G) TRAP-positive cells with at least three nuclei are counted. Mean \pm SD for all graphs and n=3 for all experiments.

maturation and function is highest on GN0, while that on GN1 is statistically higher than that of GN2 (Figure 4G). Taken together, it is possible that physiological conditions accompanied by loose bone ECM further facilitate both OC formation and activity alike. For instance, ECM is destabilized prior to bone formation via the production of collagenase by bone lining cells [34], and such weakening of ECM could prime the environment for OC formation.

ECM crosslinking mediates osteocoupling events

The relationship between OBs and OCs (i.e., osteocoupling) is both intricate and potent in its capacity to remodel bone. For instance, the interplay among the receptor activators of nuclear factor-kappa B (RANK), RANK ligand (RANK-L), and osteoprotegerin (OPG) is a well-recognized dynamic that couples the activity of OBs and OCs [35] – the RANK/RANK-L/OPG axis (Figure 5A). Specifically, RANK-L produced by OBs, presented as either a surface-bound ligand or a soluble protein, binds to RANK receptors on precursor OCs and leads to osteoclastogenesis. OPG, on the other hand, is another OB-derived soluble factor that acts as a decoy receptor

for RANK-L. Consequently, an increase in OPG levels inhibits OC maturation and contributes to an environment that favors the anabolic activity of OBs. More recently, other OB- and OC-specific proteins have been shown to affect the maturation of both OBs and OCs alike [36, 37]. In particular, EphB4 on OBs and ephrinB2 on OCs bind to one another to provide a bidirectional signal in which OB and OC maturation is enhanced and inhibited, respectively (Figure 5B). Interestingly, research thus far indicates that mechanical forces affect the expression of members of the Eph/ephrin family [38, 39]. For example, ephrinA2 – expressed on OCs as a ligand for EphA2 on

Obs [40] – has been shown to increase in compressed periodontal ligament fibroblasts [38]. Considering the evolutionary conservation of protein functions, it is then likely that such mechano-dependent change in fibroblast ephrinA2 expression extends to other cells such as OCs.

After a week of MC3T3 osteogenic differentiation, we observe an overall decrease in RANK-L transcript levels for cells cultured on progressively more compact PDM, in which transcript levels are significantly higher on GN0 than on GN1 or GN2 (Figure 5C). Put differently, OBs cultured on relatively loose PDM are more likely to play a role in the upregulation of OC maturation, while those

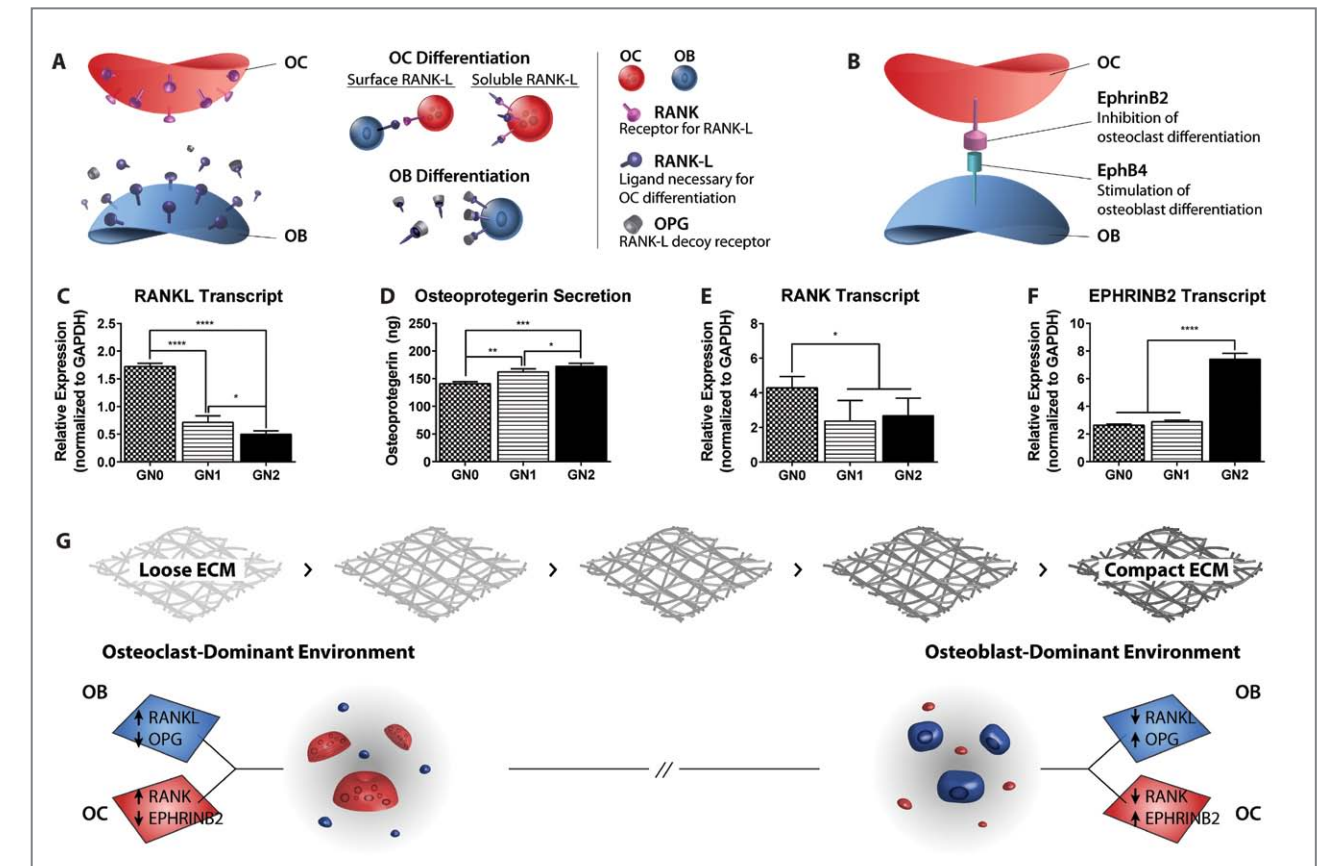


Figure 5 ECM crosslinking couples the interaction between OBs and OCs. (A) OB-derived RANK-L binds to RANK receptors on OCs to initiate osteoclastogenesis; OPG, also produced by OBs, acts as a decoy receptor by binding to RANK-L. (B) EphB4/ephrinB2 bidirectional signaling between OBs and OCs. (C) RANK-L transcript levels from MC3T3 cells are assessed after 7 days of osteogenic differentiation. (D) OPG protein secretion from differentiating MC3T3 cells is assessed via ELISA. (E) RANK transcript levels from RAW264.7 cells differentiating on the least compact ECM (GN0). (F) Transcript levels for ephrinB2 are highest among RAW264.7 cells assessed after 4 days of osteoclastic differentiation. (G) ECM crosslinking-mediated levels of OB- and OC-specific markers work in tandem to generate an OC-dominant environment on loose PDM and an OB-dominant environment on compact PDM. Mean \pm SD for all graphs and n=3 for all experiments.

cultured on compact PDM are less likely. OPG protein levels, on the other hand, are lowest for cells cultured on GN0, and increase for those cultured on progressively more compact PDM (Figure 5D). Given that OPG competitively binds to RANK-L, a potent OC maturation factor, OBs cultured on loose PDM are then more likely to provide an environment conducive for OC maturation, while those cultured on compact PDM are more likely to provide one favorable towards OB maturation. Similarly, the effect of ECM crosslinking on OC-derived osteocoupling markers is examined after four days of RAW264.7 osteoclastic differentiation. Transcript levels for RANK are significantly higher for cells cultured on GN0 than those on GN1 or GN2 (Figure 5E). In other words, OCs cultured on relatively loose PDM are more receptive to RANK-L-mediated osteoclastogenesis. Levels of EPHRINB2, on the other hand, are significantly higher on the most compact GN2 (Figure 5F), indicating that OCs cultured on compact PDM are more likely to play a role in the upregulation of OB maturation. In essence, OBs modulate their signals (e.g., RANK-L and OPG) to facilitate OC maturation on loose ECM and OB maturation on compact ECM. On the other hand, OCs modulate their signals (e.g., RANK and EPHRINB2) to facilitate OB maturation on compact ECM and OC maturation on loose ECM. Put together, bone ECM crosslinking is a key factor behind osteocoupling, in which OB- and OC-derived markers work in tandem to generate an OC-dominant environment on loose PDM and an OB-dominant environment on compact PDM (Figure 5G). On a final note, it is important to recognize that there must be another cue that affects osteocoupling; a constantly hard and compact ECM would only give rise to OBs as a continually soft and loose ECM would OCs. We speculate that a fluctuating physiological demand for calcium or phosphate ions could affect MMP or LOX activity to modulate bone ECM density. Another possibility is the presence of an undetermined link between OBs and OCs, which could be a point of further investigation via co-culture studies.

Conclusions

Current studies that explore ECM microenvironmental effects on cell behavior focus on elucidating the role of an individual cue, but fall short of capturing the full biophysical scope of natural ECM. In this study, we demonstrate the use of cell-derived ECM, which consists of a natural self-assembled ECM network, as an alternative to traditional synthetic substrates. In particular, we approximate various bone ECM profiles by using different concentrations of genipin, a natural crosslinker. Using this platform, we demonstrate increased osteoblast and osteoclast maturation on compact and loose ECM, respectively. Most notably, we identify ECM crosslinking density as an underlying force in the coupling between osteoblast and osteoclast behavior.

Note

This article and images are drawn from “Approximating Bone ECM: Crosslinking directs individual and coupled osteoblast/osteoclast behavior” in *Biomaterials*, Vol. 103, pp. 22–32.

References

- [1] Fan D, Creemers EE, Kassiri Z. *Circulation Research* 2014; 114: 889-902.
- [2] ten Dijke P, Arthur HM. *Nat. Rev. Mol. Cell Biol.* 2007; 8: 857-69.
- [3] Wang X, Harris RE, Bayston LJ, Ashe HL. *Nature* 2008; 455: 72-7.
- [4] Zhu J, Clark RAF. *J. Invest. Dermatol.* 2014; 134: 895-901.
- [5] Wassen MHM, Lammens J, Tekoppele JM, Sackers RJB, Liu Z, Verboort AJ, et al. *Journal of Bone and Mineral Research* 2000; 15: 1776-85.
- [6] Bailey AJ, Wotton SF, Sims TJ, Thompson PW. *Connective Tissue Research* 1993; 29: 119-32.
- [7] Knott L, Bailey AJ. *Bone* 1998; 22: 181-7.

- [8] Vaananen HK, Zhao H, Mulari M, Halleen JM. *Journal of Cell Science* 2000; 113: 377-81.
- [9] Oxlund H, Barckman M, Ortoft G, Andreassen TT. *Bone* 1995; 17: 365s-71s.
- [10] Humphrey JD, Dufresne ER, Schwartz MA. *Nat. Rev. Mol. Cell Biol.* 2014; 15: 802-12.
- [11] Charras G, Sahai E. *Nat. Rev. Mol. Cell Biol.* 2014; 15: 813-24.
- [12] Engler AJ, Sen S, Sweeney HL, Discher DE. *Cell* 2006; 126: 677-89.
- [13] Trappmann B, Gautrot JE, Connelly JT, Strange DGT, Li Y, Oyen ML, et al. *Nature Materials* 2012; 11: 642-9.
- [14] Teo BKK, Wong ST, Lim CK, Kung TYS, Yap CH, Ramagopal Y, et al. *ACS Nano* 2013; 7: 4785-98.
- [15] Rowlands AS, George PA, Cooper-White JJ. *American Journal of Physiology-Cell Physiology* 2008; 295: C1037-C44.
- [16] Chaudhuri O, Gu L, Darnell M, Klumpers D, Bencherif SA, Weaver JC, et al. *Nat. Commun.* 2015; 6:6364.
- [17] Bae SE, Bhang SH, Kim B-S, Park K. *Biomacromolecules* 2012; 13: 2811-20.
- [18] Jae SY, Yong JK, Soo HK, Seung HC. *Korean J. Thorac. Cardiovasc. Surg.* 2011; 44: 197-207.
- [19] Chang Y, Tsai CC, Liang HC, Sung HW. *Biomaterials* 2002; 23: 2447-57.
- [20] Cao X. *Nature Medicine* 2011; 17: 1344-6.
- [21] Henriksen K, Neutzsky-Wulff AV, Bonewald LF, Karsdal MA. *Bone* 2009; 44: 1026-33.
- [22] Norton WHJ, Ledin J, Grandel H, Neumann CJ. *Development* 2005; 132: 4963-73.
- [23] Kollet O, Dar A, Shvitiel S, Kalinkovich A, Lapid K, Sztainberg Y, et al. *Nature Medicine* 2006; 12: 657+.
- [24] Prewitz MC, Seib FP, von Bonin M, Friedrichs J, Stissel A, Niehage C, et al. *Nature Methods* 2013; 10: 788+.
- [25] Choi D, Suhaeri M, Hwang M, Kim I, Han D, Park K. *Cell Tissue Res.* 2014; 357: 781-92.
- [26] Grau-Bové X, Ruiz-Trillo I, Rodriguez-Pascual F. *Scientific Reports* 2015; 5: 10568.
- [27] Kilian KA, Bugarija B, Lahn BT, Mrksich M. *Proceedings of the National Academy of Sciences* 2010; 107: 4872-7.
- [28] Shih YRV, Tseng KF, Lai HY, Lin CH, Lee OK. *Journal of Bone and Mineral Research* 2011; 26: 730-8.
- [29] Dupont S, Morsut L, Aragona M, Enzo E, Giullitti S,

- Cordenonsi M, et al. *Nature* 2011; 474: 179-83.
- [30] Hauge EM, Qvesel D, Eriksen EF, Mosekilde L, Melsen F. *Journal of Bone and Mineral Research* 2001; 16: 1575-82.
- [31] Lees RL, Sabharwal VK, Heersche JNM. *Bone* 2001; 28:187-94.
- [32] Yagi M, Miyamoto T, Sawatani Y, Iwamoto K, Hosogane N, Fujita N, et al. *The Journal of Experimental Medicine* 2005; 202: 345-51.
- [33] Hollberg K, Hultenby K, Hayman AR, Cox TM, Andersson G. *Experimental Cell Research* 2002; 279: 227-38.
- [34] Chambers TJ, Fuller K. *Journal of Cell Science* 1985; 76: 155-65.
- [35] Suda T, Takahashi N, Udagawa N, Jimi E, Gillespie MT, Martin TJ. *Endocrine Reviews* 1999; 20: 345-57.
- [36] Negishi-Koga T, Shinohara M, Komatsu N, Bito H, Kodama T, Friedel RH, et al. *Nat. Med.* 2011; 17: 1473-80.
- [37] Zhao C, Irie N, Takada Y, Shimoda K, Miyamoto T, Nishiwaki T, et al. *Cell Metabolism* 2006; 4: 111-21.
- [38] Diercke K, Sen S, Kohl A, Lux CJ, Erber R. *Journal of Dental Research* 2011; 90: 1108-15.
- [39] Salaita K, Nair PM, Petit RS, Neve RM, Das D, Gray JW, et al. *Science* 2010; 327: 1380-5.
- [40] Irie N, Takada Y, Watanabe Y, Matsuzaki Y, Naruse C, Asano M, et al. *Journal of Biological Chemistry* 2009; 284: 14637-44.



Improvement of the Sensitivity in Bead-Based Electrochemical Impedance Spectroscopy (BEIS) Biosensor Using Microwells



Ji Yoon KANG
Center for
BioMicrosystems
Brain Science Institute
jykang@kist.re.kr

Introduction

Enzyme-linked immunosorbent assay (ELISA) is a prevalent immunoassay method which generally detects biomolecules above the range of a few tens of pg/mL [1]. However, some target biomolecules exist in very low concentrations within a sample so that ELISA can fail to detect them and may not report meaningful information. Therefore, it is important to provide a highly-sensitive, reliable, low-cost detection method for the early diagnosis and precise monitoring of a disease detectable in blood. Various types of biosensors have been developed for use as immunoassay devices based on several approaches based on electrochemical [2-7], optical [8-11], electrical [12-16], and mechanical transducer [17, 18] principles. Among these approaches, electrochemical sensors and nanotechnology (NT)-based field effect transistor (FET) sensors using nanowires [13, 19] or carbon nanotubes [20] are the most promising devices yet found for detecting biomolecules in a low concentration range of 10-100 fg/mL [19, 21-23]. However, it has been difficult to commercialize NT-based FET sensors due to the long-term instability of their electrical characteristics caused by the diffusion of ions from high ion-strength buffers into gate oxides [24].

Electrochemical sensors are advantageous due to their inherent simplicity, low cost of fabrication, and reliability in detecting biomarkers [25]. Electrochemical impedance spectroscopy (EIS) sensors measure changes in the electrical impedance spectrum generated by the interactions between biomarkers and receptors. The region for receptor immobilization

is mostly on the surfaces of the electrodes or in the gaps between electrodes, and the changes in the electrical properties that are caused by the interactions between antibodies and antigen can be measured. Unfortunately, the direct immobilization of antibodies on the surface of the electrodes hinders the repeated use of EIS sensors and causes problems in their calibration. Hence, a particle-based, renewable, electrochemical immunosensor was proposed that used magnetic beads and gold nanoparticle labeling [26]. The antibody-conjugated magnetic beads were attracted to the surface of a carbon paste sensor by a magnetic field, then the beads were washed away from the surface of the sensor for reuse. Several groups have reported using particle-based EIS sensors to detect different target molecules [21, 26, 27]; however, the limits of detection (LODs) of these devices are significantly higher (> 100 pg/ml) than those of recently reported EIS sensors which use signal amplification (5.4 pg/ml) [28] or nanochannels (250 fg/mL) [29].

In order to overcome the low sensitivity of conventional particle-based EIS sensors, we proposed a new bead-based EIS (BEIS) sensor with high sensitivity as well as reusability. This sensor system is composed of an EIS electrode array which includes microwells, a magnetic bar to manipulate magnetic beads and a simple straight microfluidic channel to inject the magnetic beads and other reagents. To test for a specific target biomarker, the magnetic beads are coated with the appropriate antibody and trapped in the microwells. A sample is then injected and a reaction with antigens triggers changes in the impedance of the surfaces of the beads. Differences between the beads in the biosensor and beads incubated in a negative control sample can then be evaluated. After any differences are measured, the used beads can be replaced with new beads of the same or a different antibody, thus allowing the reuse of the BEIS platform. The microwell array structure enhances the sensitivity of impedance testing by concentrating the electric field on the surfaces of the magnetic beads and also improves reliability by maintaining a uniform number of magnetic beads.

The performance of the BEIS platform with a

microwell array was demonstrated by the immunoassay of prostate specific antigen (PSA), which is a protein produced by the prostate gland and which is a sensitive biomarker of prostate cancer or other prostate disorders [30, 31]. We have also tested the performance of BEIS with a microwell array by detecting PSA in a phosphate-buffered saline (PBS) buffer as well as in human plasma, and the LOD of the proposed sensor platform was comparable to that of nano-FET. This biosensor represents a promising sensor platform since it can provide a non-labeled, low-cost, reusable sensor that has high sensitivity.

Materials and methods

Reagents and preparation of samples

For the preparation of magnetic beads with prostate-specific antigen (PSA) antibody, we purchased tosylactivated magnetic beads (Dynabeads M-280, diameter ~ 2.8 μm) and monoclonal anti-PSA (10-P20A) from Invitrogen and Fitzgerald Industries, USA, respectively. The anti-PSA antibody of 1 mg/ml was immobilized to the tosylactivated beads in 0.1 M phosphate buffer by incubation for 24 h on a roll mixer in an incubator at 37°C. The beads were washed with PBST (PBS including 1% Tween 20), and then concentrated to 30 mg/mL in PBST (0.01% Tween 20). The magnetic beads were diluted in 0.1x PBS (mixture with 1x PBS and deionized water) at a concentration of 3 ng/mL. For detection of the PSA antigen (30C-CP1017) that was purchased from Fitzgerald Industries, PSA was prepared with various concentrations ranging from 10 fg/mL to 100 pg/mL with 0.1x PBS buffer solution.

Structures of the BEIS platform and experimental procedures

Figure 1A shows photographs of a fabricated BEIS sensor and a BEIS platform with a PDMS microfluidic channel. A layer of SU-8 was used to construct a

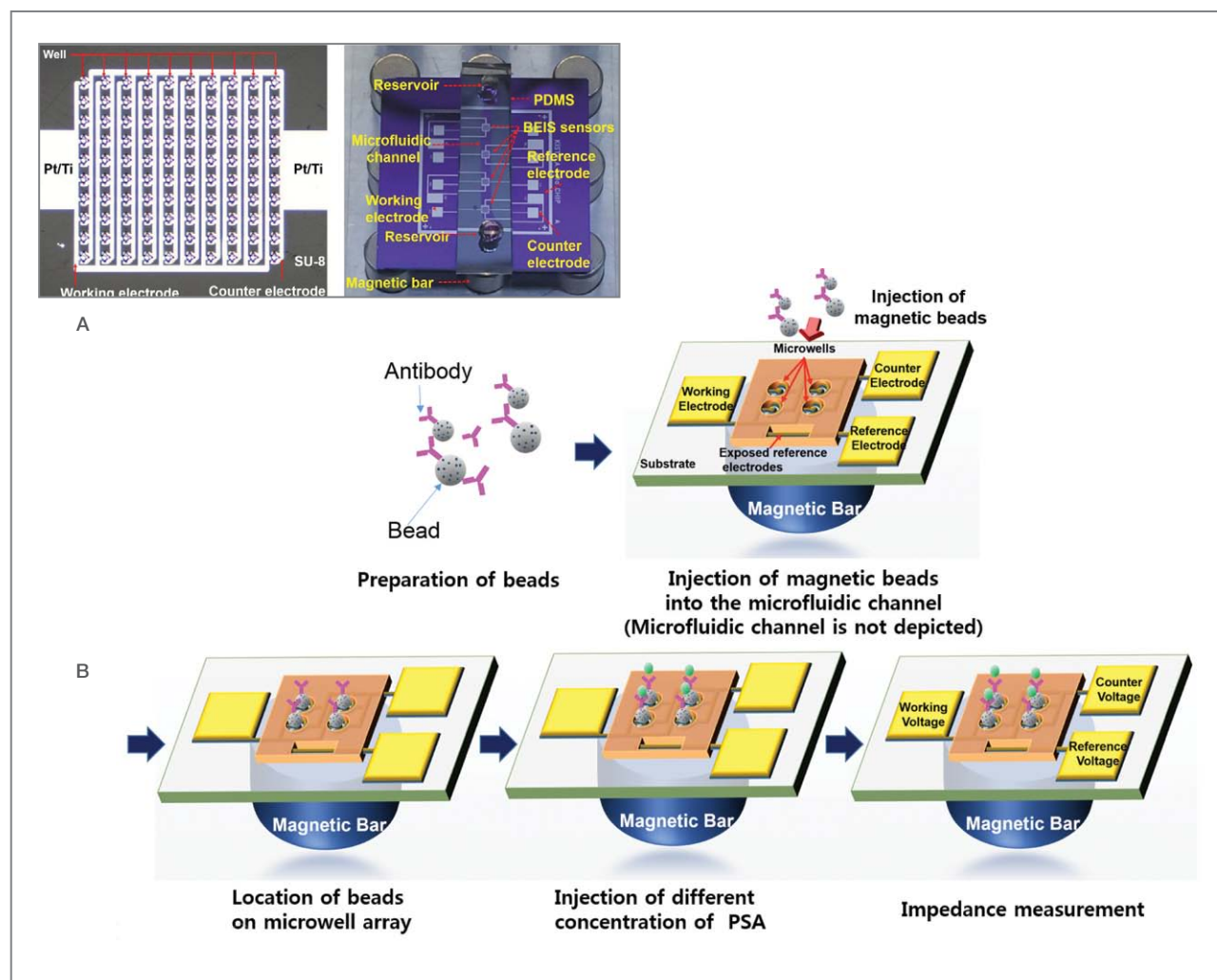


Figure 1 Images of a proposed BEIS (beads-based electrochemical impedance spectroscopy) platform and experimental procedures. (A) Images of the fabricated BEIS sensor and the BEIS platform with a magnetic bar. (B) Schematics of experimental procedures using the BEIS platform.

microwell on each electrode pair to concentrate the electric field inside the microwell, thus preventing undesirable current leakage between the metal line and the buffer solution in the microfluidic channel. The platform had multiple microarrays of BEIS sensors with a microfluidic channel on a slide glass or a silicon dioxide substrate, and a permanent magnetic bar beneath the slide glass. Each BEIS sensor consisted of a 10 x 10 array of a microwell with an electrode pair (the width of a working/counter electrode $\sim 2 \pm 0.2 \mu\text{m}$, gap $\sim 2 \pm 0.2 \mu\text{m}$). The individual well diameter and depth were 6 ± 0.5

μm and $5 \pm 0.2 \mu\text{m}$, respectively. Based on this design, each microwell could capture two or three magnetic beads given a bead diameter of $2.8 \mu\text{m}$.

Figure 1B shows the experimental procedure using a BEIS platform. After attaching the anti-PSA antibody onto the magnetic beads, the beads were injected into the microfluidic channel at a flow rate of $2 \mu\text{l}/\text{min}$ and attracted into the microwell array by a magnetic bar located beneath the bottom of the sensor. The residual beads on the SU-8 surface were then removed by the injection of PBS buffer solution. After the washing step, a

solution of PSA antigen was injected into the microfluidic channel at a flow rate of $2 \mu\text{l}/\text{min}$. The flow was stopped for 10 min while the PSA antigen fully diffused into the bottom of the microwell array and reacted with the antibody on the surface of the beads. After reaction between the anti-PSA antibody and antigen, the PBS buffer was used to remove nonspecific binding for a few minutes. The impedance of the BEIS platform was measured after stopping the flow of solution. The last two steps were repeated using different PSA concentrations to measure the change in the impedance of the magnetic beads as a function of PSA concentration. When a BEIS sensor was characterized, measurement was based on a three-electrode setup using an Autolab measurement

system (Autolab® PGSTAT302N). For this configuration, an additional electrode was located outside of the BEIS sensor (reference electrode in Figure 1A). During frequency sweeping, the frequency was varied from 1 Hz to 1 MHz, while the amplitude of voltage was fixed at 50 mVrms.

Results and discussion

Operation principles based on electric field and equivalent electrical circuit

To investigate the effect of the microwell on the distribution of electric fields, a single well was modeled and simulated in COMSOL® software (Figure 2) [32]. The simulation results confirmed that the distributions of electrical potential and electric field are strongly affected by a microwell. When a bead was positioned on the electrode (Figure 2A, left), the lines of electrical potential around/in a bead were more sparse than when a bead was near the edge of the electrode. If a bead was positioned near the edge of the electrodes, the distributions of electrical potential were almost the same around a bead regardless of the presence of a microwell (Figure 2A, middle and right). However, it is difficult to locate a bead in a specific position without a guide structure such as the microwell. In addition, it was noted that the electrical potential distributions were weak above the SU-8 layer and that most of the potential between the electrode and the buffer solution dropped within the SU-8 layer. A small decrease in the potential above the SU-8 layer generated very small current leakage. Electric fields were more concentrated around a bead than in the cases without a microwell (Figure 2B, left and middle). Although three beads were packed in a microwell, the electric fields were effectively confined around them (Figure 2B, right). Therefore, it is apparent that the structure of the microwell facilitated the location of a bead between the electrodes and also focused the electric fields on the beads.

The distribution of electrical potential is very

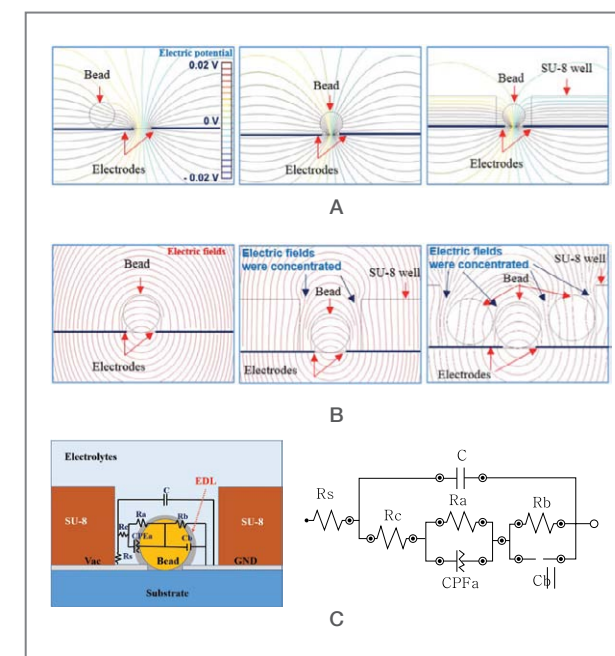


Figure 2 Simulation results from COMSOL software of the effect of a microwell on the distributions of electrical potential and electric field, and equivalent electrical circuit for a BEIS platform. (A) Distribution of electrical potential (left: a bead located on electrode without a microwell; middle: a bead located between electrodes without a microwell; right: a bead located between electrodes with a microwell). (B) Distribution of electric field (left: a bead located between electrodes without a microwell; middle: a bead located between electrodes with a microwell; right: three beads located between electrodes with a microwell). (C) Structure of a BEIS sensor with consideration of electrical components (left) and the derived equivalent electrical circuit (right).

important for understanding the sensing mechanism of a BEIS sensor. As the lines of electrical potential around the beads become dense, the electric field strength around a bead increases. Then more ion charges in the buffer solution will cover the surface of a bead at a lower frequency to form the electrical double layer (EDL). The electric fields are stronger in the bottom part of a bead, which means that a thicker EDL is generated there than in the other surface regions. When charged biomolecules bind to the surface of a bead, they perturb the EDL, and the changes in the EDL layer resulting from the deformation of electrical field and ion diffusion result in measurable changes in the impedance [29]. Therefore, the higher electric field forces more charges on the beads to form the EDL region, and they also push more biomolecules into the EDL region close to bead surfaces. In terms of the net charge of the beads, the absorption or reaction of biomolecules modulates the net charges on the beads, and ion diffusion near the EDL region compensates for the change. Since the isoelectric point of PSA is between 6.8-7.5, PSA has negative charges in the PBS buffer (pH ~7.4). As the concentration of PSA antigen increases, more PSA antigens accumulate on the surfaces of the magnetic beads and more negative charges on the surfaces of the beads in the EDL region. Therefore, the increment of PSA concentration results in decreasing the impedance of a BEIS sensor due to the ion diffusion caused by the perturbation of the EDL region.

The changes in impedance that occur when biomolecules are absorbed can also be explained by an electrical equivalent circuit. The BEIS sensor was modeled as an equivalent electrical circuit in the form of a sensor (Figure 2C). It is composed of one constant-phase element, two capacitors, and four resistors. R_s is electrolyte resistance, R_c is contact resistance between the electrolyte and the EDL region, C is capacitance between electrodes, and CPE_a and R_a are a constant-phase element and resistance between the electrolyte and antigen in the EDL region, respectively. C_b and R_b are capacitance and resistance between the antigen in the EDL region and the beads, respectively. The changes in PSA concentration will induce changes in R_c , CPE_a , R_a

and C_b in the equivalent electrical circuit. In particular, R_c and CPE_a are affected by the ion diffusion between the electrolytes and the antigen in the EDL; R_a and C_b are related to the charge amount of the antigen on the beads. The values of R_c , CPE_a , R_a and C_b will show different trends as the concentration of PSA antigen increases. R_c and R_a are reduced by increasing ion diffusion and changes in the surface charge caused by PSA antigen. CPE_a and C_b are increased by increasing the concentration and the effective binding area of PSA antigen on the beads. These changes cause a decrease in the total impedance of the equivalent circuit.

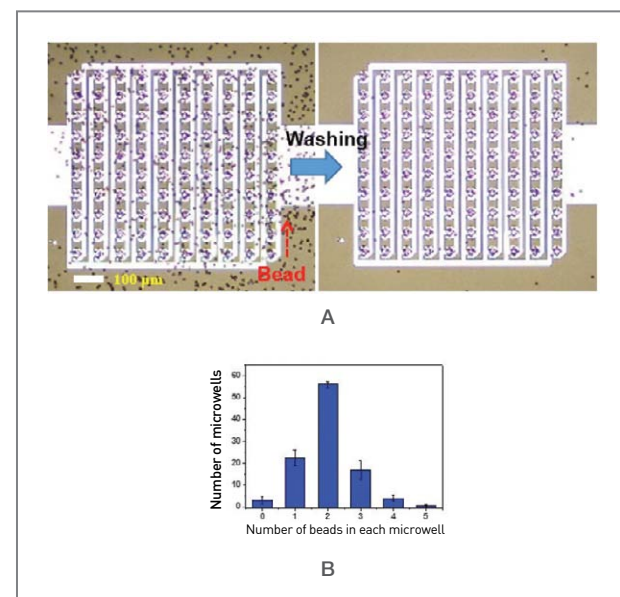


Figure 3 The results of control experiments with magnetic beads in a BEIS platform. (A) Image of pre-treated beads after injection into the microfluidic channel (left) and image of pre-treated beads after washing showing only a few beads remaining on the surface of SU-8 2005 (right). (B) Distribution graph for the number of beads settling in the wells of a BEIS sensor (N=3, total number of microwells in a BEIS sensor = 100).

Control experiments with magnetic beads

Before conducting the whole process of PSA detection, we first checked the distribution of beads in the microwell array after the injection of the magnetic bead solution. The number of beads tended to increase

slightly when the injection time was longer or the flow rate was slower. The residue beads on the surface of SU-8 were washed away with a slightly higher flow rate than that of the bead injection flow. Flow rates of 2 μl/min and 10 μl/min were used for the bead injection and washing steps, respectively. After the washing step, we could still observe some beads remaining on the SU-8 passivation surface (Figure 3A). However, those beads did not affect the impedance measurement of the captured beads, since the passivation layer blocked any effect from the uncaptured beads. The distribution of the number of beads followed the Poisson distribution, and it was difficult to find a microwell that had more than five beads in the experiments (Figure 3B). In most cases, the number of beads trapped in a microwell ranged from one to three, and the microwells with two beads were dominant in every experiment.

Results of PSA detection with a BEIS platform

The concentration of PSA antigen was changed from 1 fg/mL to 10 ng/mL in the PBS buffer. Figure 4 shows the Nyquist, impedance and phase results with varying concentrations of PSA antigen as a function of frequency. It is clear that the changes in the concentration of PSA antigen can effectively modulate the output responses from a BEIS platform due to changes in the charge on the beads caused by the PSA antigen. Note that the impedance changes were dominant at lower frequencies while the phase changes occurred in a medium frequency range (1 kHz ~ 100 kHz). However, the number of beads and the ion concentration of PBS buffer also affects the phase values in the medium frequency range. Therefore, it is difficult to separate the effect of PSA antigen on the phase plot from the mixed signal possible from the number of beads and the ion concentration of the buffer solution. Fortunately, the number of beads did not affect the impedance significantly at lower frequencies if the buffer solution was not changed during the experimental procedure. Therefore, it is recommended that a low frequency impedance be chosen to determine the concentration of PSA antigen using a pre-defined

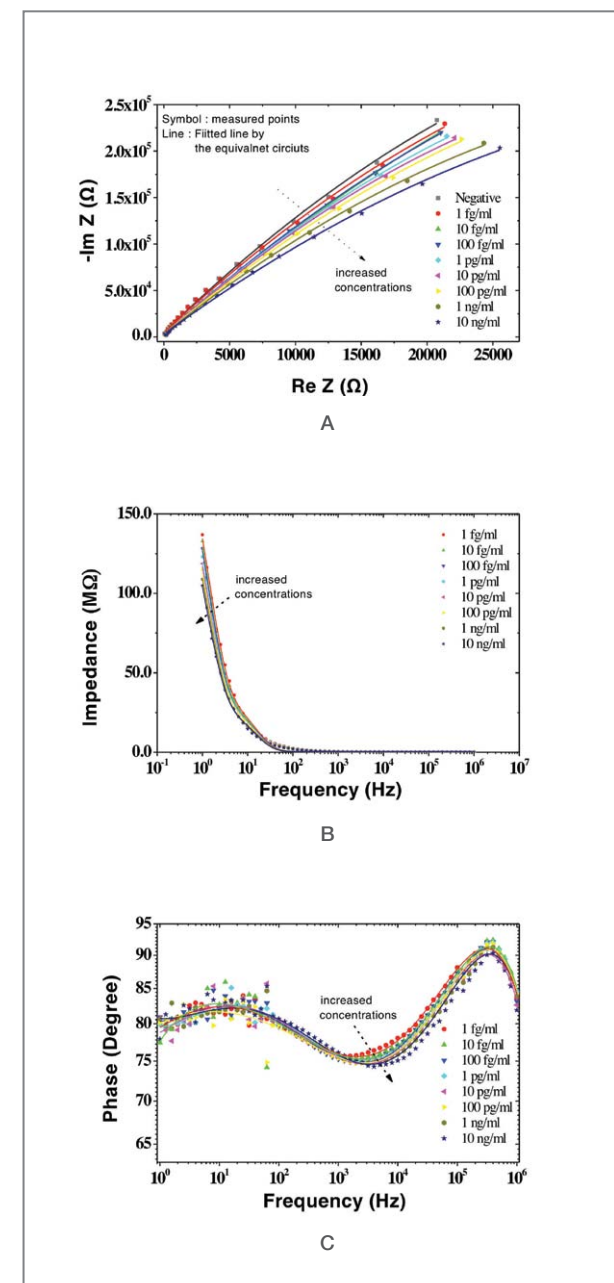


Figure 4 Output responses from a BEIS platform at various concentrations of PSA antigen. (A) Nyquist responses with varying concentration of PSA antigen. (B) Impedance responses as a function of frequency. (C) Phase responses as a function of frequency.

buffer solution. The responses measured and the results extracted from the equivalent circuit (Figure 2C) are exhibited as symbols and lines, respectively, in Figure

4. The extraction was conducted in three steps with the equivalent electrical circuit. First, the four parameters of R_c , R_a , CPE_a , and C_b were initially fitted by NOVA® software using the measured responses as a function of the concentration of PSA antigen to find the dominant parameter. It was assumed that the other three parameters of R_s , C and R_b are constant. Secondly, each parameter of R_c , R_a , CPE_a , and C_b was arranged according to varying concentrations of PSA and a linear relationship extracted by linear fitting for each parameter. Third, lines at the different concentrations (shown in Figure 4) were collected by applying all refined values of R_c , R_a , CPE_a , C_b to the equivalent circuit in the simulation mode in NOVA software, where refined values are deducted from the fitted lines at specific concentrations. All of the lines that were extracted coincided well with the symbolic responses with chi-squared in the range of 0.045-0.061. Although the chi-squared values are slightly higher than 0.05, these results imply that R_c , R_a , CPE_a , and C_b are the dominant factors in the equivalent electrical circuit, rather than R_s , C and R_b .

Sensitivity and limit of detection of a BEIS platform for PSA detection

In order to evaluate the frequency effect on output responses as a function of PSA antigen, the outputs of impedance were plotted, as shown in Figure 5. We tested multiple devices ($N=4$) in a platform to evaluate the LOD of detecting PSA in PBS using average slope. Figure 5A shows the average impedance as a function of the concentration of PSA at 1 Hz; the sensitivity was approximately 5.3 M Ω /dec. However, defining the sensitivity as the slope of absolute impedance is not advisable since devices display some variation in sensitivities caused by different impedance levels. This can occur even though they were fabricated at the same time or in the same batch. To resolve the variation of sensitivity due to differences from device to device, we defined a normalized sensitivity as the ratio of impedance changes at a concentration of PSA antigen normalized by the initial reference impedance as:

where, Z_{PSA} and Z_{Buffer} are the impedance at a concentration

$$\text{Normalized Sensitivity (\%/dec)} \sim \frac{|Z_{PSA} - Z_{Buffer}|}{Z_{Buffer}} \times 100 \quad (1)$$

of PSA antigen in buffer solution and the impedance in only buffer solution, respectively.

Normalized impedance as converted by Eq. 1 (Figure 5B) results in a normalized sensitivity of approximately 3.6 %/dec. The error bar at 1 fg/ml of PSA antigen is so large that some of the sensors could not distinguish between the signal change of PBS buffer and that of 1 fg/mL of PSA antigen. Above 10 fg/mL of PSA antigen, the error bars were small enough to discriminate the value of the next point. Hence, it is reasonable to define the LOD of a BEIS platform as above 10 fg/mL. This LOD is comparable to that of a nanotechnology-based biosensor [19].

Next, human plasma was spiked with known concentrations of PSA in the range of 100 fg/mL and 10 ng/mL. To determine the initial reference impedance (Z_{Buffer}) of human plasma in a BEIS platform, human plasma was injected into a microfluidic channel for 5 min and washed by 0.1x PBS buffer, and the impedance was used as an initial reference. All impedance levels with varying concentrations of PSA in plasma were measured and plotted, as shown in Figures 5C and 5D. The impedance levels and slope of impedance were different from those of the previous PSA experiments in PBS buffer due to the changes in the fabricated devices (Figure 5C). However, the normalized sensitivity was 3.5 %/dec, which was close to that of PSA in PBS (3.6%/dec). Hence, the normalized sensitivity was useful to compensate for the variations in the impedances of the devices. The linearities in Figures 5B and 5D were about the same in the PBS buffer as the human plasma, i.e., 0.983 and 0.981, respectively. The LOD of PSA in human plasma was estimated as approximately 100 fg/mL, which was higher than the previous LOD of PSA in PBS by a factor of 10, but it is still comparable to that of the best EIS sensors or nanotechnology-based biosensors. In addition, we checked the reusability of a

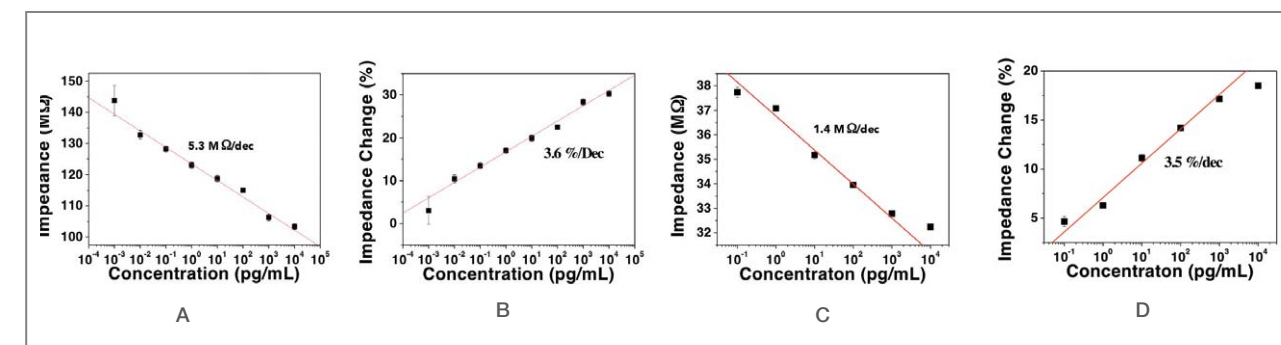


Figure 5 Sensitivities of BEIS platforms for detection of PSA antigen in PBS buffer and in human plasma. (A) Sensitivity of 5.3 M Ω /dec at 1 Hz in PBS buffer. (B) Sensitivity in percentage terms of 3.6 %/dec at 1 Hz in PBS buffer. (C) Sensitivity of 1.4 M Ω /dec at 1 Hz in human plasma. (D) Sensitivity in percentage terms of 3.5 %/dec at 1 Hz in human plasma.

BEIS platform to detect the PSA antigen and confirmed that the sensor can be reused 3-5 times.

Conclusion

Particle-based reusable electrochemical immunosensors using magnetic beads have the demonstrated advantage of reusability, but their detection limit (>100 pg/mL) is greater than that of recently-reported EIS sensors. As a result, BEIS biosensors have trouble detecting the early stages of disease due to their relatively low sensitivity. We proposed a novel BEIS platform with a microwell array to push the LOD of reusable EIS devices to sub pg/mL levels and sustain the recyclability of the BEIS sensor. Microwell arrays were used to concentrate the electric field on the surfaces of magnetic beads to improve the sensitivity of the device.

The performance of the BEIS platform with a microwell array was confirmed by the immunoassay of prostate specific antigen (PSA). The experimental results show that the BEIS platform with a microwell array can detect PSA with much higher sensitivity at low frequency. It could detect levels of a few tens of fg/mL in the PBS buffer and levels of a few hundreds of fg/mL of PSA antigen in human plasma. The LODs of our proposed BEIS platform are comparable to those of advanced biosensors based on nanotechnology, but

BEIS has the advantages of a simple fabrication process, low cost, and reusability. Since we demonstrated that the BEIS platform with a microwell array is a highly sensitive and rugged non-labeled biosensor platform, it is expected to become a valuable platform in immunoassays that require high sensitivity.

Note

This article and images are drawn from “Sensitivity Enhancement of Bead-based Electrochemical Impedance Spectroscopy (BEIS) biosensor by electric field-focusing in microwells” in *Biosensors and Bioelectronics*, Vol. 85, pp 16~24.

References

- [1] Johnson ED, Kotowski TM. *J. Forensic Sci.* 1993; 38(2): 250-258.
- [2] Akter R, Kyun Rhee C, Aminur Rahman M. *Biosens. Bioelectron.* 2014; 54(0): 351-357.
- [3] Chiriaco MS et al. *Analyst.* 2013; 138(18): 5404-5410.
- [4] Chuah K, Lai LMH, Goon IY, Parker SG, Amal R, Gooding J. *J. Chem. Commun.* 2012; 48(29): 3503-3505

- [5] Hu Y, Zuo P, Ye BC. *Biosens. Bioelectron.* 2013; 43(0): 79-83.
- [6] Mao K. et al. *Anal. Biochem.* 2012; 422(1): 22-27.
- [7] Zhang Y et al. *Biosens. Bioelectron.* 2015; 68(0): 343-349.
- [8] Lee JU, Nguyen AH, Sim SJ. *Biosens. Bioelectron.* 2015; 74(0): 341-346.
- [9] Brazhnik K et al. *Nanomed. Nanotechnol. Biol. Med.* 2015; 11(5): 1065-1075.
- [10] Ewers M, Sperling RA, Klunk WE, Weiner MW, Hampel H. *Trends Neurosci.* 2011; 34(8): 430-442.
- [11] Haes AJ, Chang L, Klein WL, Van Duyne RP. *J. Am. Chem. Soc.* 2005; 127(7): 2264-2271.
- [12] Gao A. et al. *Nano Lett.* 2012; 12(10): 5262-5268.
- [13] Huang YW et al. *Anal. Chem.* 2013; 85(16): 7912-7918.
- [14] Luo X, Davis JJ, *Chem. Soc. Rev.* 2013; 42(13): 5944-5962.
- [15] Oh J et al. *Biosens. Bioelectron.* 2013; 50(0): 345-350.
- [16] Choi JH, Kim HS, Choi JW, Hong JW, Kim YK, Oh BK. *Biosens. Bioelectron.* 2013; 49(0), 415-419.
- [17] Wu G, Datar RH, Hansen KM, Thundat T, Cote RJ, Majumdar A. *Nat. Biotech.* 2001; 19(9): 856-860.
- [18] Lee JH, Hwang KS, Park J, Yoon KH, Yoon DS, Kim TS. *Biosens. Bioelectron.* 2005; 20(10): 2157-2162.
- [19] Kim A et al. *Appl. Phys. Lett.* 2007; 91(10): 103901.
- [20] Li C et al. *J. Am. Chem. Soc.* 2005; 127(36): 12484-12485.
- [21] Centi S, Tombelli S, Minunni M, Mascini M. *Anal. Chem.* 2007; 79(4): 1466-1473.
- [22] Mohd Azmi MA et al. *Biosens. Bioelectron.* 2014; 52(0): 216-224.
- [23] Gao A, Lu N, Dai P, Fan C, Wang Y, Li T. *Nanoscale* 2014; 6(21): 13036-13042.
- [24] Wen X, Gupta S, Wang Y, Nicholson TR, Lee SC, Lu W. *Appl. Phys. Lett.* 2011; 99(4): 043701.
- [25] Rusling JF. *Anal. Chem.* 2013; 85(11): 5304-5310.
- [26] Liu G, Lin Y. *J. Nanosci. Nanotechnol.* 2005; 5(7): 1060-1065.
- [27] Sarkar P, Ghosh D, Bhattacharyay D, Setford SJ, Turner APF. *Electroanalysis* 2008; 20(13): 1414-1420.
- [28] Yang J, Wen W, Zhang X, Wang S. *Microchim. Acta.* 2015; 182: 1855-1861.
- [29] Nagaraj VJ, Jacobs M, Vattipalli KM, Annam VP, Prasad S,

- Env. Sci. Process.* 2014; 16(1) 135-140.
- [30] Jia-dong L et al. *J. Micromech. Microeng.* 2014; 24(7): 075023.
- [31] Shariat SF, Semjonow A, Lilja H, Savage C, Vickers AJ, Bjartell A. *Acta Oncologica.* 2011; 50(S1): 61-75.
- [32] Pryor RW. *Multiphysics modeling using COMSOL: a first principles approach.* Jones & Bartlett Publishers, 2009.



Technical Review

Highly Conductive 2D Layered Materials for Electromagnetic Interference Shielding



Chong Min KOO

Materials Architecturing
Research Center,
Materials and Life
Science Research
Division
koo@kist.re.kr



Faisal SHAHZAD

Materials Architecturing
Research Center,
Materials and Life
Science Research
Division
efs2000@yahoo.com

Introduction

Electromagnetic interference (EMI) is emitted by any electronic device that transmits, distributes, or utilizes electrical energy. As electronics and their components operate at faster speeds and become smaller in size, there will be a significant increase in such interference resulting in the potential malfunctioning and degradation of electronic devices [1-5]. With the rapid proliferation of these devices, it is imperative that the harmful effects of EMI on the performance of equipment and its components be explored.

Properties required for EMI shielding

For an EMI shielding material to be effective, it must both reduce undesirable emissions and protect the component from stray external signals. The primary mechanism of EMI shielding is to reflect incoming radiation using charge carriers that interact directly with the electromagnetic (EM) shield [6]. As a result, shielding materials need to be electrically conductive; however, conductivity is not the only requirement. A secondary mechanism of EMI shielding occurs when EM radiation interacts with the electric and/or magnetic dipoles of the shielding material. High electrical conductivity is the primary factor in determining reflectivity and absorption characteristics of the shield [7]. However, a third mechanism, accounting

for multiple internal reflections, is less studied, but contributes significantly to EMI shielding effectiveness. These internal reflections arise from scattering centers and interfaces or defect sites within the shielding material resulting in scattering and then absorption of EM waves (EMW) [1, 8, 9].

Common EMI shielding materials

In earlier days, metal shrouds were the material of choice to mitigate EMI interference [1-4, 6-10], but with the increasing use of smaller devices and components, susceptibility to corrosion coupled with high density has made metals less desirable shield materials [8]. As a result, low-cost, lightweight, high strength and easy-to-fabricate shielding materials are very much needed. Polymer-matrix composites with embedded conductive nano fillers have become a popular alternative for EMI shielding due to their good processability and low densities [10]. Carbon-based fillers, particularly carbon nanotubes and graphene, have attracted much interest in recent years [11], but no major breakthrough has been reported thus far. New EMI shielding materials that can meet the requirements of next-generation telecommunication equipment and wearable devices are sorely needed.

Concept of using MXene as an EMI shielding material

MXenes are a recently discovered unique family of two-dimensional (2D) transition metal carbides and/or nitrides, with a formula of $M_{n+1}X_nT_x$, where M is an early transition metal (e.g., Ti, Zr, V, Nb, Ta or Mo) and X is carbon and/or nitrogen. Due to the aqueous medium used during synthesis, MXene flakes are terminated with surface moieties (T_x), such as a mixture of $-OH$, $=O$ and $-F$ [12]. Exceptional electrical conductivity and good mechanical properties coupled with hydrophilicity make

MXenes a good choice for use in polymer composites [12] and energy storage devices [13] as they are capable of intercalating organic molecules and ions. So far, about 20 different MXenes have been reported [12, 14, 15]. The most commonly studied MXene, $Ti_3C_2T_x$, has been incorporated into different polymer matrices, such as polyvinyl alcohol (PVA), ultrahigh molecular weight polyethylene (UMWPE) and polypyrrole (PPy) [16,17]. Sodium alginate (SA) is a linear polysaccharide copolymer derived from seaweed. Natural biomaterials, like SA, are potentially ideal candidates for polymeric matrices since they are abundant, environmentally friendly, and mechanically robust [18]. SA has oxygen-containing functional groups ($-OH$, $-COO$, and $=O$), which can potentially facilitate the formation of hydrogen bonding with the termination groups of MXenes. To date, no MXene-SA composites have been reported in literature; therefore, we were motivated to explore MXene and its polymer composites due to their high electrical conductivity, which is a prime requirement for EMI shielding.

In this work, we report the synthesis and EMI shielding performance of highly flexible MXene films ($Ti_3C_2T_x$, $Mo_2TiC_2T_x$, and $Mo_2Ti_2C_3T_x$) and nacre-like MXene polymer composite films ($Ti_3C_2T_x$ -SA). All freestanding films were made by vacuum-assisted filtration from the colloidal solutions of pure MXenes or its composites. The schematic representation of the 2D layered structure for MXene-SA composites is displayed in Figure 1. The highest EMI SE performance of 92 dB

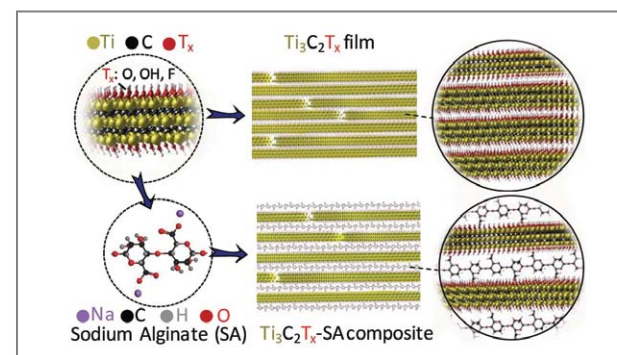


Figure 1 Schematic of $Ti_3C_2T_x$ and $Ti_3C_2T_x$ -SA composite films.

was recorded for $Ti_3C_2T_x$ film (45 μm) and 57 dB for $Ti_3C_2T_x$ -SA (8 μm , 10 wt.% SA) film, respectively. These MXene films have additional advantages such as easy processing, high conductivity, relatively low density, and mechanical flexibility. To our knowledge, this is the highest EMI SE performance ever reported for synthetic materials of similar thicknesses and is comparable to pure metals. This finding opens up a large family of new 2D materials for use as EMI shielding materials.

Experimental

Materials

Lithium fluoride (LiF, Alfa Aesar, 98.5%), hydrofluoric acid (HF, Acros Organics, 49.5 wt.%), hydrochloric acid (HCl, Fisher Scientific, 37.2%), alginic acid sodium salt (sodium alginate, Sigma Aldrich) and tetrabutylammonium hydroxide (TBAOH, Acros Organics, 40 wt.% solution in water) were used as received. Copper (10 μm) and aluminum foils (8 μm) were purchased from Alfa Aesar.

Synthesis of Ti_3AlC_2 (MAX phase)

Ti_3AlC_2 was synthesized as described elsewhere [1]. The as-synthesized powders were crashed and sieved through a 400 mesh size sieve ($\leq 38 \mu m$ particle size) and collected for etching. The powders were stored under inert atmosphere to avoid any oxidation.

Minimally intensive layer delamination (MILD) synthesis of $Ti_3C_2T_x$

$Ti_3C_2T_x$ was synthesized through a modified etching route to the clay method [2]; a higher molar ratio of LiF: Ti_3AlC_2 than the clay method was employed, and no sonication was used for the delamination step. Briefly, the etchant solution was prepared by first completely dissolving 1 g LiF in 20 ml of 6 M HCl in a 100 ml-

polypropylene plastic vial, after which 1 g of Ti_3AlC_2 (MAX) was gradually added to the etchant solution over a period of 10 min and the reaction was allowed to proceed at 35°C for 24 h. The as-etched product was washed copiously with deionized water (DI water) via centrifugation several times at 3500 rpm for 5 min per cycle until a stable dark-green supernatant solution of $Ti_3C_2T_x$ flakes, with a pH of ≥ 6 , was obtained. At this stage, the dark supernatant was decanted, leaving behind a swelled clay-like sediment. Adding DI water to the sediment and manually shaking it for < 5 min resulted in delamination of the flakes. This was followed by 1 h of centrifugation at 3500 rpm. The resulting supernatant had a MXene concentration of $\sim 1.5 \text{ mg ml}^{-1}$.

Synthesis of $Mo_2TiC_2T_x$ and $Mo_2Ti_2C_3T_x$

1 g of Mo_2TiAlC_2 was etched in a 10 ml solution (10 wt.% HF and 10 wt.% HCl) at 40°C for 40 h. The as-etched product was washed copiously with DI water until neutralized before being collected and dried in a vacuum oven overnight. $Mo_2Ti_2C_3T_x$ was synthesized by etching $Mo_2Ti_2AlC_3$ using similar conditions to that used in synthesizing Mo_2TiAlC_2 .

Delamination of $Mo_2TiC_2T_x$ and $Mo_2Ti_2C_3T_x$

1 g of $Mo_2TiC_2T_x$ and 1 g $Mo_2Ti_2C_3T_x$ were separately stirred in 50 ml of DI water containing 0.8 wt.% TBAOH for 2 h before collecting the colloidal solution via centrifugation after 1 h at 3500 rpm.

Preparing $Ti_3C_2T_x$ -sodium alginate (SA) composite

An aqueous SA solution with a concentration of 0.5 mg ml^{-1} was prepared by completely dissolving the required SA content into DI water. Subsequently, an aqueous $Ti_3C_2T_x$ colloidal solution, based on the desired final $Ti_3C_2T_x$ content, was added to the SA solution. The resultant mixture was then stirred for 24 h at room temperature (RT) yielding a series of aqueous $Ti_3C_2T_x$ -SA solutions with different initial $Ti_3C_2T_x$ content (90, 80,

60, 50, 30, 10 wt.%). Each aqueous $\text{Ti}_3\text{C}_2\text{T}_x$ -SA solution was filtered using a polypropylene membrane (Celgard pore size $0.064\ \mu\text{m}$) and allowed to dry for 24-72 h at RT. Samples were designated according to the following scheme: a 90 wt.% $\text{Ti}_3\text{C}_2\text{T}_x$ with 10 wt.% SA was referred to as 90 wt.% $\text{Ti}_3\text{C}_2\text{T}_x$ -SA. Pure $\text{Ti}_3\text{C}_2\text{T}_x$ film was filtered using the same method for comparison.

Preparation of freestanding films of MXene

All freestanding films were prepared via vacuum-assisted filtration (VAF) using Durapore filter membrane (polyvinylidene fluoride PVDF, Hydrophilic, with $0.1\ \mu\text{m}$ pore size) to make $\text{Ti}_3\text{C}_2\text{T}_x$, $\text{Mo}_2\text{Ti}_3\text{C}_2\text{T}_x$, and $\text{Mo}_2\text{Ti}_2\text{C}_3\text{T}_x$ films. All films were allowed to dry at RT before being easily peeled off as freestanding films and stored under vacuum for future use.

Results and discussion

Figure 2A shows the scanning electron microscopy (SEM) image of a $\text{Ti}_3\text{C}_2\text{T}_x$ MXene flake (sizes ranged from 1 to $5\ \mu\text{m}$) on an alumina filter. Figures 2B and 2C show the cross-sectional SEM images of the 50 wt.% $\text{Ti}_3\text{C}_2\text{T}_x$ -SA, and pristine $\text{Ti}_3\text{C}_2\text{T}_x$ films, respectively. In all composite loadings, the nacre-like layered stacking of the $\text{Ti}_3\text{C}_2\text{T}_x$ remained, similar to the pristine $\text{Ti}_3\text{C}_2\text{T}_x$ films. This characteristic was also confirmed by the presence of the $\text{Ti}_3\text{C}_2\text{T}_x$ (002) peak in all the $\text{Ti}_3\text{C}_2\text{T}_x$ -SA XRD patterns (Figure 2D). A decrease in the intensity of all the (00l) $\text{Ti}_3\text{C}_2\text{T}_x$ peaks in the composite samples was observed compared to that of the pristine $\text{Ti}_3\text{C}_2\text{T}_x$, due to the presence of SA in between the layers. The introduction of SA added disorder in stacking and separated MXene flakes. Additionally, a new peak around $\sim 4.4^\circ$ appeared after the addition of SA, and its intensity increased with SA content (compare the top two patterns in Figure 2D). This peak corresponds to a $\text{Ti}_3\text{C}_2\text{T}_x$ interlayer spacing of $\sim 10\ \text{\AA}$, a result of SA presence between MXene layers.

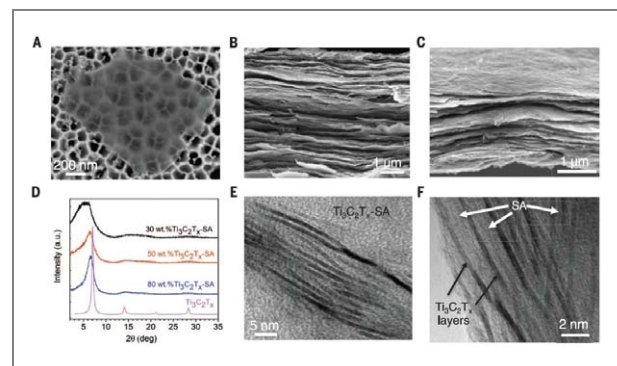


Figure 2 (A) SEM image of a $\text{Ti}_3\text{C}_2\text{T}_x$ flake on a filter. (B) SEM image of the 50 wt.% $\text{Ti}_3\text{C}_2\text{T}_x$ -SA composite. (C) SEM image of pure $\text{Ti}_3\text{C}_2\text{T}_x$. (D) XRD patterns of the pristine $\text{Ti}_3\text{C}_2\text{T}_x$ and its composite with SA at different loadings. (E and F) TEM images of 80 wt.% $\text{Ti}_3\text{C}_2\text{T}_x$ -SA and 30 wt.% $\text{Ti}_3\text{C}_2\text{T}_x$ -SA composite films, respectively.

In the case of 30 wt.% $\text{Ti}_3\text{C}_2\text{T}_x$ -SA, the broad (002) peak was between $\leq 4.4^\circ$ and 6.5° , which is due to the variable interlayer spacing between the MXene layers, ranging from >10 to $3.5\ \text{\AA}$. This shows that while SA molecules are intercalated between MXene layers, the latter still retains an ordered layered structure.

Figure 2E shows the cross-sectional transmission electron microscopy (TEM) images of the $\text{Ti}_3\text{C}_2\text{T}_x$ -SA composite films, confirming the intercalation of SA layers in between the MXene flakes. At higher $\text{Ti}_3\text{C}_2\text{T}_x$ filler loading, mostly stacks of $\text{Ti}_3\text{C}_2\text{T}_x$ flakes, with some individual flakes separated with SA, were observed. At lower $\text{Ti}_3\text{C}_2\text{T}_x$ concentrations, more individual $\text{Ti}_3\text{C}_2\text{T}_x$ flakes were separated with SA and a variety of different interlayer spacing was present (Figure 2F). This combination of different spacing between layers can explain the very broad range of the (002) peaks observed in 30 wt.% $\text{Ti}_3\text{C}_2\text{T}_x$ -SA XRD from $\leq 4.4^\circ$ to 6.5° .

Electrical conductivity and EMI shielding

Materials with large electrical conductivity are typically required to obtain high EMI SE values. Figure 3A presents the electrical conductivity of three different types of MXenes. A higher electrical conductivity in $\text{Mo}_2\text{Ti}_2\text{C}_3\text{T}_x$ was observed compared to $\text{Mo}_2\text{TiC}_2\text{T}_x$, which

is in agreement with previously reported results [19]. $\text{Ti}_3\text{C}_2\text{T}_x$ films showed the highest electrical conductivity among the studied samples, reaching $4600\ \text{S cm}^{-1}$. Such an excellent electrical conductivity arises from the high electron density of states near the Fermi level ($N(E_f)$) as predicted from Density Functional Theory (DFT) [20], making this MXene metallic in nature. On the contrary, lower electrical conductivity values of 119.7 and $297.0\ \text{S cm}^{-1}$ were observed for $\text{Mo}_2\text{TiC}_2\text{T}_x$ and $\text{Mo}_2\text{Ti}_2\text{C}_3\text{T}_x$, respectively, indicating a semiconductor-like temperature dependence of conductivity [15, 19].

Figure 3B shows the electrical conductivities of $\text{Ti}_3\text{C}_2\text{T}_x$ -SA polymer composites. With the addition of only 10 wt.% $\text{Ti}_3\text{C}_2\text{T}_x$, the conductivity of SA polymer rose to $0.5\ \text{S cm}^{-1}$. The huge improvement in electrical conductivity as compared to pristine polymer is likely due to the large aspect ratio of $\text{Ti}_3\text{C}_2\text{T}_x$ flakes that provides a percolation network at low filler loading. As the filler content is increased, electrical conductivity increased and reached $3000\ \text{S cm}^{-1}$ for 90 wt.% $\text{Ti}_3\text{C}_2\text{T}_x$ -SA composite.

Figure 3C shows the EMI shielding properties of three MXene films of different compositions with an average thickness of $\sim 2.5\ \mu\text{m}$. As a rule of thumb, higher electrical conductivity leads to better EMI SE performance. Consequently, $\text{Ti}_3\text{C}_2\text{T}_x$, with the largest electrical conductivity, gave the highest EMI SE among the studied MXenes. Since thickness plays a crucial role in the EMI SE of any material, EMI SE can easily be improved by increasing the thickness. To investigate this effect, we measured the EMI SE of six $\text{Ti}_3\text{C}_2\text{T}_x$ films with different thicknesses, as reflected in Figure 3D. The highest EMI SE value of 92 dB was recorded for a $45\text{-}\mu\text{m}$ thick film. In general, shielding can be easily enhanced by using thick conventional materials; however, material consumption and weight leave them at a disadvantage for use in aerospace and telecommunication applications. Therefore, it is of great importance to achieve high EMI SE values at a narrow thickness. The disadvantages associated with metals and other thick materials can be overcome by utilizing MXene in polymer matrices. To study this, we investigated $\text{Ti}_3\text{C}_2\text{T}_x$ -SA composites for EMI shielding. Here, a fixed thickness of $8\text{-}9\ \mu\text{m}$ was

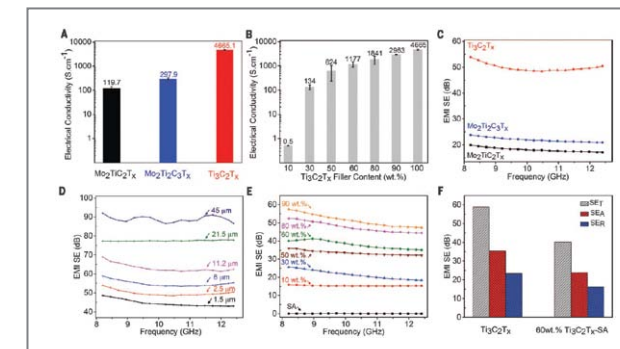


Figure 3 (A) Electrical conductivity of $\text{Mo}_2\text{TiC}_2\text{T}_x$, $\text{Mo}_2\text{Ti}_2\text{C}_3\text{T}_x$, and $\text{Ti}_3\text{C}_2\text{T}_x$. (B) Electrical conductivity of $\text{Ti}_3\text{C}_2\text{T}_x$ -SA composites. (C) EMI SE of $\text{Mo}_2\text{TiC}_2\text{T}_x$, $\text{Mo}_2\text{Ti}_2\text{C}_3\text{T}_x$, $\text{Ti}_3\text{C}_2\text{T}_x$ at thickness of $\sim 2.5\ \mu\text{m}$. (D) EMI SE of $\text{Ti}_3\text{C}_2\text{T}_x$ at different thicknesses. (E) EMI SE of $\text{Ti}_3\text{C}_2\text{T}_x$ -SA composites at thickness of $8\text{-}9\ \mu\text{m}$. (F) Total EMI SET and its absorption (SEA) and reflection (SER) mechanism in $\text{Ti}_3\text{C}_2\text{T}_x$ and 60 wt.% $\text{Ti}_3\text{C}_2\text{T}_x$ -SA samples at 8.2 GHz.

utilized for EMI measurements. With increasing MXene content, EMI SE increased and a maximum of 57 dB was recorded for the 90 wt.% $\text{Ti}_3\text{C}_2\text{T}_x$ -SA sample (Figure 3E). Shielding mechanisms due to absorption (SEA) and reflection in the $\text{Ti}_3\text{C}_2\text{T}_x$ ($6\ \mu\text{m}$) and 60 wt.% $\text{Ti}_3\text{C}_2\text{T}_x$ -SA ($\sim 8\ \mu\text{m}$) films are compared in Figure 3F at 8.2 GHz. In both cases, shielding due to absorption was the dominant mechanism rather than reflection.

Comparison of MXene performance to other reported studies

A comprehensive literature review of previously studied EMI shielding materials clearly indicates that MXenes and their polymer composites are the best EMI shielding materials produced to date. So far, the majority of research has focused on graphene [11, 21, 22], carbon nanotubes [23], iron-oxides [24], ferrites [25], iron-aluminum-silicon alloys [26], and metal based fillers [27] polymer composites. However, to satisfy the common commercial EMI shielding requirements (above 30 dB) [2], large thicknesses were usually employed. $\text{Ti}_3\text{C}_2\text{T}_x$ and $\text{Ti}_3\text{C}_2\text{T}_x$ -SA composites were compared with pure copper ($10\ \mu\text{m}$) and aluminum ($8\ \mu\text{m}$) foils. $\text{Ti}_3\text{C}_2\text{T}_x$, which has two orders of magnitude lower electrical conductivity than these metals, shows a similar EMI SE to those of

metals. For comparison, thermally reduced graphene oxide film (8.4 μm) that possessed lower electrical conductivity was also plotted and fell far below the other materials (Figure 4) [28]. A more extensive literature review indicates that ultrathin MXene films clearly outperform all of the known synthetic materials and reside at the top of the comparison chart (Figure 5A).

Recently, the concept of foam structures has garnered tremendous interest due to its potential for reducing the density of shielding materials which, in turn, could partially solve the problem of finding lightweight shielding materials for aerospace applications [1, 29, 30]. Specific EMI shielding effectiveness (SSE) was used as a criterion to evaluate different materials with respect to density. However, SSE alone is not a sufficient parameter to understand overall effectiveness, as higher SSE can simply be achieved at larger thicknesses, which then increases the weight of the final product. Therefore, a more realistic parameter is to divide SSE by the material thickness (SSE/t) [27, 32]. Such a parameter is highly valuable for determining the real effectiveness of a material by incorporating three important factors: EMI SE, density, and thickness. Interestingly, MXene and MXene-SA composites lie far ahead of the other materials of different categories. As a representative example, a 90 wt.% $\text{Ti}_3\text{C}_2\text{T}_x$ -SA composite sample gives

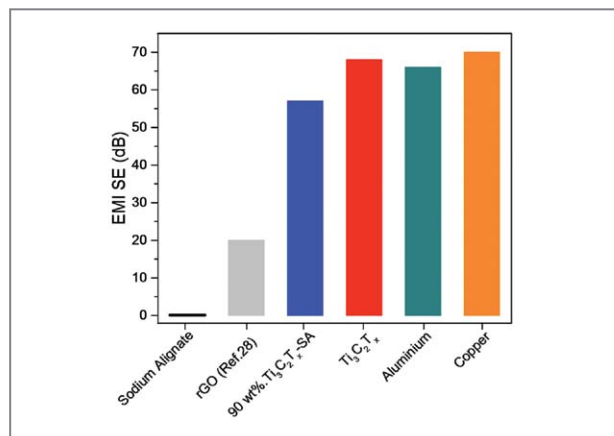


Figure 4 EMI SE values of thin films of sodium alginate (thickness: 9 μm), 90 wt.% $\text{Ti}_3\text{C}_2\text{T}_x$ -SA (8 μm), $\text{Ti}_3\text{C}_2\text{T}_x$ (11.2 μm), aluminum (8 μm) and copper (10 μm) in X-band range. For comparison, a previously reported value for rGO film (8.4 μm thick) is shown [28].

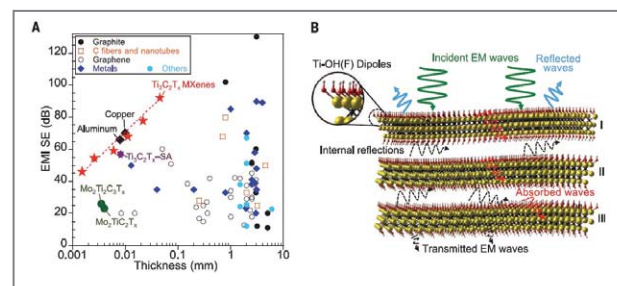


Figure 5 (A) EMI SE vs thickness of different materials. Each symbol indicates a set of material category as: $\text{Ti}_3\text{C}_2\text{T}_x$ MXenes (red solid star), $\text{Ti}_3\text{C}_2\text{T}_x$ -SA composite (purple solid star), molybdenum MXenes (green solid circle), copper and aluminum foils (black solid diamond), metals (blue solid diamond), graphene (open circle), carbon fibers and nanotubes (open square), graphite (black solid circle), other materials (blue solid circle). (B) Proposed EMI shielding mechanism.

a SSE/t of 30830 ($\text{dB cm}^2 \text{g}^{-1}$), which is several times higher than the SSE/t of other materials studied thus far [27, 32]. This finding is significant since several requirements for a commercial EMI shielding product are satisfied in a single material, such as high EMI SE (57 dB), low density (2.31 g cm^{-3}), narrow thickness (8 μm , reducing net weight and volume), oxidation resistance (due to polymer binder), high flexibility (feature of 2D films) and simple processing (mixing and filtration or spray-coating).

EMI shielding mechanism in MXenes

The excellent EMI SE performance of MXene can be understood from several proposed mechanisms shown in Figure 5B. The EMI shielding primarily originates from the excellent electrical conductivity of MXene and partially from the layered architecture of the films. A potential mechanism can be explained as follows. As EMWs strike the surface of a MXene flake, some EM waves are immediately reflected from the surface due to abundant free electrons at the surface of the highly conductive MXene [9, 10]. The remaining waves pass through the MXene lattice structure where interaction with the high electron density of MXene induces currents that contribute to ohmic losses, resulting in a drop in energy of the EMWs. The surviving EMWs, after passing through the first layer of $\text{Ti}_3\text{C}_2\text{T}_x$ marked

as “I” in Figure 5B, encounter the next barrier layer marked as “II” and the phenomenon of EMW attenuation repeats. Simultaneously, layer “II” acts as a reflecting surface and gives rise to multiple internal reflections. The EMWs thus reflect back and forth between the layers (I, II, III and so on) until completely absorbed in the structure. This is a distinct difference compared to pure metals that have a regular crystallographic structure and no interlayer reflecting surface available to provide the internal multiple reflection phenomenon. Thus, the nacre-like (or laminated) structure provides MXene with the advantage of behaving as a multilevel shield. The SEM image shown in Figure 2C shows well-aligned MXene layers in both pure $\text{Ti}_3\text{C}_2\text{T}_x$ and its composites. Considering a μm thick $\text{Ti}_3\text{C}_2\text{T}_x$ film, thousands of 2D $\text{Ti}_3\text{C}_2\text{T}_x$ sheets (a single $\text{Ti}_3\text{C}_2\text{T}_x$ sheet is almost 1 nm thick) act as barriers to EMWs. However, as the overall EMI value goes above 15 dB (>90 % shielding), it is generally assumed that the contribution from internal reflections is minimal [1]. Nevertheless, in layered kinds of structures such as MXenes, multiple internal reflections cannot be fully ignored. The multiple reflection effect, however, is included with absorption since the re-reflected waves get absorbed or dissipated in the form of heat within the shielding material [8, 9, 27]. Furthermore, MXene flake surface terminations may play a role as well. Local dipoles between Ti and terminating groups such as $-\text{F}$, $=\text{O}$ or $-\text{OH}$ (these terminating groups arise during the synthesis process) may be created when subjected to an alternating electromagnetic field. The ability of each element to interact with incoming EMWs leads to polarization losses, which in turn, improve the overall shielding.

Conclusion

In summary, flexible $\text{Ti}_3\text{C}_2\text{T}_x$ films with thicknesses ranging from 1 to 45 μm exhibit excellent electrical conductivity and EMI shielding capabilities. Their reported EMI SE values are the highest of any known

synthetic materials with similar thicknesses. Moreover, excellent shielding ability is maintained after adding sodium alginate to create polymer composite films with varying filler content. This allows the use of very thin films for device shielding to help eliminate EM radiation, a critical factor in an era of electronic miniaturization. A 45-micrometer-thick $\text{Ti}_3\text{C}_2\text{T}_x$ film exhibited EMI shielding effectiveness of 92 decibels (>50 decibels for a 2.5-micrometer film). This performance is attributable to the excellent electrical conductivity of $\text{Ti}_3\text{C}_2\text{T}_x$ films (4600 Siemens per centimeter) and multiple internal reflections from $\text{Ti}_3\text{C}_2\text{T}_x$ flakes in free-standing films. This study introduces a large family of 2D materials that are far superior in performance compared to currently used materials in EMI shielding applications.

Note

This article and images are drawn from our manuscript “Electromagnetic Interference Shielding with 2D Transition Metal Carbides (MXenes)” in *Science*, Vol. 353 (6304), pp. 1137-1140.

References

- [1] Chen Z, Xu C, Ma C, Ren W, Cheng HM. *Advanced Materials* 2013; 25: 1296-1300.
- [2] Yan DX et al. *Advanced Functional Materials* 2015; 25: 559-566.
- [3] Yousefi N et al. *Adv. Mater.* 2014; 26: 5480-5487.
- [4] Zhang Y et al. *Adv. Mater.* 2015; 27: 2049-2053.
- [5] Frey AH. *Environmental Health Perspectives* 1998; 106: 101.
- [6] Chung DDL. *Carbon* 2001; 39: 279-285.
- [7] Das NC et al. *Polymer Engineering & Science* 2009; 49: 1627-1634.
- [8] Al-Saleh MH, Saadeh WH, Sundararaj U. *Carbon* 2013; 60: 146-156.

- [9] Zhang HB, Yan Q, Zheng WG, He ZX, Yu ZZ. *ACS Applied Materials & Interfaces* 2011; 3: 918-924.
- [10] Thomassin JM et al. *Materials Science and Engineering: R: Reports* 2013; 74: 211-232.
- [11] Cao MS, Wang XX, Cao WQ, Yuan J. *Journal of Materials Chemistry C* 2015; 3: 6589-6599.
- [12] Naguib M, Mochalin VN, Barsoum MW, Gogotsi Y. *Adv. Mater.* 2014; 26: 992-1005.
- [13] Lukatskaya MR et al. *Science* 2013; 341: 1502-1505.
- [14] Anasori B et al. *ACS Nano* 2015; 9: 9507-9516.
- [15] Halim J et al. *Advanced Functional Materials* 2016; 26: 3118-3127.
- [16] Ling Z et al. *Proceedings of the National Academy of Sciences* 2014; 111: 16676-16681.
- [17] Boota M et al. *Adv. Mater.* 2016; 28: 1517-1522.
- [18] Kovalenko I et al. *Science* 2011; 334: 75-79.
- [19] Anasori B et al. *Nanoscale Horizons* 2016; 1: 227-234.
- [20] Khazaei M et al. *Advanced Functional Materials* 2013; 23: 2185-2192.
- [21] J. J. Liang et al. *Carbon* 2009; 47: 922-925.
- [22] Shahzad F, Kumar P, Kim YH, Hong SM, Koo CM. *ACS Appl. Mater. Inter.* 2016; 8: 9361-9369.
- [23] Zeng Z et al. *Carbon* 2016; 96: 768-777.
- [24] Varshney S, Ohlan A, Jain VK, Dutta VP, Dhawan SK. *Industrial & Engineering Chemistry Research* 2014; 53: 14282-14290.
- [25] Xu P et al. *The Journal of Physical Chemistry B* 2008; 112: 2775-2781.
- [26] Liu L et al. *Journal of Magnetism and Magnetic Materials* 2012; 324: 1786-1790.
- [27] Ameli A, Nofar M, Wang S, Park CB. *ACS Applied Materials & Interfaces* 2014; 6: 11091-11100.
- [28] Shen B, Zhai W, Zheng W. *Advanced Functional Materials* 2014; 24: 4542-4548.
- [29] Shen B, Li Y, Zhai W, Zheng W. *ACS Appl. Mater. Inter.* 2016; 8: 8050-8057.
- [30] Yang Y, Gupta MC, Dudley KL, Lawrence RW. *Nano Letters* 2005; 5: 2131-2134.
- [31] Chen Y et al. *Advanced Functional Materials* 2016; 26: 447-455.
- [32] Zeng Z et al. *Advanced Functional Materials* 2016; 26: 303-310.



Feature Articles

A Disordered Array of Plasmonic Metal Nanoparticles for Strong Upconversion Luminescence and a Highly-Sensitive Near-Infrared Photodetector



Seok Joon KWON

Nanophotonics
Research Center,
Materials and Life
Science Research
Division
cheme@kist.re.kr

Introduction

Utilizing broad-band light in a single device has been an important technology in a variety of photonic systems in recent years [1-3]. These efforts have mainly focused on maximizing incident light absorption; however, strategies for utilizing broad-band light becomes complicated when light extraction from devices is pursued. Enhancing both the incident light absorption and internally-generated light emission, such as upconversion luminescence (UCL), requires optimized configurations within an optimization strategy [4-8]. In particular, a configuration to overcome the low internal quantum efficiency (IQE) of the UCL for practical applications is in strong demand. Recently, nano-patterns have been examined to enhance light absorption [4-8] or extraction [4-6]. Instead of a single uniform pattern, sophisticated nano-patterns can be employed; however, these typically require cost-intensive fabrications. In contrast, employing an array of randomized metallic nanoparticles (NPs) can be a plausible way to enhance light absorption or extraction. In the present study, we suggest a simple yet coherent approach of harnessing conspicuously enhanced UCL from the NIR-to-visible upconversion nanoparticles (UCNP) by utilizing a disordered array of plasmonic metal NPs (DANPs) on the dielectric layer supported by a metallic back reflector. The designed platform shows outstanding optical and photonic performance compared to counterpart ordered platforms (OANPs). We could verify that the suggested method provides a sound method of harnessing ultra-strong UCL enhanced by 3 orders of magnitude

compared to a reference platform. Consequently, the ultra-strong UCL led to the construction of a highly-sensitive, fast, and stable NIR photodetector sensing weak NIR at room temperature without cooling.

Discussion

The design of our plasmonic platform (hereafter coded MIUIM) started with the deposition of 100 nm-thick Ag film (M) on a Si substrate. A thin insulator layer composed of a 2D monolayer of lanthanide ($\text{Yb}^{3+}/\text{Er}^{3+}$)-doped $\beta\text{-NaYF}_4$ UCNP (U) [9], which were sandwiched between 5 nm-thick bottom (I) and top SiO_2 (I) layers, was placed onto the deposited film. Next, 15 nm-thick Ag film (M) was deposited on the top SiO_2 surface followed by thermal annealing. The platform is described in **Figure 1A** with a representative ultra-strong UCL image observed from the platform in **Figure 1B**. In the DANPs, neither orientational order nor a spatially regular pattern was observed. However, spatial order existed for the array. To verify the superior optical performances of the fabricated device, we measured the absorbance (Abs) and reflectance (R) spectra of the platform and compared them to those in other platforms such as a UCNP monolayer on glass substrate (Ref), structures composed of insulator-UCNPs monolayer-insulator on glass (IUI), IUI on the Ag back reflector (IUIIM), and IUI with the top DANPs (MIUI). As shown in **Figure 2A**, the MIUIM platform was more effective in broad-band absorption compared to other platforms. In particular, at the excitation NIR ($\lambda_0 = 972$ nm) for UCL, the MIUIM platform exhibited 10.2-times and 3.4-times stronger absorption than the Ref and IUIIM platforms, respectively. The enhanced Abs of the MIUIM platform strongly indicates that DANPs act as a plasmonic configuration to effectively confine the incident NIR. Indeed, the MIUIM platform with DANPs exhibited considerably reduced R spectra in the Vis-NIR range (**Figure 2B**). In particular, the platform exhibited reduced R compared to the IUIIM platform at λ_0 . DDA calculations also indicated that the DANPs provide the AR effects in the Vis-NIR

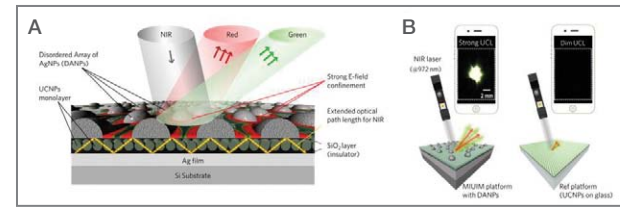


Figure 1 Plasmonic platform with a disordered array of AgNPs (DANPs).

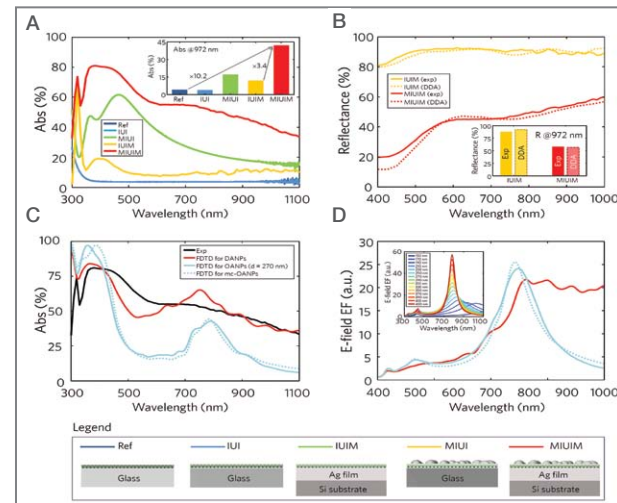


Figure 2 Optical properties of plasmonic platform.

range including λ_0 when compared to the IUIIM platform (**Figure 2B**).

Using the simulated Abs spectra, we calculated mode-collective Abs ($\text{Abs}_{\text{mc}}(\lambda)$) and $\text{Abs}(\lambda, \langle q \rangle)$, where $\langle q \rangle = 2\pi/\langle d \rangle$, and compared them to the experimentally measured spectra (**Figure 2C**). Interestingly, $\text{Abs}_{\text{mc}}(\lambda)$ and $\text{Abs}(\lambda, \langle q \rangle)$ were similar; however, both were considerably lower than the experimental spectra. The discrepancy can be considered to work as a synthetic deterministic aperiodic 2D pattern composed of the OANPs. To detect the distinctive character from the DANPs, we also simulated the Abs spectra of the MIUIM platform with DANPs using 3D FDTD. It is worth noting that the simulated spectra exhibited good agreement with the experimental profile, particularly for the NIR band. The E-field enhancement in the DANPs over OANPs can be linked to Anderson localization (AL) of surface plasmons, which would imply that the

disorder in the plasmonic AgNPs can contribute to the formation of “hotter-spots” for incident NIR E-field confinement in the IUI layer than in OANPs. Indeed at λ_0 , we found that Abs for the MIUIM with DANPs is greater than Abs_{mc} or $\text{Abs}(\langle q \rangle)$ for the MIUIM with OANPs. Therefore, enhanced near-field coupling among plasmonic AgNPs given by the randomized array nature is responsible for the enhanced incident NIR absorption. To investigate the detailed plasmonic enhancement in the UCNP monolayer in the MIUIM platform with DANPs compared to that with OANPs, we conducted full-scale 3D FDTD simulation with incident NIR at λ_0 . In particular, it was observed that the E-field around the individual AgNPs uniformly spread over all the dimensions (**Figure 3E**). From the figures, it is clear that the MIUIM acts as a more efficient plasmonic platform to confine the E-field when incorporated with DANPs than with OANPs. As shown in **Figures 4A-4D**, $|E(r)|^2$ in the UCNP monolayer in the MIUIM platform with DANPs is greater than that in the platform with OANPs regardless of zU . The E-field enhancement is also distinctive along the z -direction for DANPs compared to that for OANPs (**Figures 4E and 4F**). Collectively, DANPs provided a 1.39-fold enhanced E-field confinement compared to

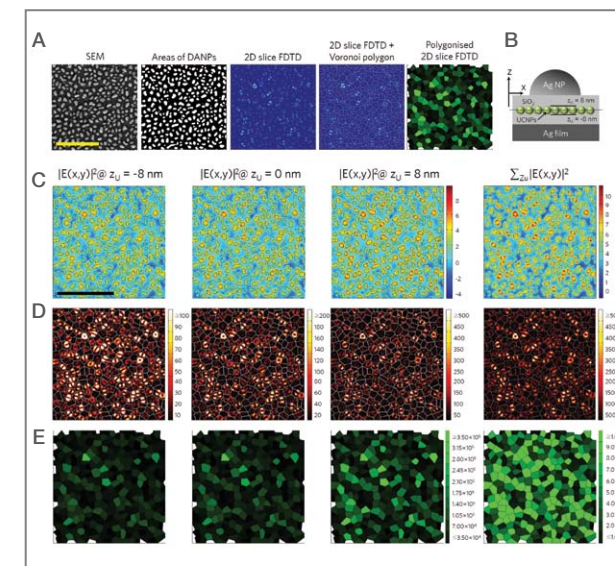


Figure 3 3D distribution of NIR E-field in a MIUIM platform with plasmonic DANPs.

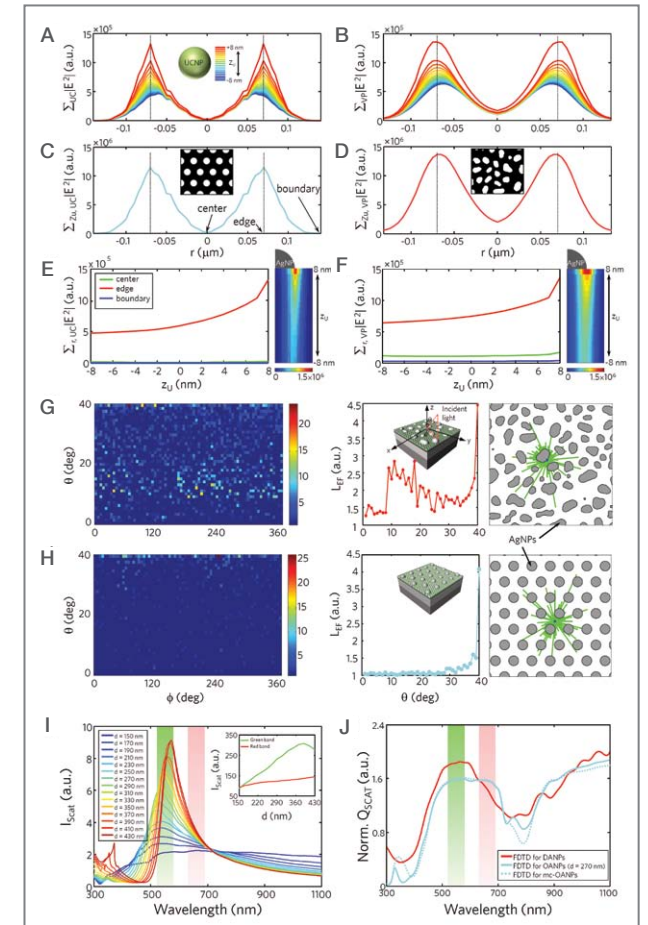


Figure 4 Advantages of DANPs in NIR-trapping and Vis-extracting.

the OANPs in the MIUIM platform. The DANPs also contained absorbed light for a longer period than the OANPs. We investigated the light trapping efficiency of DANPs using 3D Monte-Carlo ray-tracing (3D MCRT) simulation. We found that the DANPs exhibited $21.1 \pm 3.4\%$ additional gain in L_{EF} compared to that in OANPs (**Figures 4G and 4H**). Therefore, the DANPs work better as an incident NIR-trapping frame than do the OANPs. The UCL intensity would be further reinforced with an increase in the forward scattering coefficient of Vis light emitted from UCNP. As shown in **Figures 4I and 4J**, the MIUIM platform with DANPs exhibited higher or comparable scattering for the green and red emissions when compared to the OANPs. Therefore, the DANPs

in the MIUIM platform simultaneously perform as an efficient incident NIR-absorber and Vis-emitter.

The measured UCL intensity from the platform of interest exceeds other platforms by 2-3 orders of magnitude for both green and red emissions (Figures 5A-5C). In addition, the radiative decay rate (Γ_r) is considerably higher than that of the other platforms (Figures 5D and 5E). These data indicate that the internal quantum processes for UCL are boosted more in the MIUIM platform with the DANPs than in the other platforms. The NIR detectability of the MIUIM platform with DANPs was prominently elevated. From the double-logarithmic plots of the PL intensity vs. excitation power shown in Figures 5F and 5G, we observed a linear optical process for PL at strong excitation power, whereas non-linear PL was observed at weak excitation power. The non-linear process, which is due mainly to the intrinsic energy transfer process intervened by the two-photon process [6-8], dominated PL at a weak power limit. In particular, the UCL intensity at the red emission was greatly enhanced, with factor EF = 1.35×10^3 at weak and 1.60×10^2 at strong excitations,

respectively (Figure 5H). For the green emission, EF was slightly reduced, showing EF = 7.62×10^2 and 1.04×10^2 at weak and strong excitations, respectively. It should be noted that for the 3 orders of magnitude, EF is unprecedented in the EFs observed in other experimental studies on UCL. The greatly enhanced UCL is due to the combined effects provided by the boosted internal quantum processes, enhanced NIR-absorption, stronger NIR-trapping, and good nano-antenna effects for higher forward-scattering of Vis light. This is promising for the design of upconversion photonic devices, as the UCNP could replace non-linear optical crystals. To investigate the UCL enhancement mechanism, we employed a rate-equation-based model. The strong UCL enhancement largely depends on the boosted internal processes in the UCNP such as 1) absorption efficiency enhancement (f), 2) faster energy transfer rate between donor and acceptor levels (k_1), 3) increase in Γ_r , and 4) increase in the fraction of the plasmonic resonance-affected UCNP monolayer (ξ) [6-9]. We found that all the processes and factors were noticeably enhanced in the MIUIM platform with DANPs compared to the Ref.

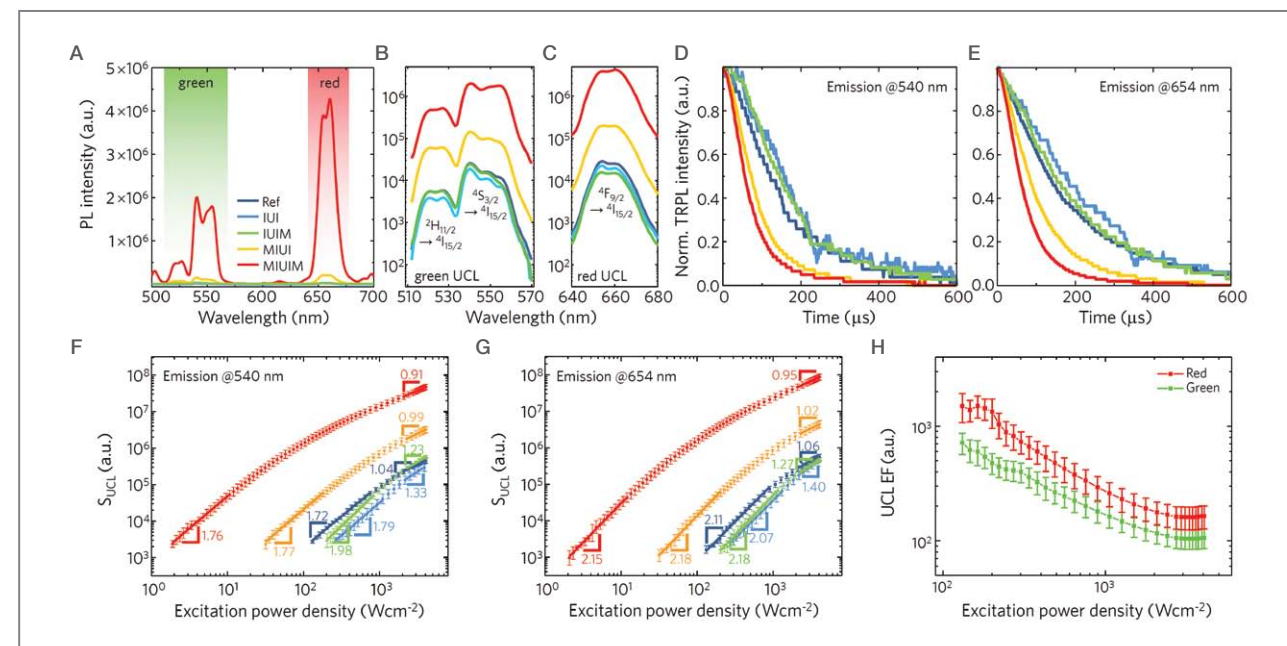


Figure 5 Strongly-enhanced UCL in a MIUIM platform with optimized DANPs.

To take full advantage of the ultra-strong UCL, we fabricated a NIR photodetector composed of a 100 nm-thick PTB7-coated MIUIM platform with DANPs (Figures 6A and 6B). To test the photo-detecting performance of the designed platform, we measured on/off I-V characteristics for NIR at room temperature without cooling. The fabricated photodetectors exhibited a nearly 2-order signal-to-noise ratio at NIR. In addition, the responsibility also exceeded the values of other UCL-based detectors by 1-2 orders of magnitude when normalized by the thickness of the sensing materials. The on/off ratio in the PTB7-coated MIUIM platform with DANPs was 58-times greater than that in the IUIIM platform at a saturated voltage level (Figure 6C). As excitation power diminished, the on/off ratio also monotonically decreased, and was nearly equivalent to that of the IUIIM platform at NIR. The greatly enhanced NIR-detecting performance based on this ultra-strong UCL looks promising for more fruitful applications such as NIR imaging systems and cost-effective NIR-to-Vis spectral converting displays.

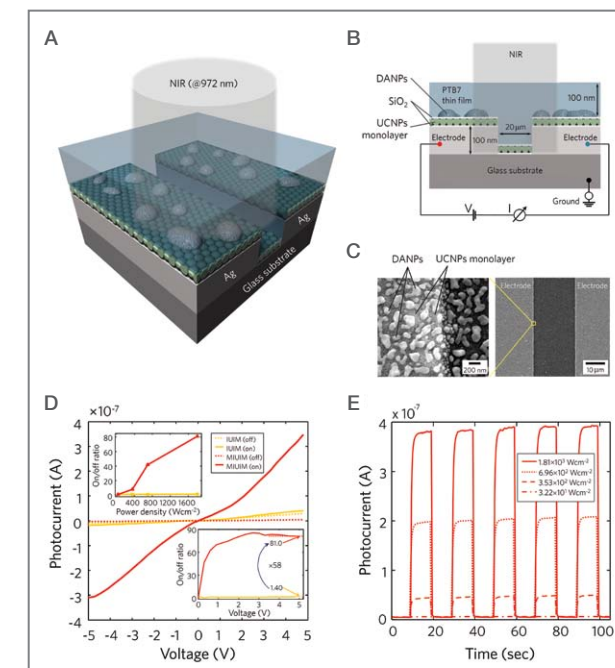


Figure 6 Highly-sensitive NIR photodetector based on ultra-strong UCL.

References

- [1] Schuller JA, Barnard ES, Cai W, Jun YC, White JS, Brongersma ML. *Nat. Mater.* 2010; 9: 193.
- [2] Pala RA, Liu JSQ, Barnard ES, Askarov D, Garnett EC, Fan S, Brongersma ML. *Nat. Commun.* 2013; 4: 2095.
- [3] Forestiere C, Donelli M, Walsh GF, Zeni E, Miano G, Dal Negro L. *Opt. Lett.* 2010; 35: 133.
- [4] Lindquist NC, Nagpal P, Lesuffleur A, Norris DJ, Oh SH. *Nano Lett.* 2010; 10: 1369.
- [5] Zhang W, Ding F, Chou SY. *Adv. Opt. Mater.* 2012; 24: OP236.
- [6] Lu D, Cho SK, Ahn S, Brun L, Summers CJ, Park W. *ACS Nano* 2014; 8: 7780.
- [7] Sun QC, Mundoor H, Ribot JC, Singh V, Smalyukh II, Nagpal P. *Nano Lett.* 2014; 14: 101.
- [8] Lee GY, Jung K, Jang HS, Kyhm J, Han IK, Park B, Ju H, Kwon SJ, Ko H. *Nanoscale* 2016; 8: 2071.
- [9] Na H, Woo K, Lim K, Jang HS. *Nanoscale* 2013; 5: 4242.

An Alternative Patterning Process for the Realization of Large-Area, Full-Color, Active Quantum Dot Displays



Joon Suh PARK

Nanophotonics
Research Center
Materials and Life
Science Research
Division
fieryice@kist.re.kr



Il Ki HAN

Nanophotonics
Research Center
Materials and Life
Science Research
Division
hikoel@kist.re.kr

Introduction

Colloidal quantum dots (QDs) are semiconductor nanocrystals that exhibit quantum confinement effect-derived band-gap tunability and narrow-band photoluminescence characteristics [1]. They have been a source of keen interest for many researchers over the last decade. Due to their color tunability throughout the optical spectrum, they have been considered a promising material for next-generation optoelectronics, especially in the display industry. Moreover, QDs exhibit a similar photo/chemical robustness to their host material due to having a radius smaller than the exciton Bohr radius of the material's bulk state [2]. Such material properties are considered an advantage compared to contemporary organic materials, whose tolerance against oxidation is low and energy state modification is only achievable by manipulating complex chemical structures that result in relatively broad-band emission properties.

To integrate QDs into optical or electrical devices, one requires a technique to coat and pattern the QDs on the desired surface. Unlike organic material devices which can be fabricated by a vacuum-based evaporation method, QDs have a very high molecular weight which precludes the easy application of this same fabrication technique. The dispersal of QDs in a solvent also hinders such a straightforward approach. Various material coating techniques, such as spin-coating [3], self-assembly [4], or dip-coating [5], have been investigated to overcome the obstacles in fabricating QD-based devices. However, such methods only allow for the deposition of

monochrome or mixed QDs onto an entire substrate so that patterning of different QDs is not feasible. Therefore, additional techniques (e.g., mist deposition with fine-metal-mask [6], jet-printing [7], or transfer printing [8]) for patterning QDs have been developed. However, each of these demonstrated methods has limitations or involves trade-offs, such as size-scalability, cost/time effectiveness in manufacturing, mass production, or high-resolution pattern formation, that impede the marketability of QD-based devices.

An alternative approach to resolve these issues, especially as regards the scale and the resolution of QD patterns as well as technical difficulties, would be to use a conventional photolithography process. This method is commonly used for fabricating large-area devices with structural resolution up to the optical diffraction limit. However, because most QDs are dispersed in organic, non-polar solvents, solvent non-orthogonality with materials used in photolithography prohibits the use of such a process with colloidal QDs; the solvents dissolve both the QDs and photoresist so they cannot be used simultaneously. Therefore, using water-dispersed QDs which are orthogonal to the non-polar solvents used in photolithography could allow for the application of the photolithography process to pattern the QDs.

In this work, we present an alternative QD patterning method that combines a photolithographic lift-off process and charge-assisted layer-by-layer (LbL) assembly [9] of hydrophilic QDs. In addition to showing that the fine-patterning of QDs can be achieved by photolithography, we also demonstrate that such a patterning process can be integrated into an actual working device.

Photolithographic quantum dot patterning

After performing conventional photolithography to form a photoresist pattern on a substrate (Figure 1A (1)-(2)), LbL assembly of QDs is performed. First, the surface is exposed to oxygen plasma to endow a negative charge on the surface of the substrate (Figure 1A (3)).

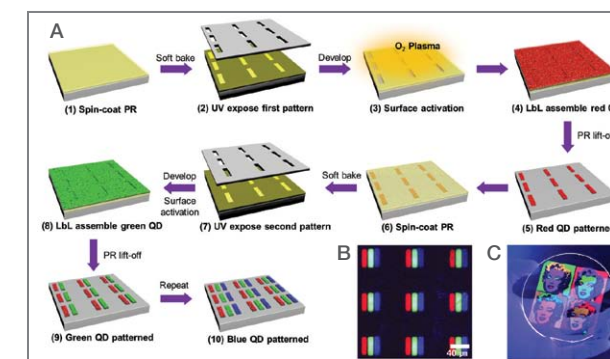


Figure 1 Illustration of photolithographic QD patterning process. (b) PL image of micro-scale patterned RGB quantum dot array. (c) Large-scale QD pattern demonstration with pop art of Marilyn Monroe by Andy Warhol (1967) on 4-inch quartz wafer under UV lamp excitation.

The substrate, now hydrophilic by “surface activation,” is then immersed in positively ionized polyelectrolyte solution in water. The positively charged polyelectrolyte adheres to the negatively charged surface by electrostatic force. After the immersion process, the substrate is rinsed thoroughly in water to remove residual polyelectrolytes that are not bonded to the substrate and is dried with a nitrogen gun. The surface-adhered polyelectrolyte temporarily provides a positively charged surface.

Then the substrate is coated with water-dispersed QDs that have surface termination which negatively ionizes in water. The negatively ionized ligands of the QDs bond electrically to the polyelectrolyte-covered substrate. After the QD deposition process, the substrate is rinsed with water to remove excess QDs that are not strongly bonded to the polyelectrolyte layer and is dried with a nitrogen gun. This results in an assembly of QD monolayer on the entire exposed surface. By repeating the process of immersing in polyelectrolyte solution and depositing QDs, one can achieve thicker QD layers with respect to the number of LbL cycles.

When the desired thickness of QD pattern is achieved (Figure 1A (4)), the PR-patterned and QD-deposited substrate is sequentially immersed in acetone and methanol in an ultrasonic bath to lift-off the PR, carrying along the QD layers coated atop the PR. This results in the first QD pattern on the substrate, as shown in Figure 1A (5). The PR patterning, surface activation,

QD LbL assembly, and lift-off process can be repeated to additionally pattern other QDs on the same substrate (Figures 1A (6)-(11)). Our result in Figure 1B shows the PL image of $40\mu\text{m} \times 40\mu\text{m}$ square RGB pixels on SiO_2 substrate consisting of $10\mu\text{m} \times 40\mu\text{m}$ RGB subpixels with spacing between each color under UV excitation. Also, to provide clear examples of large-scale patterning with this method, we have fabricated differently colored pop art of “Marilyn Monroe 1967” by Andy Warhol on a 4-inch quartz wafer, as shown in Figure 1C.

Reliability study of our proposed method

The resolution demonstration of our method was carried out by patterning line patterns of QDs and observing the process step-by-step with a scanning electron microscope (SEM). As shown in Figure 2A, the PR patterning process results in a tapered PR pattern. After the PR-patterned substrate was exposed to oxygen plasma for surface activation, we found that the plasma minimally etched the PR, retaining the pattern shape (Figure 2B). As the oxygen plasma not only activates the exposed part of the substrate but also the PR itself, the LbL assembly of QDs occurs on both materials so that QDs cover the entire exposed area (Figure 2C). Figure 2D shows the final line pattern of QDs after the PR lift-off process, showing well-defined boundaries. From this result, we are able to conclude that the resolution of QD patterning is only restricted to the optical limit of the photolithography process.

In addition to addressing the resolution issue, we have shown that each QD patterning process does not affect previous patterning despite repeated spin-coating, baking, and stripping PR on top of the patterned QD structure. After reenacting the conditions of repeated photolithography, we were able to observe through atomic force microscopy (AFM) that previously deposited QD layers do not deteriorate by additional pattern processing, as shown in Figures 3A and 3B. Combining this result with thickness control achieved by

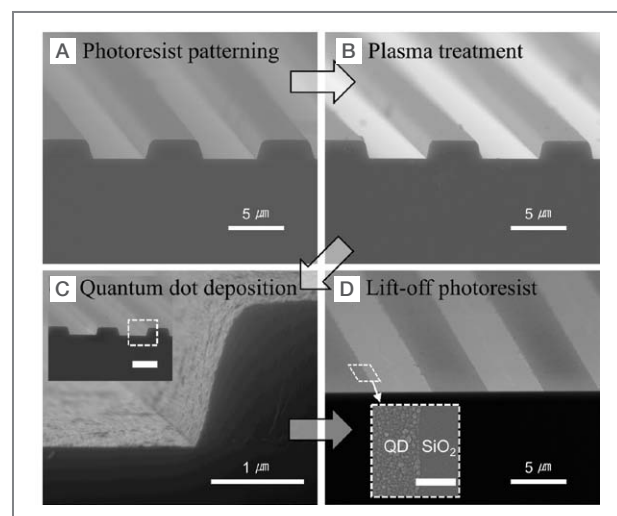


Figure 2 SEM image of QD patterning process on SiO_2 substrate. (A) Line pattern of PR with width and pitch of 5 and 10 μm , respectively. (B) PR-patterned surface after oxygen plasma treatment. Damage to the PR structure is negligible in this scale. (C) Close-up image of the patterned substrate after QD LbL deposition. (D) Line pattern of QDs after PR lift-off process.

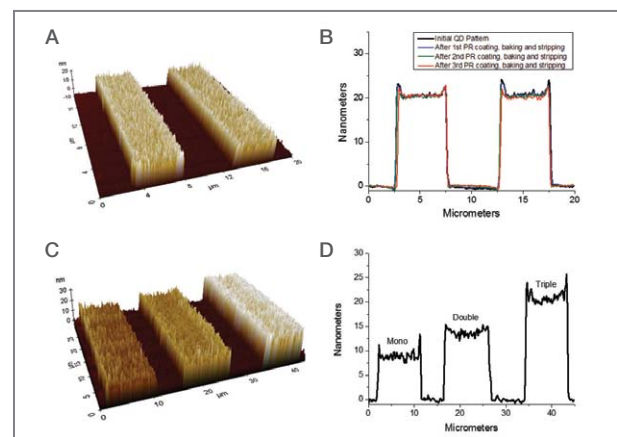


Figure 3 Demonstration of (A) robustness of QD thickness after repeated photolithography processing and (C) layer thickness control at each position. Confirmation by AFM measurements of (B) robustness after processing and (D) thickness control.

repeated LbL assembly, we were also able to demonstrate that QD thickness control for each patterned location can be achieved for future device applications that may require a different thickness for each QD pattern (Figures 3C and 3D).

Application to electroluminescent device

Using the demonstrated method, we fabricated an inverted [10], multicolored, active QD light-emitting device (QD-LED) on a substrate as a proof-of-concept for realizing full-color, active QD displays. The device structure we fabricated was as follows: ITO as the cathode, sol-gel processed ZnO layer as the electron transport layer (ETL), patterned QD as the emissive layer (EML), poly[N,N'-bis(4-butylphenyl)-N,N'-bis(phenyl)-benzidine] (poly-TPD) as the hole injection layer (HIL), and MoO_3/Ag as the anode (Figure 4A).

QDs with varying colors were patterned on each of the four ZnO-coated ITO pixel patterns using photolithographic patterning and LbL assembly. For each pixel, the LbL assembly process was repeated five times to ensure formation of EML, and warm-white color pixel was fabricated by sequentially stacking different QDs (2 cyan, 2 green, and 1 red) with LbL assembly.

Figure 4B shows a cross-sectional transmission electron microscope (TEM) image of the resulting device. The well-defined boundaries between each constituting layer allow effective carrier interaction between each layer without short-circuiting when bias voltage is applied to the device. From an energy band study using ultraviolet photoelectron spectroscopy (UPS) and photoluminescence (PL) measurements, we were able to approximate each material's highest occupied molecular orbital (HOMO) and lowest unoccupied molecular orbital (LUMO) energies (Figure 4C). From the band energy alignment relationships, we were able to speculate that the ultrathin ZnO layer works as an efficient ETL but poor hole-blocking material, and poly-TPD works as both an HIL and electron blocking layer.

Figure 4D shows the electroluminescence (EL) photograph of our RGCW, active QD-LED with a common bias voltage of 6 V. From separately measured I-V-L characteristics, we found that the maximum EL intensities of red, green, cyan and warm-white QD-LEDs were $6,900 \text{ cd/m}^2$ at 6.6 V, $23,770 \text{ cd/m}^2$ at 8.4 V, $4,598 \text{ cd/m}^2$ at 7 V, and $10,920 \text{ cd/m}^2$ at 7.6 V,

respectively. Each pixel's EL can be attributed to a direct recombination within a QD layer as there was no excess EL spectrum originating from other device materials and the EL spectrum consisted solely of near-band edge emission of the QDs.

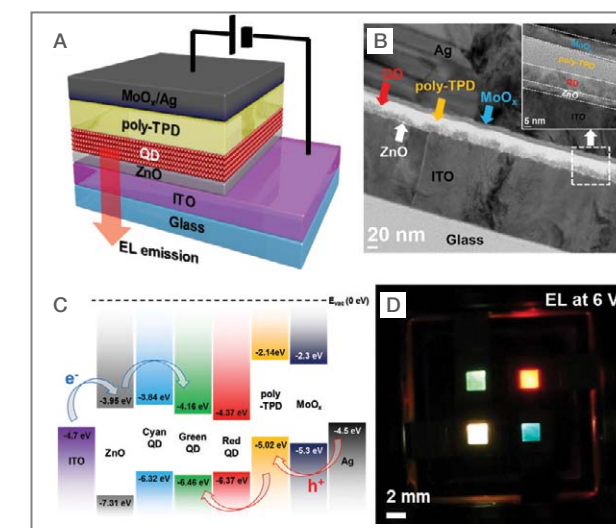


Figure 4 (A) Inverted QD-LED structure. (B) TEM cross-sectional image of our QD-LED structure. (C) Energy diagram of our QD-LED structure. (D) EL image of RGCW QD emissive light-emitting device with different QDs on each pixel.

Conclusion

In the present study, we have successfully shown a novel QD patterning technique using conventional photolithography and provided an alternative to previous studied QD patterning methods. In addition to providing pattern resolution and scalability details, we have shown the reliability of our method against repeated process and thickness control demonstrations to provide a wider scope in practical device fabrication requirements. To provide evident example of this QD patterning process in an actual device application, we made a proof-of-concept, multicolored, active QD-LED on a single substrate. As shown by our example, the presented QD-patterning process can be considered generally expandable to various optoelectronic applications which

require QD patterns for displays or sensors. We believe that this photolithographic QD patterning method can provide a cost-efficient, practical solution to current bottlenecks in developing high-resolution, large-scale QD-based photonic devices, especially in the area of active QD display applications.

Note

This article and images are drawn from “Alternative Patterning Process for Realization of Large-Area, Full-Color, Active Quantum Dot Display” in *Nano Letters*, 2016, Vol. 16, pp. 6946-6953.

References

- [1] Ekimov AI, Efros AL, Onushchenko AA. *Solid State Commun.* 1985; 56(11): 921–924.
- [2] Kortan AR, Hull R, Opila RL, Bawendi MG, Steigerwald ML, Carroll PJ, Brus LE. *J. Am. Chem. Soc.* 1990 112(4): 1327–1332.
- [3] Colvin VL, Schlamp MC, Alivisatos AP. *Nature* 1994; 370(6488): 354–357.
- [4] Gao M, Lesser C, Kirstein S, Möhwald H, Rogach AL, Weller H. *J. Appl. Phys.* 2000; 87(5): 2297–2302.
- [5] Debnath R, Tang J, Barkhouse DA, Wang X, Pattantyus-Abraham AG, Brzozowski L, Levina L, Sargent EH. *J. Am. Chem. Soc.* 2010; 132(17): 5952–5953.
- [6] Pickering S, Kshirsagar A, Ruzyllo J, Xu J. *Opto-Electron. Rev.* 2012; 20(2): 148–152.
- [7] Kim BH, Onses MS, Lim JB, Nam S, Oh N, Kim H, Yu KJ, Lee JW, Kim JH, Kang SK, Lee CH, Lee J, Shin JH, Kim NH, Leal C, Shim M, Rogers JA. *Nano Lett.* 2015; 15(2): 969–973.
- [8] Choi MK, Yang J, Kang K, Kim DC, Choi C, Park C, Kim SJ, Chae SI, Kim TH, Kim JH, Hyeon T, Kim DH. *Nat. Commun.* 2015 6: 7149.
- [9] Bae WK, Kwak J, Lim J, Lee D, Nam MK, Char K, Lee C, Lee S. *Nano Lett.* 2010; 10(7): 2368–2373.

- [10] Kwak J, Bae WK, Lee D, Park I, Lim J, Park M, Cho H, Woo H, Yoon DY, Char K, Lee S, Lee C. *Nano Lett.* 2012; 12(5): 2362–2366.



Technical Review

Improving the Performance and Stability of Flexible Planar-Heterojunction Perovskite Solar Cells Using Polymeric Hole-Transport Material



Hae Jung SON

Photoelectronic Hybrid
Research Center,
National Agenda
Research Division
hjson@kist.re.kr

Introduction

Organic-inorganic hybrid lead halide perovskite solar cells (PSCs) have been recognized as promising candidates in the development of flexible solar cells since it has now been demonstrated that highly crystalline and uniform perovskite films can be formed through simple low-temperature solution processes. Many high-efficiency PSCs have been prepared based on mesoporous-TiO₂-scaffolds, but while these PSCs have shown high power conversion efficiencies (PCEs) of over 21%, the high-temperature processes ($\geq 400^\circ\text{C}$) required to obtain high-quality condensed TiO₂ films have severely limited their use in flexible PSCs [1-7].

In search of alternatives to mesoporous-TiO₂-scaffold-based PSCs, planar heterojunction (PHJ) PSCs have been widely investigated because they enable fabrication of solar cell devices using advantageous mild processing conditions [8-11]. Several normal-type flexible devices have recorded high PCEs, i.e., above 15%, because of the development of low-temperature processable electron-transporting layer (ETL) materials such as ZnO, Zn₂SnO₄, and TiOx, which are suitable for the fabrication of flexible PHJ PSCs on plastic substrates [12-15]. In contrast, due to the absence of appropriate hole-transport layer (HTL) materials, the fabrication of most flexible solar cell devices with an inverted-type architecture has usually been attempted using poly(3,4-ethylenedioxythiophene):poly(styrenesulfonate) (PEDOT:PSS) as the HTL; however, the performance of these devices has been disappointing due to their relatively low PCEs, i.e., below 14% [16-

19]. Such low efficiency has mainly been attributed to the following unfavorable properties of PEDOT:PSS affecting solar device performance: (1) the PEDOT:PSS films display relatively poor charge transport; (2) the relatively low work function (WF) of PEDOT:PSS (~5.0 eV), as compared with the valence band of perovskite (~5.3 eV for $\text{CH}_3\text{NH}_3\text{PbI}_3$) leads to a potential energy loss at the interface between perovskite and PEDOT:PSS layers, resulting in lowering of the built-in potential within the solar cell device and (3) the acidity of PEDOT:PSS (pH ~ 1) corrodes the adjacent layers, which include a transparent anode and a perovskite layer, and hence, accelerates device degradation [20-23]. Nonetheless, polymer materials potentially have many advantages as charge transport materials in flexible PHJ PSCs [24-26].

In this study, we introduced a polymeric hole-transport material resulting from the copolymerization of 1,4-bis (4-sulfonato-butoxy) benzene and thiophene moieties (PhNa-1T) and applied this polymer to high-performance inverted PHJ PSCs on a flexible substrate. The developed solar cell device showed a significantly enhanced PCE of 14.7% compared to a corresponding PEDOT:PSS-based device having a PCE of 8.4%. We investigated the reasons for the notable improvement in the photovoltaic properties of the PhNa-1T-based PSCs by performing various experimental analyses. The air stability and mechanical properties of the PhNa-1T-based flexible PSCs were also tested to further assess their potential in the solar cell market.

Synthesis and opto-electrical properties of polymeric hole-transport materials

An inverted-type PHJ PSC was prepared with a polyethylene naphthalate (PEN)/indium tin oxide (ITO)/HTL/perovskite/[6,6]-phenyl-C61-butyril methyl ester (PC_{61}BM)/Ag device structure as shown in Figure 1A. PhNa-1T (chemical structure shown in Figure 1B) was used as the HTL material because it has

advantageous properties for PHJ PSC applications, such as good hole-transport in the out-of-plane direction and a high electrical conductivity of $2.6 \times 10^{-4} \text{ S cm}^{-1}$ due to its intrinsic doping during the dialysis procedure. In addition, PhNa-1T has been shown to have a relatively high WF of 5.2 eV, which is higher than that of PEDOT:PSS (WF = 5.0 eV) (Figure 1C), and hence, more suitable for forming an Ohmic contact with the perovskite active layer [24].

PhNa-1T is highly soluble in water and water/alcohol solutions; therefore, PhNa-1T HTLs can easily be deposited on ITO by using a low-temperature spin-coating process. A water/isopropyl alcohol co-solvent (1:1 v/v) was used for the spin-casting, resulting in a smooth and homogeneous PhNa-1T film on ITO/PEN. Atomic force microscopy (AFM) images of PhNa-1T films (Figure 1D) show an extremely smooth surface with a low root mean square (RMS) roughness below 1 nm, whereas the PEDOT:PSS film coated on the same substrate exhibited a relatively rougher surface with an RMS value of 1.76 nm. The smooth surface of the PhNa-1T film is favorable for forming a good contact between the HTL and perovskite layers. Figure 1E compares changes in the transmission spectra resulting from the deposition of HTLs on ITO/PEN. The PhNa-1T/ITO/PEN films yielded high optical transmittance values of over 80% in the visible range, though the transmittance in the wavelength range below 600 nm was slightly lower than that of the corresponding PEDOT:PSS film due to the absorption by PhNa-1T.

Methylammonium lead iodide ($\text{CH}_3\text{NH}_3\text{PbI}_3$) perovskite layers were prepared by following the one-step deposition method using a Lewis base adduct as reported by the Park group [29], resulting in ~400nm thick perovskite layers on the HTLs. We then performed experiments to test if PhNa-1T would satisfy the basic properties required for device fabrication. We compared UV-vis absorption spectra of the PhNa-1T films before and after washing with a processing solvent, a dimethylformamide (DMF)/dimethyl sulfoxide (DMSO) mixture, and could not find any significant change between them. This indicates that the PhNa-1T film has good resistivity against the processing solvent used.

The contact angle of a DMF/DMSO mixed drop on the PhNa-1T film was below 10° , thus demonstrating high wettability with the processing solvent. Such appropriate physical properties of PhNa-1T during the solution process enable deposition of the perovskite layer without the need for additional modification of the PhNa-1T surface.

On top of this perovskite layer, a 50 nm thick layer of PC_{61}BM was deposited by spin-coating and then overlaid by 120 nm of an Ag cathode deposited through thermal evaporation.

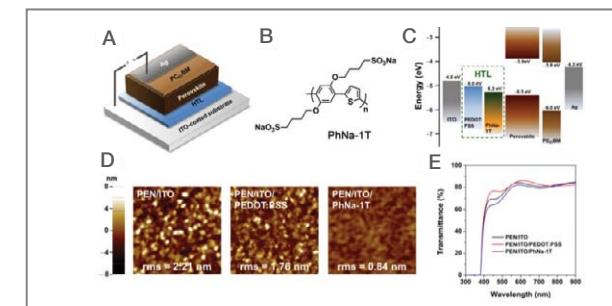


Figure 1 (A) Device architecture of the PHJ PSC. (B) Chemical structure of PhNa-1T. (C) Schematic energy diagrams of the PHJ PSC. (D) Topographic AFM images ($2 \mu\text{m} \times 2 \mu\text{m}$) of PEDOT:PSS and PhNa-1T films deposited on ITO/PEN. (E) Transmission spectra of PEDOT:PSS and PhNa-1T films deposited on ITO/PEN.

Photovoltaic properties of perovskite solar cells using polymeric hole-transport materials

Figure 2A shows the current density-voltage ($J-V$) curves of the flexible PHJ PSCs containing either PEDOT:PSS or PhNa-1T HTLs on ITO/PEN. The photovoltaic parameters determined for these PSCs are summarized in Table 1. The solar cell device incorporating PEDOT:PSS showed a PCE of 8.4%. When PEDOT:PSS was replaced with PhNa-1T, all photovoltaic parameters were remarkably enhanced and the best-performing device achieved a noticeable PCE of 14.7%. External quantum efficiencies (EQEs) of the

solar cell devices were measured under the condition of monochromatic light (Figure 2B). The integrated J_{sc} values calculated from the EQE spectra were 18.2 and 14.1 mA cm^{-2} for the flexible PSCs with PhNa-1T and PEDOT:PSS, respectively. Therefore, the EQE values were consistent with those of J_{sc} obtained from the $J-V$ measurements. Figures 2C and 2D show the $J-V$ curves obtained from the forward and reverse individual scans for the flexible devices. Negligible $J-V$ hysteresis was observed for both the devices. This result was probably due to the good balance between electron and hole fluxes [11, 18]. We also prepared the PHJ PSC device on ITO/glass under the same processing conditions used for the

Table 1 Photovoltaic properties of flexible PSCs^(a) measured under standard AM 1.5G illumination.^(b)

HTL	V_{oc} [V]	J_{sc} [mA cm^{-2}]	FF [%]	PCE [%]
PEDOT:PSS (30 nm)	0.88 (0.88)	14.4 (13.4)	66.2 (63.0)	8.4 (8.0)
PhNa-1T (9 nm)	1.03 (1.01)	18.4 (17.6)	77.4 (73.6)	14.7 (13.3)

(A) Inverted device configuration: PEN/ITO/HTL/ $\text{CH}_3\text{NH}_3\text{PbI}_3$ / PC_{61}BM /Ag.
(B) The values in brackets are the average parameters averaged values calculated from 30 devices.

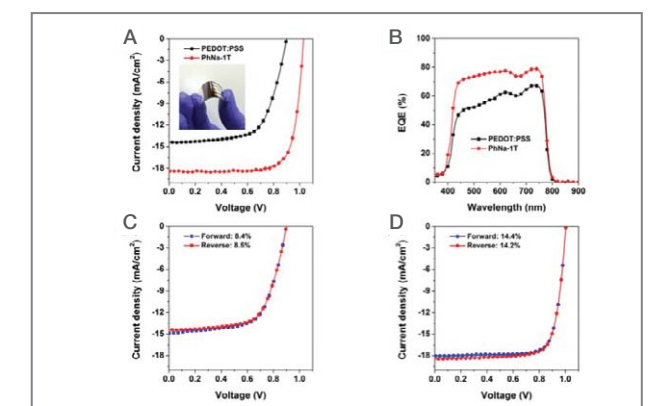


Figure 2 (A) $J-V$ curves and (B) EQE spectra of the flexible PSCs (PEN/ITO/HTL/ $\text{CH}_3\text{NH}_3\text{PbI}_3$ / PC_{61}BM /Ag) with PEDOT:PSS and PhNa-1T HTLs. Inset of (A) is a photograph of the flexible PhNa-1T-based PHJ PSC fabricated in the current work. $J-V$ curves of flexible perovskite solar cells (PEN/ITO/HTL/ $\text{CH}_3\text{NH}_3\text{PbI}_3$ / PC_{61}BM /Ag) using (C) PEDOT:PSS and (D) PhNa-1T HTL under backward and forward scans with a 100 ms time delay.

flexible PSC device. The PhNa-1T PSC consistently showed better photovoltaic properties (PCE of 16.3%) than did the PEDOT:PSS-based PSC, which yielded a PCE of 11.4%. This result further demonstrates the excellent performance of the PhNa-1T-based flexible PSC device.

Effect of polymeric hole-transport materials on open-circuit voltage of perovskite solar cells

Different V_{oc} 's between PSCs using PEDOT:PSS and PhNa-1T HTLs were studied to understand the enhanced performance of the PhNa-1T-based PSCs. In our investigations, the PhNa-1T-based PSCs reproducibly exhibited higher V_{oc} values as compared to PSC devices using PEDOT:PSS, with average values of 1.01V and 0.88V, respectively. The V_{oc} value for PEDOT:PSS-based PSCs is about the same as the -0.9 eV value reported by many other research groups [16-19]. The difference in V_{oc} values between the two types of devices can be explained by a reduced energy loss at the HTL/perovskite interface resulting from the small difference in the energy level between the WFs of PhNa-1T (5.2 eV) and the perovskite valence band (-5.3 eV) (Figure 1C) [17, 22]. Furthermore, as shown in the histogram of V_{oc} values obtained from 30 devices (Figure 3A), PhNa-1T-based PSCs yielded a narrower distribution of V_{oc} values than did the PEDOT:PSS-based PSCs. The methyl ammonium iodide (MAI) precursor presumably induces changes in the properties of PEDOT:PSS located near the PEDOT:PSS/perovskite interface during the perovskite layer processing step.

In order to investigate this hypothesis, we prepared a PEDOT:PSS film that was post-treated with a 1 wt% MAI solution in DMF and then used ultraviolet photoelectron spectroscopy (UPS) and X-ray photoelectron spectroscopy (XPS) to study how this treatment changed the properties of the film. According to the UPS results presented in Figure 3B, it was found that the WF of the PEDOT:PSS film decreased from 5.0 to 4.7 eV with the

MAI deposition. In addition, as shown in Figure 3C, the XPS spectra of the PEDOT:PSS film treated with MAI differed from that of the pristine PEDOT:PSS film as evidenced by the shift of the S 2p peak of PSS from 168.0 eV for untreated film to 168.2 eV after the MAI deposition. This may have induced the vacuum-level shift and decreased WF. It is known that the electrical characteristics of PEDOT:PSS film can be changed by treatment with amine compounds [30-32]. This result suggested that the deposition of the perovskite layer caused the change of the WF of PEDOT:PSS. (Figure 3E), though further studies are necessary. Another factor may be the low reproducibility of the V_{oc} results for PEDOT:PSS-based PSC devices because the degree of influence by MAI on PEDOT:PSS can be different for each deposition. Thus, PEDOT:PSS HTLs in the inverted PSCs may have variable WFs after the deposition of the perovskite layer. In contrast, the properties, including the 5.2 eV WF of the neutral PhNa-1T film, should not be affected significantly by being coated with MAI (Figures 3B and 3D).

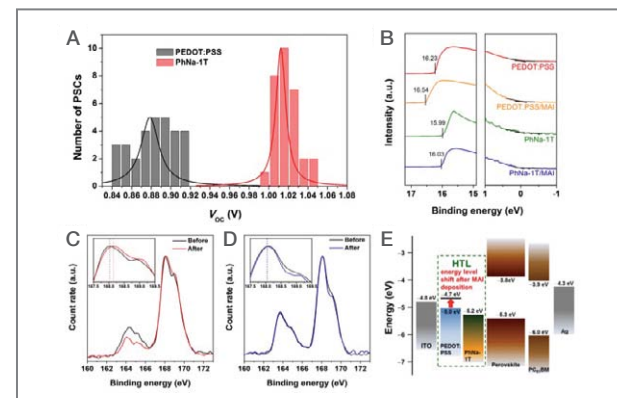


Figure 3 (A) V_{oc} distributions of flexible perovskite solar cells with PEDOT:PSS and PhNa-1T HTL. (B) UPS spectra of HTLs before and after MAI deposition. (C) XPS spectra of (C) PEDOT:PSS and (D) PhNa-1T before and after MAI deposition. (E) Energy level change of PEDOT:PSS after MAI deposition.

Effect of polymeric hole-transport materials on morphology of perovskite photoactive layer

The morphologies of the perovskite films on the PEDOT:PSS and PhNa-1T HTLs were investigated by using X-ray diffraction (XRD) and scanning electron microscopy (SEM). As shown in Figure 4A, the crystalline structures of the perovskite films were compared by XRD analysis. Overall, The PEDOT:PSS- and PhNa-1T-based perovskite films yielded similar diffraction patterns that indicated a tetragonal perovskite structure. However, the PhNa-1T-based perovskite film yielded stronger and sharper XRD peaks, and the (110) peak showed a full width at a half maximum (FWHM) value of 0.48, which was 13% smaller than that of PEDOT:PSS/ $\text{CH}_3\text{NH}_3\text{PbI}_3$ (FWHM = 0.55), suggesting that larger perovskite grains grew on the PhNa-1T layer. The different grain sizes of the perovskite films were clearly shown in the SEM images of their top surfaces. As shown in Figure 4B, the perovskite films on both the PEDOT:PSS and PhNa-1T layers exhibited densely packed morphologies with high surface coverage and film uniformity, but the average grain size of perovskite film on PhNa-1T (~114 nm) was larger than that of the corresponding film on PEDOT:PSS (~65 nm) (Figure 4C). The improved morphology of the perovskite film on PhNa-1T may have contributed to the increases in the J_{sc} and FF of the PhNa-1T-based PSC. These different perovskite growth patterns for the films on PEDOT:PSS and PhNa-1T may have been caused by different surface properties of PEDOT:PSS and PhNa-1T films, perhaps wettability or morphology.

We also tested for differences in the perovskite crystal orientation in film for different interlayer materials [35-36]. When the $\text{CH}_3\text{NH}_3\text{PbI}_3$ films grown on PEDOT:PSS and PhNa-1T were investigated by grazing incidence

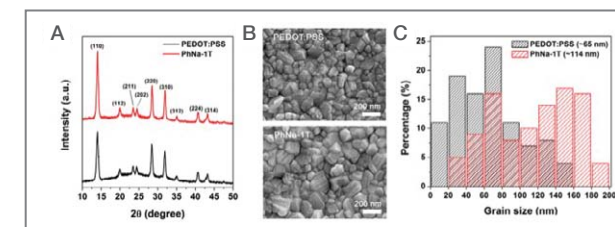


Figure 4 (A) XRD patterns and (B) SEM images of $\text{CH}_3\text{NH}_3\text{PbI}_3$ films processed on PEDOT:PSS and PhNa-1T. (C) Grain size distributions obtained from the SEM images.

X-ray diffraction (GIXD), similar GIXD patterns were observed and there was no meaningful change induced in the crystal orientation for the perovskite films using these different HTLs.

Charge extraction/collection abilities were examined by determining time-resolved photoluminescence (PL) decays of the perovskite films used on PhNa-1T and PEDOT:PSS HTLs. The time-resolved PL decays of the quartz/perovskite, PEDOT:PSS/perovskite, and PhNa-1T/perovskite are shown in Figure 5A. The time-resolved PL profiles were fitted using a bi-exponential function [37-40]. The average PL decay time of the perovskite film on the bare quartz substrate was found to be 12.5 ns, whereas the perovskite films deposited on the PEDOT:PSS and PhNa-1T HTLs yielded much reduced decay times of 6.1 and 1.7 ns, respectively. The lower decay time of the PhNa-1T/perovskite film compared with the PEDOT:PSS/perovskite film indicates more efficient hole extraction at the PhNa-1T/perovskite interface, which may have resulted in reduced charge recombination and thus the improved J_{sc} and FF values.

To enhance scientific understanding of the charge recombination and charge transport manner in the PHJ devices, we performed electrochemical impedance spectroscopy studies in the frequency range of 0.1 Hz to 1.5 MHz under different applied voltages (Figure 6). The individual electronic parameters were estimated by fitting curves with the equivalent circuit for inverted PSC as reported by the Huang group (Figure 6) [41-42]. Short and long lifetimes, which were denoted as the interface recombination lifetime and bulk recombination time respectively, were then extracted. Prolonged recombination time of the bulk component

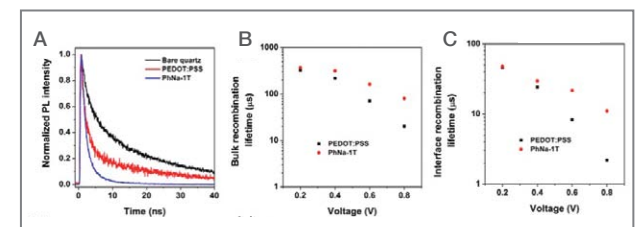


Figure 5 (A) Time-resolved PL decays of $\text{CH}_3\text{NH}_3\text{PbI}_3$ films on bare quartz, and PEDOT:PSS and PhNa-1T films. (B) Bulk and (C) interface recombination times of PHJ PSCs under different applied voltages.

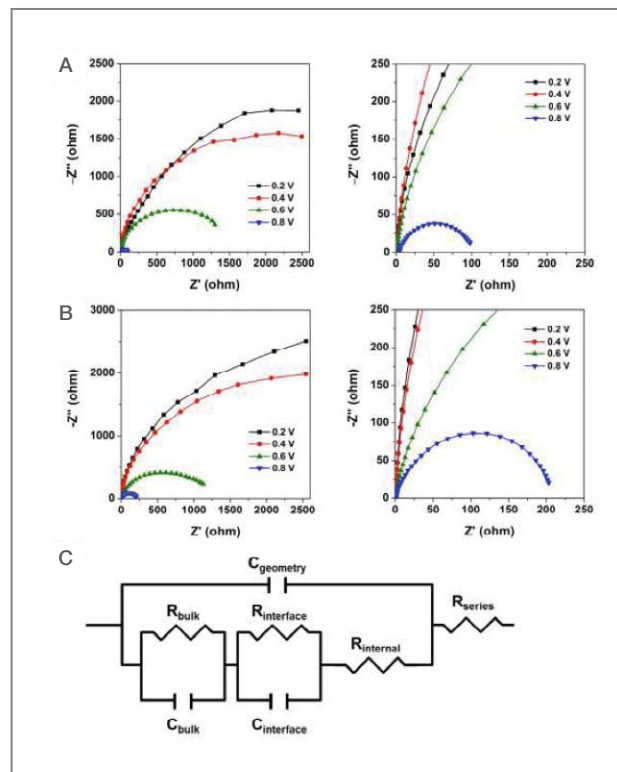


Figure 6 Nyquist plots of perovskite solar cells using (A) PEDOT:PSS and (B) PhNa-1T HTLs under different applied voltages. (C) The equivalent circuits for fitting Nyquist plots.

could be explained by low trap density in the bulk of high crystalline perovskite films [41]. As shown in **Figure 5B**, the PhNa-1T-based PSC exhibited extended bulk recombination lifetimes over the whole voltage range compared with the PEDOT:PSS device. Note that the relatively large perovskite grains of the PhNa-1T-based PSC would be expected to suppress charge recombination due to the reduced grain boundaries (**Figure 4B**) [33-34]. In addition, increased interface recombination lifetimes of the PSCs were found after replacing PEDOT:PSS with PhNa-1T (**Figure 5C**). Such improvements were probably due to the smoother surface of the PhNa-1T film which likely reduced the surface trap density at the HTL/perovskite interface. Also, better hole-transport of PhNa-1T in the out-of-plane direction may have contributed significantly to efficient charge transport. From the impedance spectroscopy study, we concluded that the introduction of PhNa-1T enhanced the

solar cell performance of the PHJ PSC by simultaneously improving the properties of the bulk perovskite and of the HTL/perovskite interface in the PSC device.

Effect of polymeric hole-transport materials on the long-term stability of perovskite solar cells

Long-term stability tests of the flexible PSC devices were conducted under an ambient condition of 25°C and 40% relative humidity. **Figure 7A** shows PCE changes of the PSC devices with different HTLs as a function of exposure time. The PCE of the PEDOT:PSS-based PSC rapidly decreased and approached zero after 168 h whereas the PhNa-1T-based PSC showed a much slower rate of decrease of the PCE, and in fact, maintained more than 66% of its initial performance even after 300 h of exposure. The low stability of the PEDOT:PSS-based device is closely related to degradation of the ITO and perovskite films by the acidic PEDOT:PSS [21, 23]. In contrast, the neutral PhNa-1T HTL (pH = 7.12) would be expected to be much more favorable for maintaining the stability of the flexible PSC device.

Mechanical bending tests were performed with various binding radii (r) in order to evaluate the mechanical properties of PhNa-1T-based flexible PSCs (**Figure 7B**). The bending axis and the electrodes were at right angles to each other while the mechanical stress

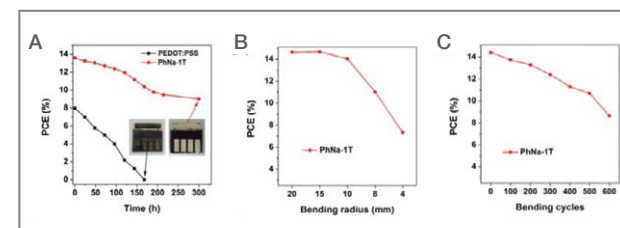


Figure 7 (A) PCE changes of the flexible PHJ PSCs with PEDOT:PSS and PhNa-1T HTLs as a function of exposure time to ambient atmosphere (40% relative humidity at 25°C). The inset shows photographs of the corresponding degraded PHJ PSCs. (B) PCEs of the PhNa-1T-based flexible devices obtained after recovery from bending at various radii ($r = 20-4$ mm). (C) PCEs of the PhNa-1T-based flexible devices after repeated bending at $r = 10$ mm for up to 600 bending cycles.

was applied on the active layers. The performance of the flexible devices was maintained without any significant change for bending radii down to $r = 10$ mm, whereas the FF and PCE values declined when the bending radius was decreased to below 8 mm. In our previous report [18], organic-inorganic hybrid lead halide perovskite was demonstrated to display outstanding mechanical flexibility and was not destroyed for bending radii down to $r = 1$ mm. We used SEM to further investigate the failure of the device during the bending test. As shown in **Figure 8**, cracks were clearly observed after bending at $r = 4$ mm when the samples were prepared on PEN/ITO, while there was no significant evidence of degradation in the corresponding samples coated on a PEN substrate without ITO. This suggests that the relatively limited flexibility of our flexible PSCs is mainly due to cracking of the ITO, which may result not only from increased sheet resistance of ITO but also degradation of the other layers in the device though the propagation of cracks [13, 14]. Repeated bending tests were also conducted to identify the bending durability of the flexible PSCs (**Figure 7C**). The performance of the flexible devices gradually decreased during the 600 bending cycles at

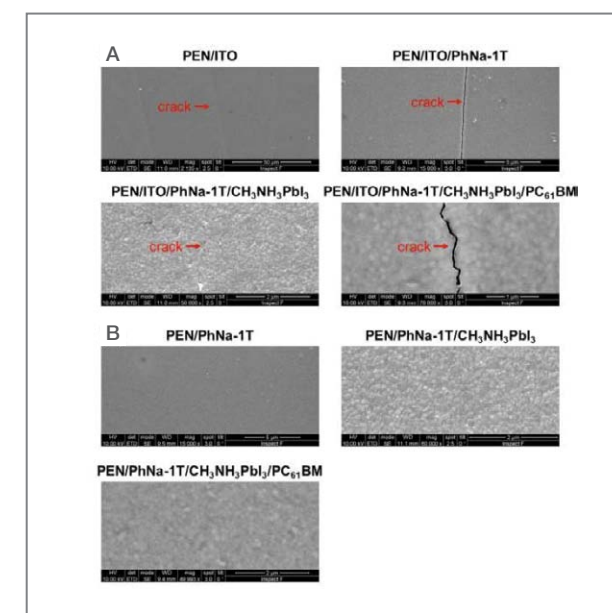


Figure 8 SEM images of samples prepared on (A) PEN/ITO and (B) PEN after bending at $r = 4$ mm.

$r = 10$ mm, and this gradual decrease appears to have been mainly due to a reduction in FF induced by a failure of the ITO electrode. Nevertheless, the PhNa-1T-based flexible device retained a relatively high solar cell performance after 600 bending cycles at 60% of the initial PCE. As a result, our flexible PSC devices using the PhNa-1T interlayer were shown to have a high resistance.

Conclusion

We developed a PhNa-1T HTL in a low-temperature solution process to achieve a high-performance, flexible PHJ PSC in inverted architecture. Introduction of PhNa-1T in place of PEDOT:PSS in the HTLs of PSCs was found to be more effective in reducing potential energy loss at the HTL/perovskite interface, forming a better contact between the perovskite layer and underlying HTL and enhancing the morphology of the $\text{CH}_3\text{NH}_3\text{PbI}_3$ film. These features are due to the enhanced charge extraction from the perovskite absorber to the HTL and the suppression of the charge combination of the bulk perovskite and the HTL/perovskite interface of the PSCs. Consequently, a flexible PHJ PSC based on a PhNa-1T HTL instead of a PEDOT:PSS HTL achieved a much better photovoltaic performance of 14.7%. In addition, the air stability of PhNa-1T-based flexible PSCs was observed to be more stable than with PEDOT:PSS, and mechanical resistance was excellent under repeated stress. In conclusion, we believe that PhNa-1T offers considerable promise as an HTL material for high-performance flexible PHJ PSCs and represents a great opportunity for use in advanced optoelectronics such as deformable portable and wearable devices.

Note

This article and images are drawn from “Improving Performance and Stability of Flexible Planar-Heterojunction Perovskite Solar Cells Using Polymeric

Hole-Transport Material” in *Adv. Funct. Mater.*, Vol. 26, pp. 4464-4471.

References

- [1] Kojima A, Teshima K, Shirai Y, Miyasaka T. *J. Am. Chem. Soc.* 2009 131: 6050.
- [2] Im JH, Lee CR, Lee JW, Park SW, Park NG. *Nanoscale* 2011 3: 4088.
- [3] Burschka J, Pellet N, Moon SJ, Humphry-Baker R, Gao P, Nazeeruddin MK, Grätzel M. *Nature* 2013 499: 316.
- [4] Stranks SD, Eperon GE, Grancini G, Menelaou C, Alcocer MJP, Leijtens T, Herz LM, Petrozza A, Snaith HJ. *Science* 2013 342: 341.
- [5] Zhou H, Chen Q, Li G, Luo S, Song TB, Duan HS, Hong Z, You J, Liu Y, Yang Y. *Science* 2014 345: 542.
- [6] Park S, Heo JH, Cheon CH, Kim H, Im SH, Son HJ. *J. Mater. Chem. A*. 2015 3: 24215.
- [7] Bi D, Tress DW, Dar MI, Gao P, Luo J, Renevier C, Schenk K, Abate A, Giordano F, Baena JPC, Decoppet JD, Zakeeruddin SM, Nazeeruddin MK, Grätzel M, Hagfeldt A. *Sci. Adv.* 2016 2: e1501170.
- [8] Liu M, Johnston MB, Snaith HJ. *Nature* 2013 501: 395.
- [9] Sun S, Salim T, Mathews N, Duchamp M, Boothroyd C, Xing G, Sum TC, Lam YM. *Energy Environ. Sci.* 2014 7: 399.
- [10] Yan W, Li Y, Ye S, Liu Z, Wang S, Bian Z, Huang C. *Nano Energy* 2015 16: 428.
- [11] Xiao Z, Dong Q, Bi C, Shao Y, Yuan Y, Huang J. *Adv. Mater.* 2014 26: 6503.
- [12] Kumar MH, Yantara N, Dharani S, Graetzel M, Mhaisalkar S, Boix PP, Mathews N. *Chem. Commun.* 2013 49: 11089.
- [13] Liu D, Kelly TL. *Nat. Photonics* 2014 8: 133.
- [14] Kim BJ, Kim DH, Lee YY, Shin HW, Han GS, Hong JS, Mahmood K, Ahn TK, Joo YC, K. Hong S, Park NG, Lee S, Jung HS. *Energy Environ. Sci.* 2015 8: 916.
- [15] Yang D, Yang R, Zhang J, Yang Z, Liu S, Li C. *Energy Environ. Sci.* 2015 8: 3208.
- [16] Docampo P, Ball JM, Darwich M, Eperon GE, Snaith HJ. *Nat. Commun.* 2013 4: 2761.
- [17] Lim KG, Kim HB, Jeong J, Kim H, Kim JY, Lee TW. *Adv. Mater.* 2014 26: 6461.
- [18] Park M, Kim HJ, Jeong I, Lee J, Lee H, Son HJ, Kim DE, Ko MJ. *Adv. Energy Mater.* 2015 5: 1501406.
- [19] Li Y, Meng L, Yang YM, Xu G, Hong Z, Chen Q, You J, Li G, Yang Y, Li Y. *Nat. Commun.* 2016 7: 10214.
- [20] Nardes AM, Kemerink M, Janssen RAJ, Bastiaansen JAM, N. Kiggen MM, Langeveld BMW, A. van Breemen JJM, de Kok MM. *Adv. Mater.* 2007 19: 1196.
- [21] Hou F, Su Z, Jin F, Yan X, Wang L, Zhao H, Zhu J, Chu B, Lia W. *Nanoscale* 2015 7: 9427.
- [22] Lin Q, Stoltzfus DM, Armin A, Burn PL, Meredith P. *Adv. Mater. Interfaces* 2015 3: 1500420.
- [23] Hou Y, Zhang H, Chen W, Chen S, Quiroz COR, Azimi H, Osvet A, Matt GJ, Zeira E, Seuring J, Kausch-Busies N, Lövenich W, Brabec CJ. *Adv. Energy Mater.* 2015 5: 1500543.
- [24] Jo JW, Jung JW, Bae S, Ko MJ, Kim H, Jo WH, Jen AKY, Son HJ. *Adv. Mater. Interfaces* 2016 3: 1500703.
- [25] Zhou H, Zhang Y, Mai CK, Collins SD, Nguyen TQ, Bazan GC, Heeger AJ. *Adv. Mater.* 2014 26: 780.
- [26] Lee JH, Lee BH, Jeong SY, Park SB, Kim G, Lee SH, Lee K. *Adv. Energy Mater.* 2015 5: 1501292.
- [27] Choi H, Mai CK, Kim HB, Jeong J, Song S, Bazan GC, Kim JY, Heeger AJ. *Nat. Commun.* 2015 6: 7348.
- [28] Li X, Liu X, Wang X, Zhao L, Jiu T, Fang J. *J. Mater. Chem. A*. 2015 3: 15024.
- [29] Ahn N, Son DY, Jang IH, Kang SM, Choi M, Park NG. *J. Am. Chem. Soc.* 2015 137: 8696.
- [30] Zhou Y, Fuentes-Hernandez C, Shim J, Meyer J, Giordano AJ, Li H, Winget P, Papadopoulos T, Cheun H, Kim J, Fenoll M, Dindar A, Haske W, Najafabadi E, Khan TM, Sojoudi H, Barlow S, Graham S, Brédas JL, Marder SR, Kahn A, Kippelen B. *Science* 2012 336: 327.
- [31] Gu Z, Zuo L, Larsen-Olsen TT, Ye T, Wu G, Krebs FC, Chen H. *J. Mater. Chem. A*. 2015 3: 24254.
- [32] Jung MH, Lee H. *Langmuir* 2008 24: 9825.
- [33] Wang Q, Bi C, Huang J. *Nano Energy* 2015 15: 275.
- [34] Bi C, Wang Q, Shao Y, Yuan Y, Xiao Z, Huang J. *Nat. Commun.* 2015 6: 7747.
- [35] Wu Z, Bai S, Xiang J, Yuan Z, Yang Y, Cui W, Gao X, Liu Z, Jin Y, Sun B. *Nanoscale* 2014 6: 10505.
- [36] Huang W, Huang F, Gann E, Cheng YB, McNeill CR.

Adv. Funct. Mater. 2015 25: 5529.

- [37] Liang PW, Liao CY, Chueh CC, Zuo F, Williams ST, Xin XK, Lin J, Jen AKY. *Adv. Mater.* 2014 26: 3748.
- [38] Chen Q, Zhou H, Song TB, Luo S, Hong Z, Duan HS, Dou L, Liu Y, Yang YY. *Nano Lett.* 2014 14: 4158.
- [39] Pellet N, Gao P, Gregori G, Yang TY, Nazeeruddin MK, Maier J, Grätzel M. *Angew Chem. Int. Ed.* 2014 53: 3151.
- [40] Zuo L, Gu Z, Ye T, Fu W, Wu G, Li H, Chen H. *J. Am. Chem. Soc.* 2015 137: 2674.
- [41] Shao Y, Xiao Z, Bi C, Yuan Y, Huang J. *Nat. Commun.* 2014 5: 5784.
- [42] Bae S, Han SJ, Shin TJ, Jo WH. *J. Mater. Chem. A*. 2015 3: 23964.



Potential Risks of TiO₂ and ZnO Nanoparticles Released from Sunscreens into Outdoor Swimming Pools



Seung Hak LEE

Center for Water
Resource Cycle, Green
City Technology Institute
seunglee@kist.re.kr

Introduction

The many attractive properties of nanoparticles (NPs) have led to their widespread application in diverse commercial products. NPs can now be found in medicines, electronics, cosmetics and even foods [1]. However, with their ever-increasing production and use, it is important to evaluate their potential threat to human health and the natural environment. In fact, several recent studies have pointed out certain biological toxicities traceable to NPs, depending on their concentrations and physicochemical properties in the environment [2,3].

Sunscreens, a widely used consumer product, contain nanoparticles of titanium dioxide (TiO₂) and zinc oxide (ZnO) which effectively block ultraviolet (UV) irradiation [4]. TiO₂ NPs are known to be less toxic in stable conditions compared to Ag or ZnO NPs [5], but their effects may become more harmful when exposed to UV irradiation or strong sunlight [6]. A previous study demonstrated that TiO₂ NPs under UV irradiation might restrain the growth of living organisms (e.g., daphnia and algae) by generating reactive oxygen species (ROS) [7]. Another study reported that about 25% of the sunscreen on a bather's skin might wash into the ocean, and the resulting release of TiO₂ and ZnO NPs may inhibit the proliferation of plankton and cause bleaching of coral reefs [8].

Outdoor swimming pools are areas where sunscreen is intensively used, and because of the contained volume of water, released TiO₂ and ZnO NPs are likely to accumulate. However, no proper estimation of the

NPs' potential risks to swimmers has yet been made. Of particular concern is that the UV treatment process used to clean the circulating water at many pools might increase the negative potential of the released NPs by inducing ROS generation.

In this study, we evaluated the potential risks of sunscreen NPs released into pool water by simulating the fate and transport of NPs in the pool. We estimated the possible NP release from sunscreen-applied skin during water activities, NP removal through a typical water treatment process, and ROS generation by the released NPs under sunlight and UV irradiation. Finally, the potential risk of sunscreen NPs was estimated by calculating the possible ROS concentration in a pool based on the typical operating scenario of an outdoor swimming pool.

Physicochemical properties of metal oxide NPs in sunscreen

Five commercial sunscreens were purchased from different international manufacturers and designated as S.1 to S.5. The sunscreens evaluated in this study have different properties as shown in Table 1. They were divided according to their viscosities into thick cream types (S.1, S.3, and S.4) and thin milk types (S.2 and S.5). The total content of metal oxides was within ± 5% of the values specified by the manufacturers.

Table 1 General properties of sunscreens and physicochemical properties of NPs in the sunscreens.

	Apparent color	Type*	Metal oxide contained*	Metal oxide content*
S.1	White	Cream	Nano ZnO	20.0
S.2	White	Milk	Non-nano ZnO	18.9
S.3	Brown	Cream	TiO ₂ ZnO	10.0 3.0
S.4	White	Cream	TiO ₂ ZnO	2.8 2.0
S.5	White	Milk	TiO ₂	1.0

* manufacturer specifications.

The presence of TiO₂ and ZnO in the nano-sized particle form was observed by Fe-SEM-EDS analysis after removing the organic components in the sunscreens. As shown in Figure 1, the single particles observed in every treated sunscreen are in nanoscale (< 100 nm). Compared with pure metal oxide NPs (Figure 1 (A) and (B)), ZnO NPs in S.1, S.2, S.3 and S.4 (Figure 1 (C), (D), (E) and (F), respectively) are smaller while TiO₂ NPs in S5 (Figure 1 (G)) show larger particle sizes.

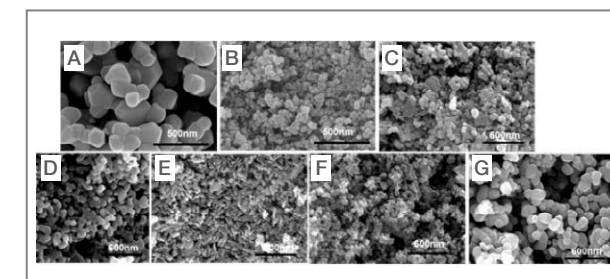


Figure 1 Scanning electron microscopy (SEM) images of (A) pure ZnO NPs and (B) pure TiO₂ NPs. The metal oxide particles found in the evaluated sunscreens are reflected in images (C)-(G): (c) S.1, (D) S.2, (E) S.3, (F) S.4, and (G) S.5.

Release of metal oxide NPs from sunscreen-applied skin

To estimate the amount of NPs released from sunscreen-applied skin during activity in a pool, pieces of pig skin were covered with different sunscreens and stirred in tap water. Releases of metal oxide NPs from the

sunscreen-applied pig skin at different stirring durations is shown in Figure 2. After 120 min of stirring at an initial pH of 7, milk-type sunscreens released roughly 40.0% of their initial amount of NPs into the water ($46.4 \pm 1.2\%$ for S.2 and 40.2 ± 0.8 for S.5), whereas cream types released considerably fewer NPs ($9.8 \pm 0.1\%$ for S.1, $22.3 \pm 1.4\%$ for S.3, and $8.4 \pm 1.0\%$ for S.4). As expected, the NP release increased with the duration of stirring. However, the release pattern was slightly different depending on the sunscreen type. Faster NP release in the case of milk types can be attributed to the weaker binding of the NPs to the skin since the organic components of these sunscreens are less viscous. The milky products are typically made of oil-in-water (o/w) emulsions while cream types are often based on water-in-oil (w/o) emulsions. The o/w emulsion certainly imparts a more hydrophilic character to the sunscreen once it is applied, thus leading to a more pronounced release in water.

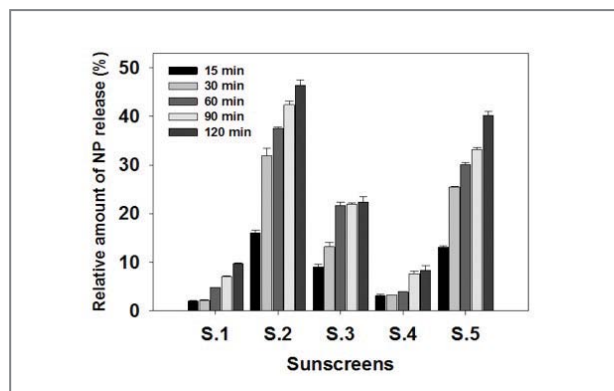


Figure 2 NP release from sunscreen-applied skin into water during different stirring durations at pH 7, normalized to the initial NP content in sunscreen.

Physicochemical properties of metal oxide NPs in sunscreen

As described in the previous section, a significant amount of NPs (10–40% of initial application) can be released from sunscreen-applied skins into pool water during activity. In most cases, pool water is periodically

circulated through a series of treatment processes. To estimate the potential amount of NPs re-entering the pool after treatment, we simulated various common treatment processes, including filtration, UV irradiation, and chlorination. As shown in Figure 3, NP removal by filtration was significant, but varied depending on the pore size of the filter. Additional removal of NPs by subsequent processes of UV irradiation and chlorination was negligible. These results indicate that up to 40% of the NPs from applied sunscreen may be present in the pool water, even after passing through a multi-stage treatment process.

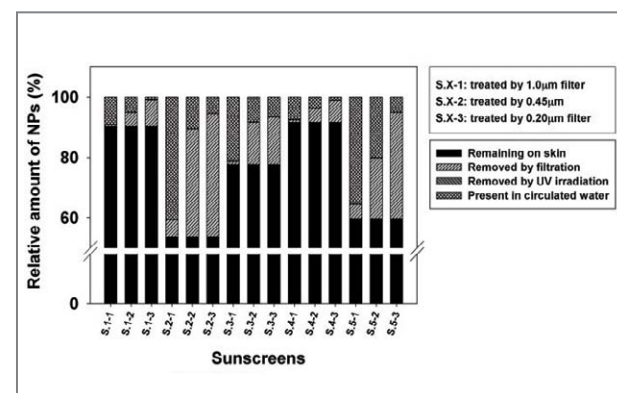


Figure 3 Relative distribution of NPs from sunscreens after water treatment processes.

Generation of ROS in pool water exposed to sunlight and after UV treatment

The potential risk of NPs released into pool water was estimated by measuring the amount of the ROS, hydrogen peroxide (H_2O_2), under simulated sunlight and UV radiation. Experimental results indicated that H_2O_2 generation by the NPs in a sunlit swimming pool is likely to be negligible. Variation of the H_2O_2 concentration in different sunscreen suspensions with time after UV treatment is shown in Figure 4 (A). In general, the concentration decreased with time and showed a

significant drop starting 60 min after the cessation of UV irradiation. Figure 4 (B) demonstrates the relative contributions of sunscreen ingredients (NPs and organics) to H_2O_2 generation. NPs in sunscreens which were treated by burning out the organic components, produced a similar amount of H_2O_2 to that of pure NPs. However, our results indicate that the co-existing organic ingredients in untreated sunscreens may enhance or inhibit the generation of H_2O_2 . Therefore, the overall amount of H_2O_2 generated by a sunscreen may vary depending on its composition, for example, levels of TiO_2 or ZnO NPs, the type of organic components within the formula, and the presence of inorganic impurities.

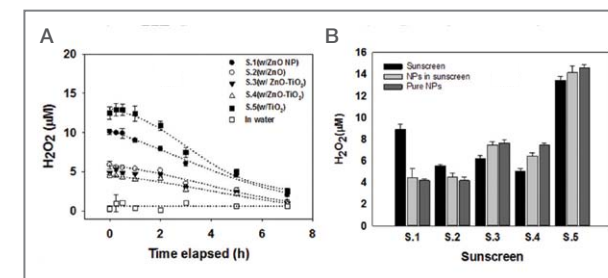


Figure 4 (A) Variation of H_2O_2 concentration in different sunscreen suspensions with time after ceasing UV irradiation. (B) H_2O_2 generated by sunscreens, NPs in sunscreens and pure NPs in the same amount as NPs initially present in each evaluated sunscreen.

Potential risk of metal oxide NPs from sunscreen released into pool water

The potential risk posed by the release of metal oxide NPs from sunscreens into pool water was estimated by using the experimental results from this study to calculate the expected concentration of H_2O_2 in a pool and applying it to a typical swimming pool operation scenario. The outdoor swimming park operated by the Seoul Metropolitan Government was used as our model. Under typical conditions, the total volume of pool water is $2167 m^3$, total visitors per day in the peak season is 1135 persons, and it was assumed that about

one third of the visitors (378 persons/group) plays in the pool before another group enters the pool. The pool water was assumed to circulate through the water treatment system within an hour and 3 times/day and a new group of visitors was assumed to have played in the pool before each circulation. Based on our calculations, the concentrations of H_2O_2 likely to be present in the swimming pool would be less than $0.2 \mu M$ for all types of sunscreens investigated. In addition, any residual concentration of H_2O_2 could be further reduced as a result of H_2O_2 quenching by organic substances in the pool. Therefore, the NPs in the sunscreens released into pool water are unlikely to impose an adverse effect on swimmers.

Conclusions

This study demonstrated that a significant amount of NPs in sunscreens may be released and accumulate in swimming pools. Although hydrogen peroxide (H_2O_2) can be generated by these NPs and other components released from the sunscreens as a result of the UV treatment process, the concentration of this potentially harmful ROS should remain below a level that would adversely affect human health.

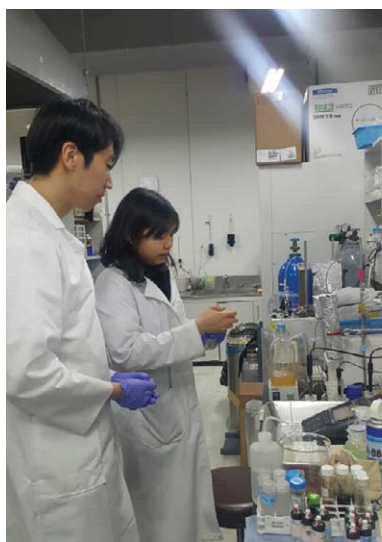
Note

This article and images are drawn from “Potential risks of TiO_2 and ZnO nanoparticles released from sunscreens into outdoor swimming pools” in *Journal of Hazardous Materials*, 2016, Vol. 317, pp. 312-318.

References

- [1] Mueller NC, Nowack B. *Environ. Sci. Technol.* 2008; 42: 4447-4453.

- [2] Kittler S, Greulich C, Diendorf J, Koller M, Epple M. *Chem. Mater.* 2010; 22: 4548-4554.
- [3] Hsiao IL, Huang YJ. *Sci. Total Environ.* 2011; 409: 1219-1228.
- [4] Rampaul A, Parkin IP, Cramer LP. *J. Photoch. Photobio. A.* 2007; 191: 138-148.
- [5] Aruoja V, Dubourguier HC, Kasemets K, Kahru A. *Sci. Total Environ.* 2009; 407: 1461-1468.
- [6] Wong SWY, Leung PTY, Djuricic AB, Leung KMY. *Anal. Bioanal. Chem.* 2010; 396: 609-618.
- [7] Hund-Rinke K, Simon M. *Environ. Sci. Pollut. R.* 2006; 13: 225-232.
- [8] Danovaro R, Bongiorni L, Corinaldesi C, Giovannelli D, Damiani E, Astolfi P, Pusceddu A. *Environmental Health Perspectives* 2008; 116(4): 441-447.



Feature Articles

Ion Conducting Nafion Membranes with a Porous Structure



Dirk
HENKENSMEIER

Fuel Cell Research Center,
National Agenda Research
Division
henkensmeier@kist.re.kr

Nafion membranes and their applications

Nafion and structurally similar materials are perfluorinated polymers and consist of a poly (tetrafluoroethylene) backbone with sulfonic acid-terminated side chains. The most striking feature of Nafion is its microphase separation into a hydrophobic phase, formed by the Teflon-like backbone, and a hydrophilic phase, formed by the sulfonic acid-terminated side chains [1]. The hydrophilic phase is highly hygroscopic and absorbs up to 20 water molecules per sulfonic acid group. This allows the sulfonic acid groups to be fully dissociated into polymer-bound sulfonate groups and freely mobile protons, and because the hydrophilic phase forms a practically continuous phase throughout the membrane, Nafion shows a remarkably high proton conductivity. The hydrophobic phase provides the polymer with mechanical strength and prevents it from swelling excessively in water. Because of the perfluorinated structure, Nafion also shows a high chemical stability against hydrolysis and radical attack.

The first generation of commercial Nafion was developed in the 1960s by Dupont. Since that time, it has become the standard material for most applications which use proton conducting membranes, e.g., automotive polymer electrolyte membrane fuel cells (PEMFC), vanadium redox flow batteries (VRFB), actuators and proton exchange membrane electrolyzers (PEM electrolyzers) [2, 3]. In these applications, the membrane acts as an electronic insulator between anode and cathode and needs to be gas tight to prevent crossover of hydrogen and oxygen in the fuel cell while being able

to rapidly transport protons between the anode and the cathode. Therefore, commercial Nafion membranes are non-porous dense membranes available in thicknesses of 25, 50, 125 and 175 μm (labeled Nafion 211, 212, 115 and 117, respectively).

Porous Nafion membranes

The introduction of pores is counterintuitive because pores would seem to increase gas permeability. However, if pores are only introduced selectively on a membrane surface, they do not affect gas permeability much, but do significantly increase the surface area of the membrane. In the fuel cell, this increases the membrane | electrode interfacial area. This is attractive because the distribution of water in the membrane electrode assembly is very critical during fuel cell operation. If the membrane dries out, its proton conductivity decreases dramatically. At the fuel cell cathode, oxygen is reduced to water. Some of this water diffuses back to the membrane and the rest is transported away by the air stream which supplies the electrodes with oxygen. If water is not efficiently transported away, it condenses in the porous structure of the electrode, limiting the availability of oxygen for the fuel cell reaction. This leads to a huge mass transfer overpotential [4]. We expect that a large membrane | electrode interfacial area helps to transport excess water from the electrode to the membrane, resulting in a well-humidified membrane (reducing membrane resistance) and a low mass transfer overpotential in the cathode. Work by others has indeed shown that an increased membrane | electrode interfacial area is beneficial for fuel cell performance. Using a very systematic approach, Shul et al. varied the interfacial area by casting the membrane in microstructured molds [5]. While this approach is scientifically sound, upscaling is difficult. In another approach, Thiele et al. spray coated the membrane on a porous electrode, which very probably also resulted in an enlarged interfacial area [6].

If pores are introduced all over a membrane, one has to distinguish between open pores (which are all

connected, as in filtration membranes) and closed pores (which are isolated). As far as we are aware, only Nafion with open pores has been reported so far. Such membranes can be used as porous substrates in which the pores are filled with another material, e.g., proton-conducting zirconium hydrogen phosphate for use in fuel cells [7] or KOH for use in alkaline water electrolyzers [8]. Another potential application could be as an acid catalyst, e.g., for hydrolysis of an acid labile educt, which could be hydrolysed while being filtrated through an acidic membrane.

A Nafion membrane with closed pores is a new material. While there is no immediate application, it could be very useful as a starting material for new, advanced materials. For example, the pores could be filled with a precursor which could pass the Nafion pore walls. Then the precursor could be reacted into a polymer or into nanoparticles, coating the Nafion pore walls. This could add stability to the membrane (coated by a silica layer) or add catalytic properties [9]. Catalysts could be cerium based in order to mitigate hydroxy radicals which form in a side reaction in the fuel cell and are a major source of membrane degradation [10]. Noble metal catalysts could also be added to react hydrogen and oxygen into water (although Nafion blocks gases, it still shows an oxygen permeability of about 0.8 Barrer [11]), humidifying the membrane from the inside [12]. This would eliminate the need of an external humidifier, reducing system complexity and the overall system weight. By coating the pore walls with an appropriate chemistry, it is expected that a layer with a high density of sulfonic acid groups could probably be achieved. Such a pathway along the pore walls would show a very low tortuosity, possibly decreasing membrane resistance.

Mechanisms for pore formation

Most published procedures, apparently all leading to open pore structures, involve the preparation of a composite membrane from which a solid porogene is later leached out by immersing the membrane in a

suitable bath [7, 8, 13]. Another method is to boil a Nafion membrane in a mixture of water and propylene carbonate (PC). In the acidic environment of the soft swollen membrane, PC degrades, forming CO_2 bubbles which expand the membrane [14]. In a similar approach, a Nafion membrane is swollen in supercritical CO_2 ; releasing the pressure expands the membrane [15].

In our work we prepared porous membranes in a single casting step by simply adding a liquid organic porogene to the casting solution *ortho*-dichlorobenzene (ODB). By adjusting the composition of the solvent mixture, the ion exchange capacity of Nafion, the amount of porogene, and the temperature during solvent evaporation, the structure of the porous membrane could be adjusted, allowing us to selectively produce dense membranes with a porous surface layer or to produce membranes with closed pores throughout the whole membrane. The structures evolve when the solvents with the lowest boiling point evaporate. At a certain point, ODB (boiling point 178-180°C) phase separates from the solvent mixture and forms ODB droplets (Figure 1). If the viscosity of the polymer solution is low enough, the density difference between ODB and a concentrated Nafion dispersion makes the droplets rise to the surface, leaving a dense polymer membrane coated by ODB droplets, which finally leads to formation of surface pores. If the viscosity of the solution is higher, e.g., if phase separation of ODB and the solvent mixture occurs at a later stage, the ODB droplets will be trapped in the membrane, resulting in a fully porous membrane.

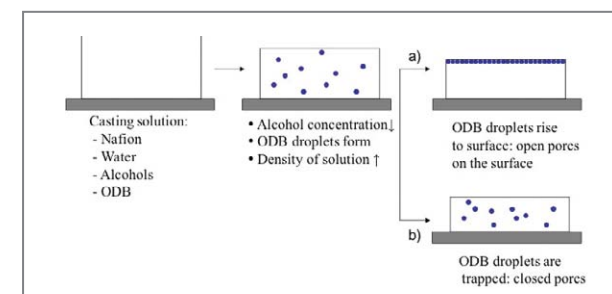


Figure 1 Mechanism for production of porous Nafion membranes; after casting a polymer solution on a glass plate, the solvents are allowed to evaporate, leaving a dry polymer film.

Fabrication of porous Nafion membranes

When we used a Nafion dispersion from Dupont called SE-20092 (20%Nafion, solvent: probably 20% water and an equimolar mixture of ethanol and n-propanol) and added 0.18 g ODB per 1 ml dispersion, we reproducibly obtained membranes which were dense but showed a porous layer on the upper surface [16, 17]. The membranes showed a similar structure to membranes prepared by breath figures (Figure 2). Breath figures can be seen when water condenses on a cold surface, like a mirror in the bathroom. In the polymer world, breath figures are observed when water condenses on a cold polymer solution, e.g., a chloroform solution of a polysulfone, which cools down significantly during solvent evaporation because of the positive evaporation enthalpy of chloroform. As a result, water droplets collect on the surface of the polymer solution, leading to a regular honeycomb structure [18]. For Nafion dispersions, the breath figure mechanism can be ruled out because water is freely miscible with water and even contains water as the highest boiling solvent.

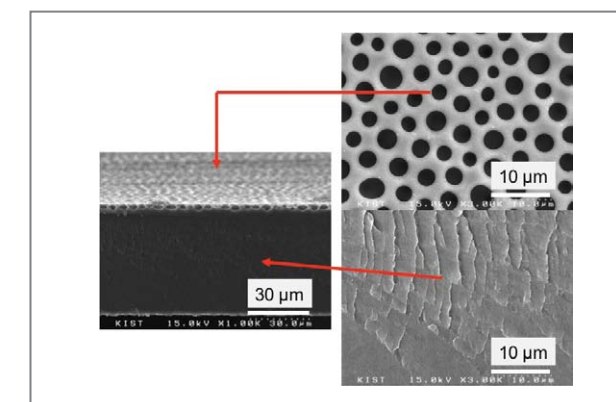


Figure 2 SEM images of a Nafion membrane with open pores on the surface.

In order to produce closed pores throughout the membrane, the casting solution was changed into a water-free dispersion by removing the solvents from commercial Nafion DE2021 dispersion and redispersing

the polymer in ethanol to achieve a 10% solution [19]. After the addition of 150 mg ODB / ml dispersion, the polymer solution was cast on a glass plate and the solvents were evaporated to give a solid membrane. As expected, the absence of water prevented early demixing of ODB and ethanol, and the polymer gelled or solidified around ODB rich phases, leading to fully porous membranes (Figure 3).

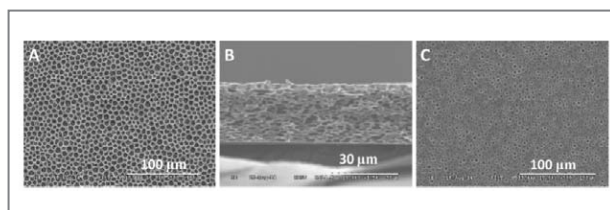


Figure 3 SEM images of (A) air surface, (B) crosssectional area and (C) glass surface of a Nafion membrane with closed pores.

For the fully porous membranes, the effect of temperature on the casting conditions was tested by drop casting the casting solution into a petri dish and evaporating the solvents at 0°C, 20°C and 50°C. The lower temperature reduced the viscosity of the casting solution, leading to large ODB rich phases which were trapped on the bottom side of the membrane (Figure 4A). When the temperature was increased to 50°C, the viscosity of the casting solution decreased, and ODB droplets easily rose to the surface, leading to the formation of a dense membrane with small pores on and below the upper surface (Figure 4C).

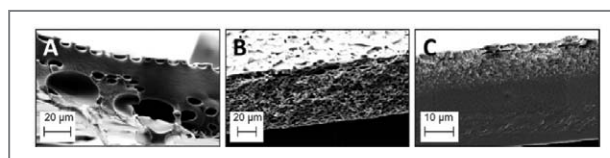


Figure 4 Influence of temperature on pore formation. (A) 0°C, (B) 20°C, (C) 50°C.

Application of porous Nafion membranes in a fuel cell

When a 50-70 μm thick surface porous Nafion

membrane was operated in a PEM fuel cell at a low relative humidity of 50% with the porous surface on the cathode side, a stable performance similar to that reported in the literature for an 11 μm thick membrane [20] was obtained (Figure 5, blue curve), demonstrating both the efficiency of the tested system and the quality of the membrane. The beneficial effect of the pores was proven by comparing the performance of our membrane with one that was about 40% thinner, but dense, and prepared using a similar approach but without ODB. Even though it should have shown a larger resistance, our thick porous membrane performed better than the thin dense membrane. When pores were introduced to a thin membrane, current density at 0.4V increased by 16%. This strongly indicates that the porous membranes are better humidified than dense membranes.

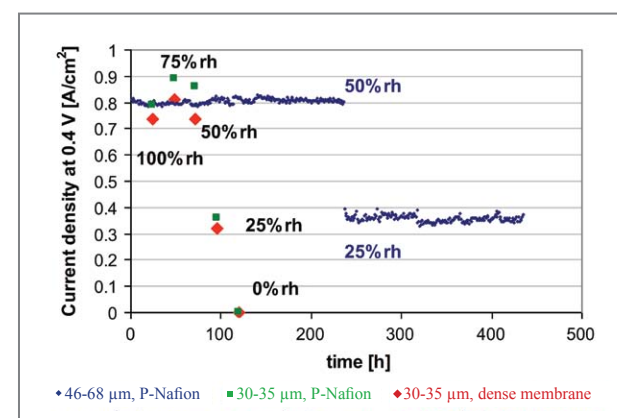


Figure 5 Membrane with open pores on the surface: performance in a fuel cell at 95°C.

In a porous catalyst electrode, the formation of a so-called three-phase boundary is important for good cell performance. The tpb is the area of catalyst particles at which fuel cell reactions can occur because all reactants are available: oxygen (supplied through the porous structure), electrons (through the carbon support) and protons (through Nafion, which is added to the electrode as binder for the catalyst particles). If the product water is not transported away efficiently, electrode flooding occurs. The Nafion binder swells, reducing the size of the

pores, and water droplets fully block some of the pores, preventing oxygen from reaching the catalyst sites. By cyclic voltammetry, the size of the electrochemically active platinum surface area can be estimated. As expected, the membranes with pores on the surface led to higher ECSA values. For example, the ECSA increased from 50 m^2/gPt , when a commercial Nafion 212 membrane was used, to 134 m^2/gPt under the same conditions when a slightly thicker P-Nafion membrane was used (Table 1).

To test their suitability as starting materials for further developments, fully porous membranes were also assembled into fuel cells. The hydrogen crossover for fully humidified membranes was about 10 times larger than for dense membranes [19]. This is a large crossover, but low enough to indicate that the membrane has no through-pores which directly connect anode and cathode sites.

Conclusions and outlook

By adding ODB to a solution containing Nafion, alcohol and/or water, it is possible to obtain dense membranes with a porous surface, and porous membranes with a closed pore structure, depending on the formulation. The first membrane type was successfully tested in fuel cells, resulting in enhanced

platinum utilization and performance. For the second membrane type, no real application could be targeted yet, but its unique morphology makes it an attractive starting material for further developments. For example, future work could focus on filling the pores with a conducting material, e.g. sulfuric acid for the use in vanadium redox flow batteries. Also, a catalyst for scavenging radicals and/or reacting crossed over gases to water could be added, or a material which adds mechanical strength and/or activates the pore surface for proton conduction.

Note

This article and images are based on the articles "Porous Nafion membranes" in the *Journal of Membrane Science*, 2016, Vol. 520, pgs. 723-730 and "Nafion Membranes with a Porous Surface" in the *Journal of Membrane Science*, 2014, Vol. 460, pgs. 199-205.

References

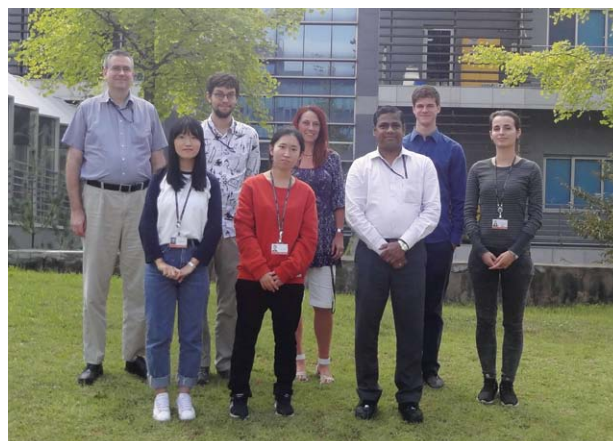
- [1] Hsu WY, Gierke TD. *J. Membr. Sci.* 1983; 13:307-326.
- [2] Grot W, *Fluorinated Ionomers*, 2nd edition, William Andrew (Elsevier), Oxford, 2011.

Table 1 Electrochemically Active Surface Area (ECSA) of the fuel cell cathode layer for different membranes and conditions. P-Nafion: 30 μm thick, dense membranes with surface pores.

Membrane type	MEA batch	temperature [°C]	Relative humidity an./ca. [%]	ECSA (m^2/gPt)	Pt Utilization (%)
N212	1	65	75/75	50	17
N212, additive in catalyst ink [17]	2	65	75/75	57	19
P-Nafion	3	65	75/75	134	44
P-Nafion	3	65	100/100	141	46
N212 from [21]	4	80	ca. 80/60	ca. 88	ca. 29
P-Nafion	3	80	80/60	87	28
Nafion 211	5	95	100/100	46	15
P-Nafion (other MEA)	6	95	100/100	64	21
P-Nafion	3	95	100/100	52	17
P-Nafion	3	95	75/75	52	17

- [3] Kusoglu A, Weber AZ. *Chem Rev.* 2017; 117:987-1104.
- [4] Deabate S, Gebel G., Huguet P, Moprin A, Pourcelly G. *Energy Env. Sci.* 2012; 5: 8824-8847.
- [5] Koh JK, Jeon Y, Cho YI, Kim JH, Shul YG. *J. Mater. Chem. A.* 2014; 2:8652-8659.
- [6] Klingele M, Britton B, Breitwieser M, Vierrath S, Zengerle R, Holdcroft S, Thiele S. *Electrochem. Commun.* 2016; 70:65-68.
- [7] Song MK, Kim YT, Hwang JS, Ha HY, Rhee HW. *Electrochem. Solid State Lett.* 2004; 7: A127-A130.
- [8] Aili D, Hansen MK, Andreasen JW, Zhang J, Jensen JO, Bjerrum NJ, Li Q. *J. Membr. Sci.* 2015; 493:589-598.
- [9] Nambi Krishnan N, Henkensmeier D, Jang JH, Kim HJ. *Macromol. Mater. Eng.* 2014 299:1031-1041.
- [10] Pearman BP, Mohajeri N, Brooker RP, Rodgers MP, Slattery DK, Hampton MD, Cullen DA, Seal S. *J. Power Sources.* 2013; 225:75-83.
- [11] Fontananova E, Trotta F, Jansen JC, Drioli E. *J. Membr. Sci.* 2010; 348: 326-336.
- [12] Watanabe M, Uchida H, Seki Y, Emori M, Stonehart P. *J. Electrochem. Soc.* 1996; 143:3847-3852.
- [13] Guo DJ, Fu SJ, Tan W, Dai ZD. *J. Mater. Chem.* 2010; 20:10159-10168.
- [14] Hestekin JA, Gilbert EP, Henry MP, Datta R, Martin EJS, Snyder SW. *J. Membr. Sci.* 2006; 281:268-273.
- [15] Howard EG, Lloyd RB, E.I. Du Pont de Nemours and Company, EP Patent 1152830B1, 2001.
- [16] Dang QK, Henkensmeier D, Nambi Krishnan N, Jang JH, Kim HJ, Nam SW, Lim TH. *J. Membr. Sci.* 2014 460:199-205.
- [17] Henkensmeier D, Dang QK, Nambi Krishnan N, Jang JH, Kim HJ, Nam SW, Lim TH. *J. Mater. Chem.* 2012 22:14602-14607.
- [18] Xu Y, Zhu B, Xu Y. *Polymer.* 2005; 46:713-717.
- [19] Joseph D, Büßselmann J, Harms C, Henkensmeier D, Larsen MJ, Dyck A, Jang JH, Kim HJ, Nam SW. *J. Membr. Sci.* 2016 520:723-730.
- [20] Tu Z, Zhang H, Luo Z, Liu J, Wan Z, Pan M. *J. Power Sources.* 2013; 222: 277-281.
- [21] Kim KH, Lee KY, Kim HJ, Cho E, Lee SY, Lim TH,

Yoon SP, Hwang IC, Jang JH. *Int. J. Hydrog. Energy.* 2010; 35:2119-2126.



Preparation of fucoxanthin-loaded Nanoparticles composed of casein and chitosan with improved fucoxanthin bioavailability

Journal of Agricultural and Food Chemistry
2016 Dec./Vol. 64 No. 49/9428-9435

Song Yi KOO, Il Kyoon MOK, Cheol Ho PAN,
and Sang Min KIM (kimsm@kist.re.kr)

To facilitate the utilization of fucoxanthin (FX), a valuable marine carotenoid, in the food industry, FX-loaded casein nanoparticles (FX-CN) and chitosan-coated FX-CN (FX-CS-CN) were developed using the FX-enriched fraction from *Phaeodactylum tricornutum*. Two nanoscale particles (237 ± 13 nm for FX-CN and 277 ± 26 nm for FX-CN-CN) with spherical and smooth surfaces showed over 71% encapsulation efficiency and a polydispersity index (PDI) value of 0.31–0.39 in water. Owing to the chitosan coating, FX-CS-CN showed a positive zeta potential (24.00 mV), whereas that of FX-CN was negative (–12.87 mV). *In vitro* simulated digestion demonstrated better FX bioaccessibility from the nanoparticles versus *P. tricornutum* powder (Pt-powder) and from FX-CN versus FX-CS-CN. However, in C57BL/6 mice, fucoxanthinol absorption to the blood circulation was two times higher for FX-CS-CN versus FX-CN, possibly due to increased retention or adsorption to mucin by the cationic biopolymer in the chitosan-coated particles. These results demonstrate that improvements to the bioavailability and water dispersibility of FX-CS-CN can be made that will enable its application in the food industry.

Individual role of the physicochemical characteristics of nanopatterns on tribological surfaces

ACS Applied Materials & Interfaces
2016 Nov./Vol. 8 No. 44/30590-30600

Prashant PENDYALA, Harpreet S. GREWAL, Hong Nam KIM,
Il Joo CHO, and Eui Sung YOON (esyoon@kist.re.kr)

Nanoscale patterns have dimensions that are comparable to the length scales affected by intermolecular and surface forces. In this study, we systematically investigated the individual roles of curvature, surface energy, lateral stiffness, material, and pattern density in the adhesion and friction of nanopatterns. We fabricated cylindrical and mushroom-shaped polymer pattern geometries containing flat- and round-topped morphologies using capillary force lithography and nanodrawing techniques. We showed that the curvature, surface energy, and density of the patterns predominantly influenced the adhesive interactions, whereas lateral stiffness dominated friction by controlling the geometrical interaction between the indenter and pillar during sliding. Interestingly, in contrast to previous studies, cylindrical and mushroom-shaped pillars showed similar adhesion characteristics but very different frictional properties. Using fracture mechanics analysis, we showed that this phenomenon is due to a larger ratio of the mushroom flange thickness (t) to the radius of the pillar stem (ρ), and we proposed a design criterion for mushroom patterns to exhibit a geckolike effect. The most important result of our work is the discovery of a linear master curve in the graph of adhesion versus friction for pillars with similar lateral stiffness values that is independent of curvature, material, surface energy, and pattern density. These results will aid in the identification of simple pattern parameters that can be scaled to tune adhesion and friction and will help broaden the understanding of nanoscale topographical interactions.

Significant exciton brightening in monolayer tungsten disulfides via fluorination: n-type gas sensing semiconductors

Advanced Functional Materials

2016 Nov./Vol. 26 No. 42/7551–7559

Young In JHON, Young Hee KIM, June PARK, Jae Hun KIM, Taik Jin LEE, Min Ah SEO, and Young Min JHON (ymjhon@kist.re.kr)

Monolayer transition-metal dichalcogenides (TMDCs) have recently emerged as promising candidates for advanced photonic and valleytronic applications due to their unique optoelectronic properties. However, the low luminescence efficiency of monolayer TMDCs has significantly hampered their use in these fields. Here it is reported that the photoluminescence efficiency of monolayer WS₂ can be remarkably enhanced up to fourfold through fluorination, surpassing the reported performance of molecular and/or electrical doping methods. Its degree is easily controlled by changing the fluorine plasma duration time and can also be reversibly tuned via additional hydrogen plasma treatment, allowing for its versatile tailoring for interfacial band alignment and customized engineering. The striking photoluminescence improvement occurs via a substantial transition of trions to excitons as a result of the strong electron affinity of fluorine dopants, and the fluorination enables unprecedented detection of n-type NH₃ gas in WS₂ due to changed excitonic dynamics showing excellent sensitivity (at least down to 1.25 ppm). This work provides valuable strategies and insights into exciton physics in monolayer TMDCs, opening up avenues toward highly-efficient 2D light emitters, photovoltaics, nanosensors, and optical interconnects.

Free-electron creation at the 60° twin boundary in Bi₂Te₃

Nature Communications

2016 Aug./Vol. 7 No. 12449

Kwang Chon KIM, Joo Hwi LEE, Byung Kyu KIM, Won Young CHOI, Hye Jung CHANG, Sung Ok WON, Beom Jin KWON, Seong Keun KIM, Dow Bin HYUN, Hyun Jae KIM, Hyun Cheol KOO, Jung Hae CHOI, Dong Ik KIM, Jin Sang KIM (jskim@kist.re.kr) and Seung Hyub BAEK (shbaek77@kist.re.kr)

Interfaces, such as grain boundaries in a solid material, are excellent regions to explore novel properties that emerge as the result of local symmetry-breaking. For instance, at the interface of a layered-chalcogenide material, the potential reconfiguration of the atoms at the boundaries can lead to a significant modification of the electronic properties because of their complex atomic bonding structure. Here, we report the experimental observation of an electron source at 60° twin boundaries in Bi₂Te₃, a representative layered-chalcogenide material. First-principles calculations reveal that the modification of the interatomic distance at the 60° twin boundary to accommodate structural misfits can alter the electronic structure of Bi₂Te₃. The change in the electronic structure generates occupied states within the original bandgap in a favourable condition to create carriers and enlarges the density-of-states near the conduction band minimum. The present work provides insight into the various transport behaviours of thermoelectrics and topological insulators.

Ordered nanoscale heterojunction architecture for enhanced solution-based CuInGaS₂ thin film solar cell performance

Advanced Energy Materials

2016 Dec./Vol. 6 No. 24/1601114

Nilesh BARANGE, Van Ben CHU, Min Woo NAM, In Hwan AHN, Young Dong KIM, Il Ki HAN, Byoung Koun MIN (bkmin@kist.re.kr) and Doo-Hyun KO

Nanopatterned CuInGaS₂ (CIGS) thin films synthesized by a sol-gel-based solution method and a nanoimprint lithography technique to achieve simultaneous photonic and electrical enhancements in thin film solar cell applications are demonstrated. The interdigitated CIGS nanopatterns in adjacent CdS layer form an ordered nanoscale heterojunction of optical contrast to create a light trapping architecture. This architecture concomitantly leads to increased junction area between the p-CIGS/n-CdS interface, and thereby influences effective charge transport. The electron beam induced current and capacitance–voltage characterization further supports the large carrier collection area and small depletion region of the nanopatterned CIGS solar cell devices. This strategic geometry affords localization of incident light inside and between the nanopatterns, where created excitons are easily dissociated, and it leads to the enhanced current generation of absorbed light. Ultimately, this approach improves the efficiency of the nanopatterned CIGS solar cell by 55% compared to its planar counterpart, and offers the possibility of simultaneous management for absorption and charge transport through a nanopatterning process.

Nanostructured PVDF membrane for MD application by an O₂ and CF₄ plasma treatment

Desalination

2016 Dec./Vol. 399/178-184

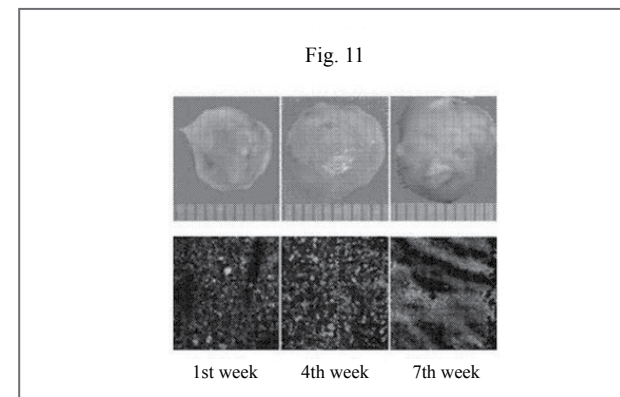
Seong Pil JEONG, Bong Su SHIN, Won Jin JO, Ho Young KIM, Myoung Woon MOON and Seock Heon LEE (seocklee@kist.re.kr)

Recently, various nanotechnologies have been utilized with regard to membrane modification due to their high activities and the low cost of the nanomaterials involved. In order to enhance the hydrophobicity of the membrane surface for membrane distillation applications by decreasing the surface energy, a radio-frequency plasma-enhanced chemical vapor deposition (RF-PECVD) process is suggested with surface nanostructuring and a subsequent hydrophobic coating step. In this research, a commercial PVDF membrane was modified by plasma treatments with the two different gases of O₂ and CF₄. The water contact angles of the active layers increased from 73° to 117° and 101° and the fluxes of the treated membranes increased to 63% and 27.9% as compared to a virgin PVDF membrane when the feed used was D.I. water by the O₂ and CF₄ plasma modifications, respectively. Defluorination over a long exposure time (120 min) for plasma treatment and increase of the overall hydrophobicity (the decrease of the contact angle hysteresis) by the HMDSO coating were the reasons for the flux variations for the plasma modified membranes.

Biodegradable and thermosensitive poly(organophosphazene) hydrogel, preparation method thereof and use thereof

US 9526699 (2016-12-27), KR 0784485 (2007-12-04)
Soo Chang SONG (scsong@kist.re.kr)

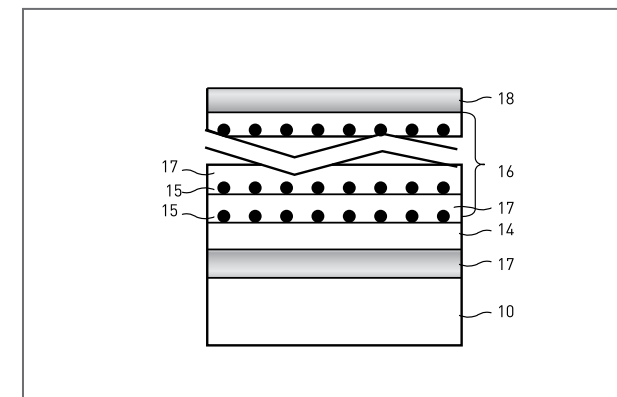
The present invention relates to a biodegradable and thermosensitive poly (organophosphazene) with a functional group, a preparation method thereof, and a use thereof for delivery of bioactive substances. According to the present invention, poly (organophosphazene) is a phosphagen-based polymer showing biodegradability, thermosensitivity, and sol-gel phase transition depending on temperature change, whereby when administered into a living body with bioactive substances such as drugs, the poly (organophosphazene) forms a gel-phase at body temperature to be capable of controlled release of the bioactive substances. Further, the poly (organophosphazene) has functional groups to chemically bind with bioactive substances through an ionic bond, covalent bond, or coordinate covalent bond to be capable of a sustained release of the bioactive substances due to its good binding property. Therefore, the poly (organophosphazene) is useful as a delivery material for bioactive substances.



Plasmonic nano-color coating layer and method for fabricating the same

US 9482798 (2016-11-01) KR 1499487 (2015-03-02)
Kyeong Seok LEE (kslee21@kist.re.kr)

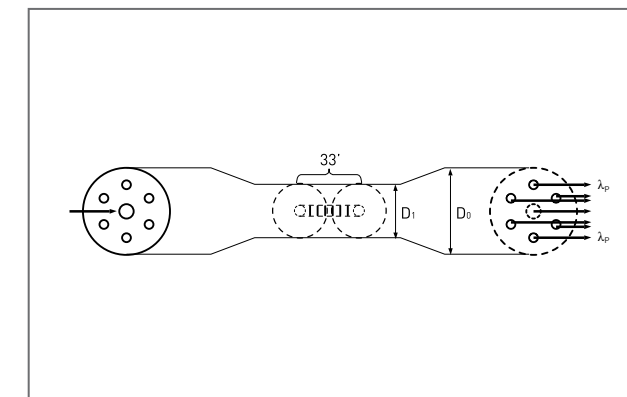
A plasmonic nano-color coating layer includes a composite layer including a plurality of metal particle layers and a plurality of matrix layers and having a periodic multilayer structure in which the metal particle layers and the matrix layers are alternately arranged, a dielectric buffer layer located below the composite layer, and a mirror layer located below the dielectric buffer layer, wherein the color of the plasmonic nano-color coating layer is determined based on a nominal thickness of the metal particle layer and a separation between the metal particle layers.



Optical element using multicore optical fiber grating and method for processing optical signal using the same

US 9477045 (2016-10-25) KR 1506931 (2015-03-24)
Sang Bae LEE (sblee@kist.re.kr)

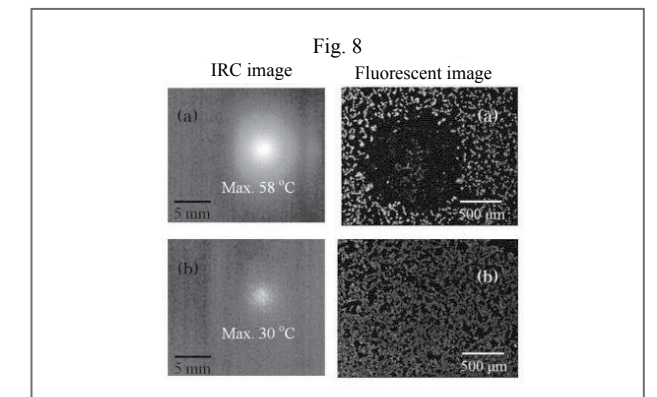
An optical element includes a multicore optical fiber, the multicore optical fiber including an inner core and at least one peripheral core arranged around the inner core and having an effective refractive index different from that of the inner core, and an optical fiber grating formed at the multicore optical fiber to cause an optical signal to be coupled between different cores among the inner core and at least one peripheral core. The optical element allows a signal of a specific wavelength to be dropped or added from an optical signal. Since the optical element may be fabricated easily, designed in a small size and mass-produced reproducibly at low costs, the optical element may be advantageously utilized for an optical communication network such as a wavelength division multiplexing network, an ultra-high speed optical communication system, an optical sensor system or the like.



Method of analyzing binding efficiency of adhesive nanoparticles

US 9442115 (2016-09-13) KR 1369392 (2014-02-25)
Young Min JHON (ymjhon@kist.re.kr)

Provided is a method of analyzing binding efficiency of adhesive nanoparticles. The method includes (a) injecting a solution containing nanoparticles into a first chamber slide, (b) evaporating only the solution from the first chamber slide into which the solution containing the nanoparticles is injected, and measuring a saturation temperature using a thermal imager while radiating light from a light source, (c) injecting cells into a second chamber slide, (d) injecting a solution containing nanoparticles into the second chamber slide in which the cells are cultured, (e) removing nanoparticles which are not bound to the cells from the second chamber slide into which the cells and the nanoparticles are injected, and (f) evaporating only the solution from the second chamber slide from which the nanoparticles are removed, and measuring a saturation temperature using a thermal imager while radiating light from the light source.

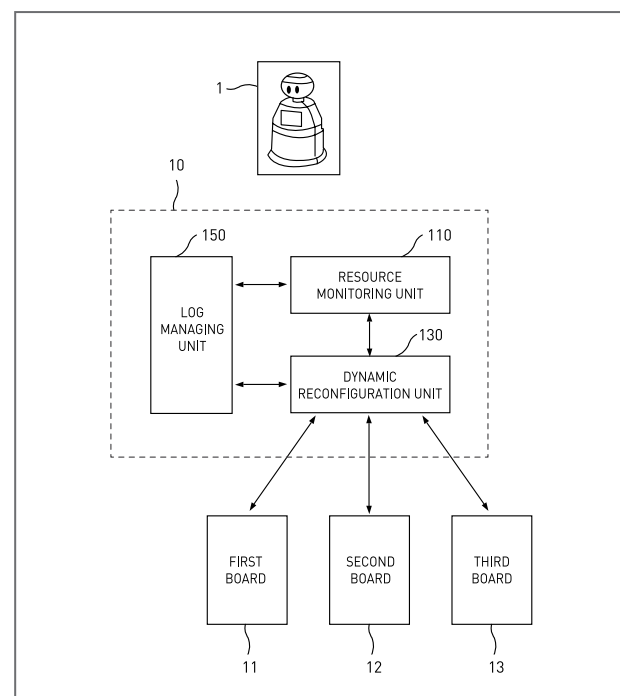


Device and method for dynamic reconfiguration of robot components

US 9415505 (2016-08-16) KR 1437483 (2014-08-28)

Sang Chul AHN (asc@kist.re.kr)

A device for dynamic reconfiguration of robot components includes: a resource monitoring unit for monitoring resources of a plurality of boards on which components for executing tasks of a robot are loaded; a dynamic reconfiguration unit for dynamically reconfiguring components of the boards in case one of the boards is at a risk for a scarcity of resources; and a log managing unit for storing a configuration of present components and a configuration of reconfigured components. Accordingly, it is possible to recognize a scarcity of resources in advance while the robot is operating and prevent the robot from malfunctioning by distributing the components.



1. Byung Gwon LEE Reappointed as KIST's President

March 3, 2017

On March 3, the National Research Council of Science and Technology (NST) announced the reappointment of the current president of KIST, Dr. Byung Gwon LEE, to a second term. His second term is scheduled to begin on March 13.

President LEE earned a Master's degree in Chemical Engineering from Seoul National University's Department of Chemical Engineering in 1982 and later received a Ph.D. in Chemical Engineering from the University of Akron in the U.S. He joined KIST in 1982 and served as director of the Energy and Environmental Research Division, director of the Research Planning and Coordination Division, and vice president of KIST, before taking up his current role as the organization's president.

The board of directors decided upon his reappointment after KIST received a rating of "very good" from the Korean government's rigorous organizational evaluation for the three years he was in office. President LEE's reappointment marks the initial implementation of the Korean government's efforts to reward, through offers of reappointment, heads of organizations that receive high evaluation scores.

During his first three-year term, KIST greatly expanded its Open Research Program (ORP), which was designed to address such globally-significant social issues as the early detection of dementia, integrated green tide removal technology, the development of plant factories, avian influenza prevention technology, quantum computing, and nano neuron network mimicry. As a result of the ORP, KIST has made major achievements in each of these areas, as exemplified by the new technology that allows for the early diagnosis of Alzheimer's via a simple blood test technology expected to generate approximately 330 billion KRW in royalties.

In addition, KIST has greatly strengthened its cooperative ties with academia by installing four joint research laboratories: two at Seoul National University (next-generation functional connectomes and artificial photosynthesis materials), one at KAIST (next-generation

deep learning algorithm), and one at POSTECH (quantum computing). By combining mutually complementary research capabilities, KIST is working to secure world-class excellence.

KIST's excellence in research has been recognized internationally, such as when Reuters ranked it as the world's 6th most innovative research institution for two years in a row (2016 and 2017). Furthermore, the Outstanding National R&D Outcomes list published by the Ministry of Science, ICT and Future Planning included more projects from KIST than from any other institution: eight KIST projects were on the list in 2015 and six in 2016.

2. KIST Participates in the Opening of Sangwolgot's Science Station

March 3, 2017

On March 3, KIST took part in the opening ceremony for the "Science Station," an underground science hall located within the Sangwolgot subway station. The organizations represented at the ceremony had been participants in the Science Station project and included: the Ministry of Science, ICT and Future Planning; the Korea Foundation for the Advancement of Science and Creativity; Seoul Metropolitan City, Seongbuk District; and Seoul Metro.

The goal of the Science Station is to utilize a highly visible public area in order to promote scientific interest and information in an interesting, unobtrusive way. The six participating organizations first signed an agreement in December 2015, and last month saw joint construction on a lecture hall, a bio living lab, and an exhibition space, all intended for scientific popularization and education among the general public.

The opening ceremony featured a video presentation titled "Sneak Preview of the Science Station," which gave the audience a taste of what the exhibition had in store, including glimpses of the multi-venue displays in Sangwolgot Station's story zone (platforms), lecture zone (lecture hall), and scientist zone (basement

exhibition area). Once the ceremony was concluded, the Science Station immediately went fully operational by conducting an educational program for infants that combines science with fairytales.

KIST's president, Byung Gwon LEE, commented on the project by saying, "The Science Station provides added value to the subway station by serving as a place where people can learn about science and technology, and where we can plant a seed to help future generations grow into scientists. KIST will spare no effort in making the Science Station a scientific and cultural experience that will greatly vitalize the local community."

3. KIST Achieves Second Consecutive Year Ranked as the World's 6th Most Innovative Research Institute

March 1, 2017

On March 1, KIST announced that, for the second year in a row, it was ranked by Reuters as the world's 6th most innovative research institution. This ranking was based on research outcomes, scientific journal publications, and received patents. Specific criteria included:

- The number of academic papers listed in the Clarivate Analytics Web of Science database from 2009 to 2014.
- The number of patent applications listed in the Derwent World Patents Index and the Derwent Innovations Index from 2009 to 2014.
- Patent/paper citations counted up until March 2016.

Organizations that met the aforementioned criteria were further narrowed to ones that filed at least 70 international patents with WIPO. Total scores were calculated by summing up the current 50% weighting and the other 50% weighting of patent citations and patent citation impacts.

This year's list was topped by the U.S. Department of Health and Human Services (HHS, ranked 4th in 2016), followed by France's Alternative Energies and Atomic Energy Commission (CEA, 1st in 2016), Germany's Fraunhofer Society (2nd in 2016), Japan's Science &

Technology Agency (3rd in 2016) and the National Institute of Advanced Industrial Science & Technology (7th in 2016). Coming in 6th, KIST ranked 3rd among Asian government research centers and was the only Korean research institution included on the list, ahead of such internationally renowned research institutions as the French National Center for Scientific Research (8th), the Chinese Academy of Sciences (11th), Japan's RIKEN (13th), and Germany's Max Plank Society (16th).

The USA and Germany led the list with five institutions apiece, followed by France and Japan, who each had four. By continent, Europe, Asia, and North America contributed 11, 8, and 6 institutions, respectively.

For its profiles of the top 25 institutions, Reuters included information on each one's patent applications and registrations during the evaluation period, as well as its economic impact.

4. KU-KIST Team Identifies the Mechanism of Hippocampal Place Cells

February 20, 2017

The hippocampus is an area of the brain that plays an essential role in remembering experiences. Because cells in this region encode information on specific locations, they are referred to as "place cells" and essentially act as a GPS in the human body. Dr. Sebastien ROYER of KIST's Brain Science Institute recently announced that a team of researchers working under the auspices of the KU-KIST Academic-Research Cooperation Program have identified the mechanism of place cells, further clarifying their involvement in the perception and memory formation of spaces, events and situations. Dr. June Seek CHOI, Professor of Psychology at Korea University (KU), led the team from the university which worked jointly with the KIST team headed by Dr. ROYER.

Place cells are nerve cells that help people and animals recognize locations and determine spatial coordinates. A study on hippocampal place cells, considered an advanced topic in the field of behavioral neuroscience, was awarded

the Nobel Prize in Physiology or Medicine in 2014. In contrast to the theory that all place cells record and save spatial information in the same manner, the KU-KIST research team discovered that place cells are actually of two types, depending on whether they accumulate spatial or non-spatial (sensory) information. Furthermore, the team found that the cells are arranged in an orderly fashion into upper and lower layers according to the anatomical structure of the hippocampus.

In the study, the neural activity of laboratory mice was recorded as they walked on a treadmill which had either a rough or smooth surface or various tactile landmarks attached, such as bumps. The research team inserted a microelectrode (silicon probe) comprised of semiconductor chips into the hippocampi of the lab mice to simultaneously record the activities of dozens to hundreds of place cells. Place cells were divided into two types based on the way they were activated. The first group of place cells was activated at a certain location on the treadmill, consistent with place cell theory. The second group was activated by certain tactile landmarks, regardless of their location on the treadmill. For instance, the second group of place cells was activated by the bumpy projections on the treadmill, but was deactivated immediately once the tactile landmark was removed. On the other hand, when the same tactile condition was created at a different location on the treadmill, a similar activation pattern was observed. The activation methods for both types of place cells were observed under a wide range of experimental conditions and were distinguished as follows:

- **Place Cell Group 1:** Context-modulated cells that perceive the coordinates of a spatial location.
- **Place Cell Group 2:** Landmark vector cells that recognize major geographic features based on the senses.

The KU-KIST research team is the world's first to discover that these two types of place cells are aligned along different layers within the same area of the hippocampus. Preceding studies on place cells have concentrated on the horizontal distribution of the cells according to areas of the hippocampus, but the KU-KIST research team functionally distinguished the vertical distribution of place cells along the depth of the same area

of the hippocampus. As Dr. ROYER explains, "We have taken a step closer to understanding how the hippocampus, which plays a critical role in the memory of animals and humans, encodes the abstract information related to places. These results will provide clues to discovering revolutionary ways to substitute the neural circuits damaged by memory-related conditions such as amnesia and dementia, provide new algorithms for artificial intelligence, and be applied to various other areas."

5. KIST Team Successfully Cultivates Neural Circuits in the Laboratory

February 13, 2017

A KIST-based research team has recently developed a technology to reproduce brain tissue in a biological material using a cell culturing process. Led by Drs. Eun Mi HUR and Nak Won CHOI of KIST's Brain Science Institute, the joint research team designed a method to align collagen fibers in a certain direction so as to directionally guide the growth of axons when cultivating nerve cells in a 3D environment inside collagen. The team successfully reconstructed a CA3-CA1 neural network to allow nerve cells extracted from the hippocampus to divide and grow along the aligned collagen fibers. They also experimentally proved that the neural network had both structural and functional connectivity.

Cells and other elements within the human body are often arranged in specific directions, thus creating structural attributes that allow biological functions to occur properly. Therefore, the ability to implement and adjust the directionality of cells when attempting to engineer tissues and organs in an environment outside the body means that it is now possible to mimic external tissue structures as well as their functions. The significance of this study is that it provides a solution to the issue of creating directionality in cells in a biological material (a three-dimensional environment outside the body) that is actually used in a cell culturing process. It resulted in the successful reconstruction of brain tissue outside the body, where numerous neural circuits could

be clearly distinguished anatomically. In commenting on the study, Dr. CHOI suggested that, “It can be applied to the reconstruction of a normal neural network as well as abnormal and diseased neural networks that are characteristic of Alzheimer’s and Parkinson’s disease.” Dr. HUR predicted that “by converging this technology with patient-derived stem cell technology, we will be able to take a step closer to understanding the association between diverse brain diseases and disorders and the dysfunctions of neural networks.”

In addition to Drs. CHOI and HUR, other team members included: Dr. Soo Hyun KIM, formerly in the KIST Star post-doctoral program and faculty member at the University of Science and Technology (UST), currently working for SK Biopharmaceuticals; Dr. Sun Kyung IM of the Neural Science Research Group and Dementia DTC Convergence Research Group; Dr. Soo Jin OH of the Neural Science Research Group, Dementia DTC Convergence Research Group and Neuroglial Cell Research Group; and other domestic researchers, including students at UST. The outcomes of this study are all the more meaningful as they were achieved solely by Korean researchers. Results of this study were published online on February 1, 2017 in *Nature Communications*.

6. KIST-MIT Research Team Becomes the World’s First to Demonstrate Zero-Power Memory Elements

January 31, 2017

A Korean research team led by Dr. Seong Hoon WOO of KIST’s Spin Convergence Research Group, working in conjunction with a team headed by Dr. Geoffrey BEACH of MIT, has implemented a method of operating a memory element using the spin properties of elements without any power consumption. The results of this study, in which magnetic domain wall motion using spin waves was confirmed for the first time, were published on January 31, 2017, in *Nature Physics*, the leading scientific journal in the field of physics.

Global research has been actively conducted on the

structure of magnetic domain walls, which separate magnetic domains with different magnetic forces, in order to apply them to next-generation memory elements. This structure is attractive because it has a high degree of mobility and stability, and is inexpensive to process. However, due to the critical current consumed to move a magnetic domain, methods developed so far have failed to present any advantages over existing electronic elements. Many studies have looked for ways to lower the critical current, but until now, a solution had not been found.

The KIST-MIT study took a completely different approach and shattered the preconceived notion that magnetic domain walls must be moved using electrical means. The research team demonstrated that an efficient magnetic domain wall motion could be achieved, with absolutely no consumption of electric power, by using spin waves (or magnons), a unique type of wave in a spin caused by collision of two magnetic domain walls. The team produced zero-power elements by changing the status of magnetic domain walls without introducing an electrical current from an external source. Dr. WOO reflected on the implications of the study by saying, “Under today’s circumstances, where the amount of information that needs to be processed by a single smart device is increasing exponentially, using ultra-low power consumption has become a major issue. Amidst this situation, the new approach of using spin elements, as proposed in our study, is expected to greatly contribute to the advancement of industries involved in manufacturing next-generation memory elements.”

SmartFarm 2.0: Technology Development for Precision Farming

Dr. Ju Won NOH

Convergence Research Center for Smart Farm Solutions

The globally popular movie *Interstellar* dealt with the topic of worldwide food shortages caused by damage from yellow dust and agricultural pests. The movie *The Martian* depicted the potential for cultivation of potatoes at a Martian base. Though presented as science fiction, the premises of both these movies are increasingly plausible and have raised awareness among the general public on the need to develop crop cultivation technologies through precision environmental controls in response to anticipated changes in the Earth’s environment. Meanwhile, it is estimated that the global population will grow by 20% over the next 30 years, from the current 7.5 billion to approximately 9 billion in 2050. Scientists remain skeptical as to whether it will be possible to adequately meet the growing demand for food. How then can a food crisis be averted? The answer is that agriculture must be part of the 4th industrial revolution. Scientists stress that “smart farms,” based on artificial intelligence and big data, will be the only viable option for future agriculture to keep pace with demand.

A smart farm is a farm that combines agriculture with information communication technology (ICT) to provide for automatic management of crops. Using Internet of Things (IoT) technology, temperature, humidity, sunlight, carbon dioxide, and soil moisture are measured, and control devices are operated based on the results of analysis to create optimal growing environments. Advanced agricultural economies such as the United States, Canada, Japan, Australia and the Netherlands, among others, are achieving massive ripple effects through the convergence of artificial intelligence

technologies with agriculture.

According to research reports, the domestic ICT convergence market for protected horticulture, despite being at a technological disadvantage compared to products from advanced agricultural economies, has already entered the competition and market expansion phase. It has been reported that the market may enter the growth phase within several years. In keeping with the growth and maturation of related markets in the future, there is an urgent need for R&D aimed at improving domestic products’ competitiveness against foreign products for the sake

of domestic use as well as exports overseas.

Previous research and development has led to advances in simple assembly and production technologies in the domestic sensor and hybrid environmental control sectors. However, improved precision and durability of commercialized sensor/hybrid environmental control technologies and the development of appropriate software are needed to compete with integrated control systems such as that offered by PRIVA of the Netherlands. In other words, the development of data-based growth management technologies and linkages with integrated growth data utilization systems will be critical in responding to future requirements of the agricultural industry.

KIST’s Convergence Research Center for Smart Farm Solutions was established in October 2015 within the Natural Products Research Center at the KIST Gangneung Institute. The aim of our smart farm research is to improve Korean agricultural productivity to the level of the Netherlands and boost the global competitiveness of domestic agricultural producers. With support from the National Research Council of Science and Technology (NST) of the Ministry of Science, ICT and Future Planning,



Photo 1 Smart Farm, KIST Gangneung, Institute of Natural Products.

the center is engaged in research for development of integrated solutions for commercialization of smart farm technology in cooperation with five government-sponsored research institutes: KIST, the Electronics and Telecommunications Research Institute (ETRI), the Korea Institute of Industrial Technology (KITECH), the Korea Institute of Energy Research (KIER), and the Korea Food Research Institute (KFRI). The first-phase objective of the center's smart farm research is to enhance agricultural convenience through automation and remote management, but the core program, known as the "Smart Farm 2.0 Project" involves the development of intelligent growth management solutions which boost the quality and

productivity of agricultural produce. To this end, sensor and network-based data is being acquired and analyzed for tomatoes, hot peppers, strawberries, and other crops which are currently the highest income-generating crops in Korea. The data will then be used to implement optimal growth environment control systems. The center is currently engaged in protocol development and verification tests on five test farms in four regions, including at the KIST Gangneung Institute, to acquire growth environment data that will allow for scientific projections of optimal temperature, humidity and propagation conditions for a given crop, as well as factors for the prevention of damage from disease and pests, Research at the center is

focused on six areas of development: (1) systems for acquiring and analyzing crop data leading to models for predicting crop growth; (2) open hybrid environmental control systems using crop growth data; (3) work management systems; (4) optimized energy management systems; (5) agricultural data utilization systems; and (6) business models for the commercialization of smart farm technologies.

Systems developed to acquire, analyze and model crop growth make use of technologies that enable systematic acquisition of data from the field, analysis, and utilization of conventional, non-systematic growth data. Apps developed for smart phones save field data and also include basic statistical functions



Photo 2 General workshop of the Convergence Research Center for Smart Farm Solutions. December 20, 2016.

which can compare current growth with previous data or growth at other farms (Photo 2). The technologies are also able to carry out precision image analysis to obtain accurate growth data. The results are reflected in a crop growth model used to predict production (Figure 1). To do this, the crop growth model is engineered using methods that predict future production based on current circumstances by applying the data for current crops to the growth model developed from previous crop analysis. It must be noted that there is not enough data yet available on protected horticulture to develop an accurate model. However, as more data is collected and analyzed from farms during the course of our research, the accuracy of the crop

growth model will substantially improve.

Real-time instrumentation sensors and a standards-based open hybrid environmental control system allow for the development of growth models appropriate to each step of cultivation, from germination to harvesting. The complex environment in the greenhouse can be monitored and controlled to provide optimal environments for crop growth. This system also provides a hybrid environmental control platform tailored for the greenhouse environment and a standards-based communication protocol for improved reliability and compatibility of the hybrid environmental control system. By maximizing crop growth, this system

is expected to reduce imports and contribute to the creation of new overseas markets (Figure 2).

Implementation of a smart farm energy operation and management system (GH-EMS) and development of a simulator for optimal engineering of the heat supply are in progress. The center is conducting research on the thermal environment in greenhouses and identifying ways to improve productivity and save energy as a result of these studies (Figure 3).

The center has also developed and is using unmanned transport modules and cleaning/demotion machines. Other developments in progress include smart work management systems that measure and analyze worker efficiency. Early

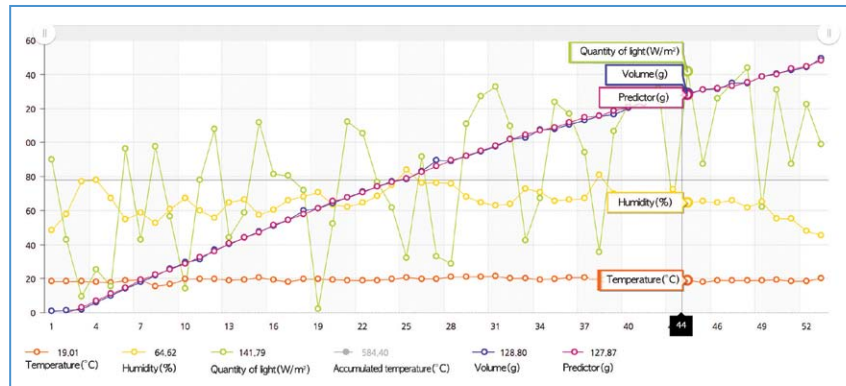


Figure 1 Fruit volume prediction model.

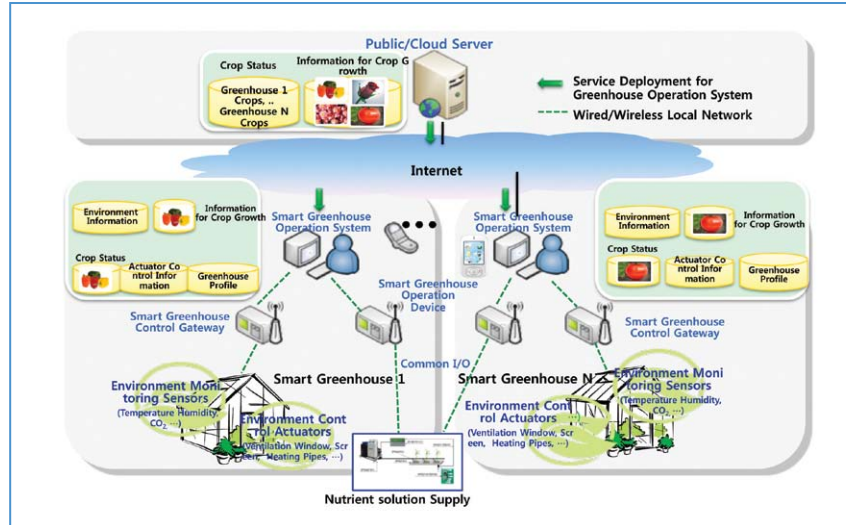


Figure 2 Hybrid environmental control system.

results suggest that these systems can generate savings of 30% or higher in labor costs. Research and development is also underway for equipment and procedures for evaluation of the precision and durability of greenhouse sensors (Figure 4).

Technology is being developed that helps farm managers determine the best strategies for harvesting and shipment. This technology

analyzes big data on prices, weather conditions, and quality, all of which are prone to sudden fluctuations during the cultivation-production-distribution process (Figure 5). The center plans to develop programs to monitor environmental/growth/quality data generated from cultivation to distribution of crops alongside quality indexes to determine the best time to release crops and effective ways to build

a distribution management system following harvest.

The center intends to use commercialized versions of already-developed smart farm solutions to expand and firmly establish smart farms domestically. This will be followed by efforts to introduce these solutions to overseas markets. Development of next-generation smart farm models using functional crops is also underway.

Although greenhouses covering areas of at least 3,300 m² to 10,000 m² are considered ideal for a smart farm operation, farms with smaller vinyl greenhouses account for almost 80% of all greenhouses in Korea. In response, the center is developing models for use with these smaller greenhouses.

The center's achievements are expected to go beyond just research and development. Our efforts are designed to bring about commercialization of smart farm technology to improve farm income and boost the global competitiveness of agricultural industries. We are also working to overcome current limitations in agricultural production through the development of commercial systems and the standardization of smart farm technology. The end result is expected to be the development of a new agricultural ecosystem comprising not only production but distribution and consumption as well.

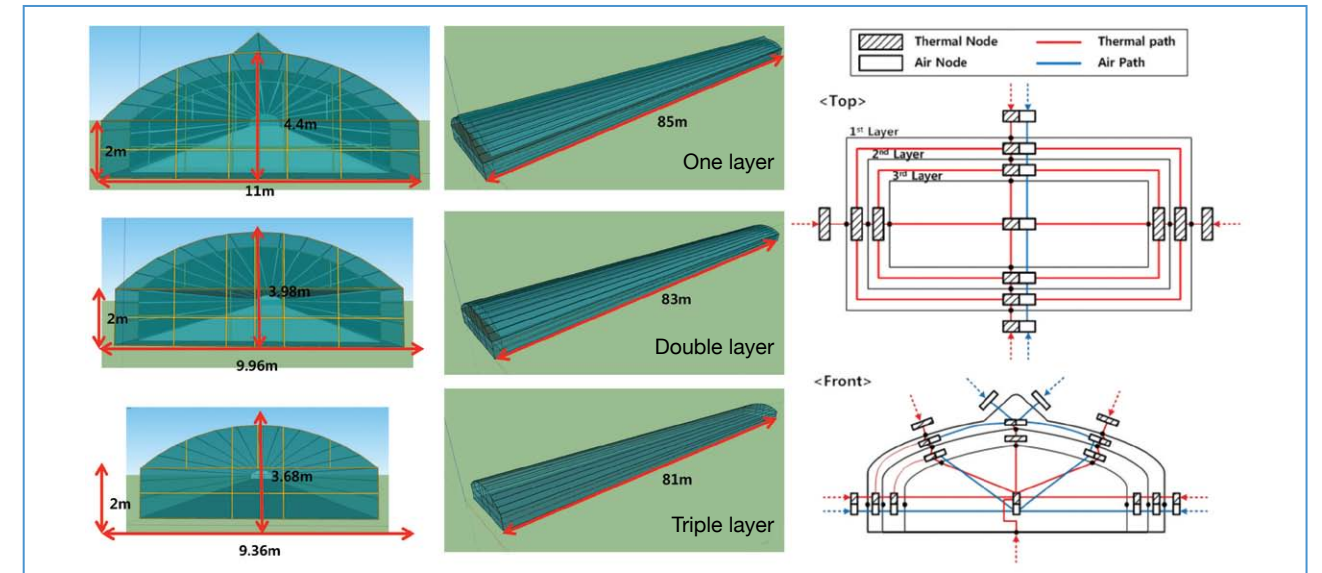


Figure 3 Thermal environment control and analysis for a three-layer greenhouse.



Figure 4 Transport robot for greenhouses.

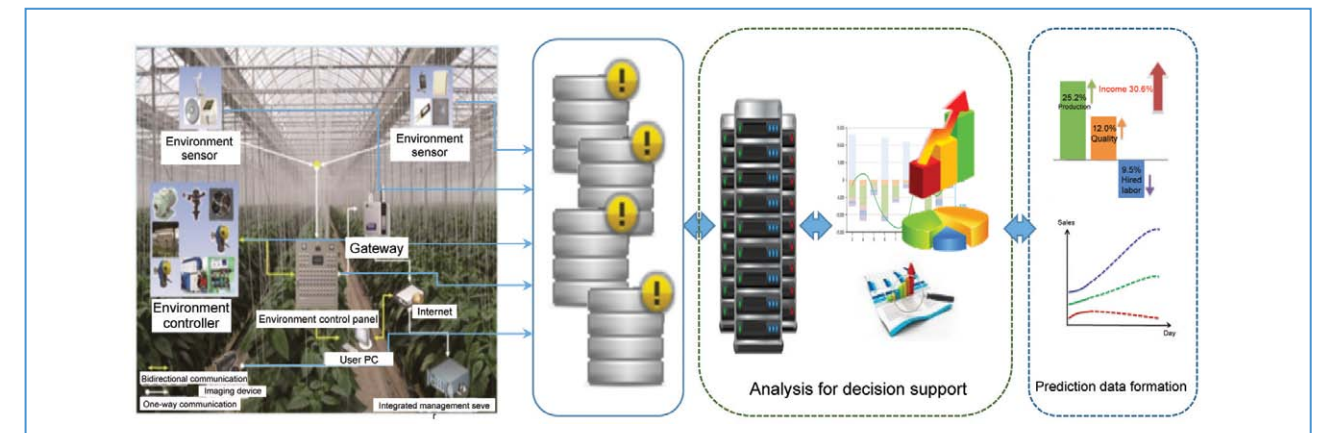
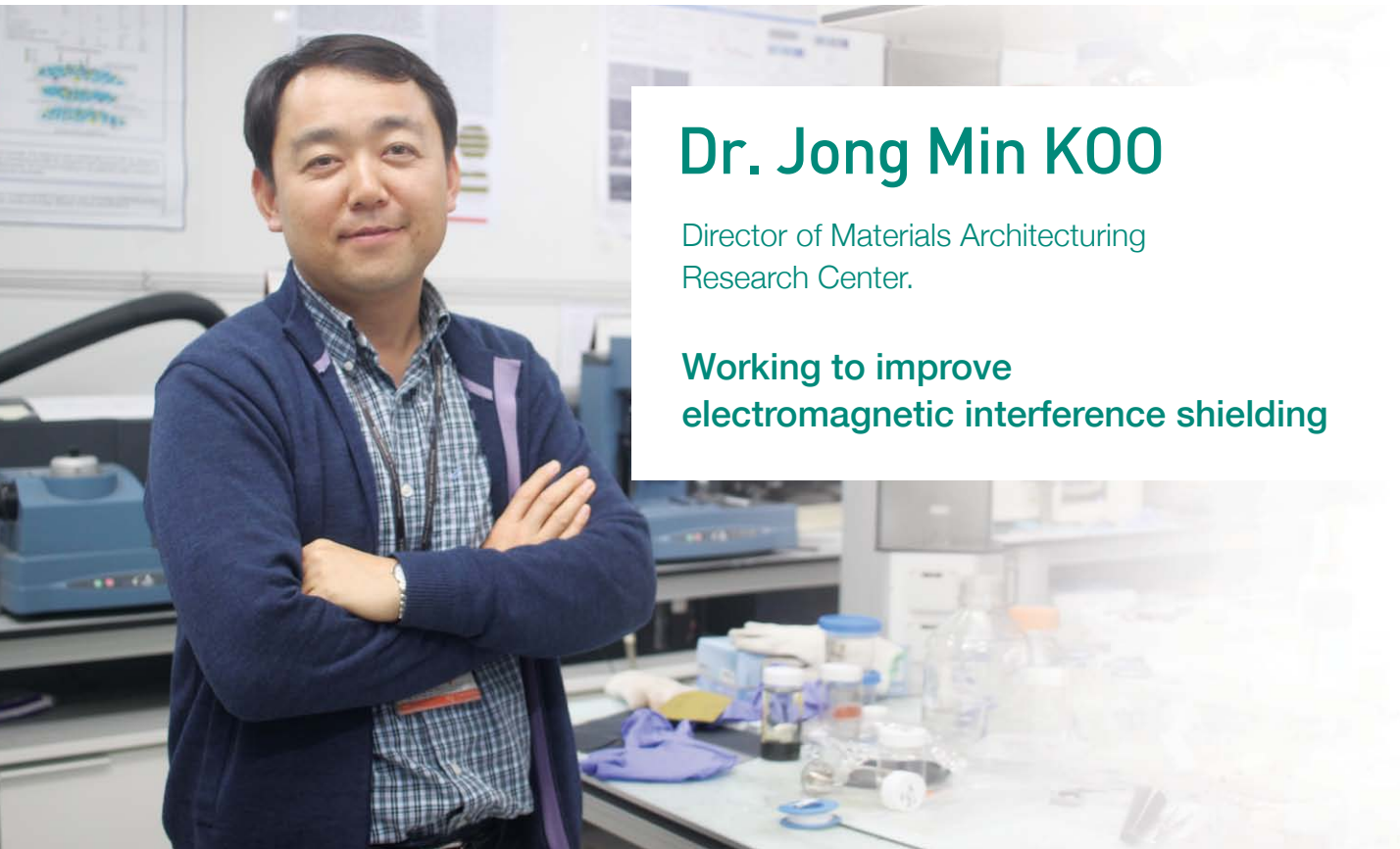


Figure 5 Smart farm information utilization system.



Dr. Jong Min KOO

Director of Materials Architecturing
Research Center.

Working to improve
electromagnetic interference shielding

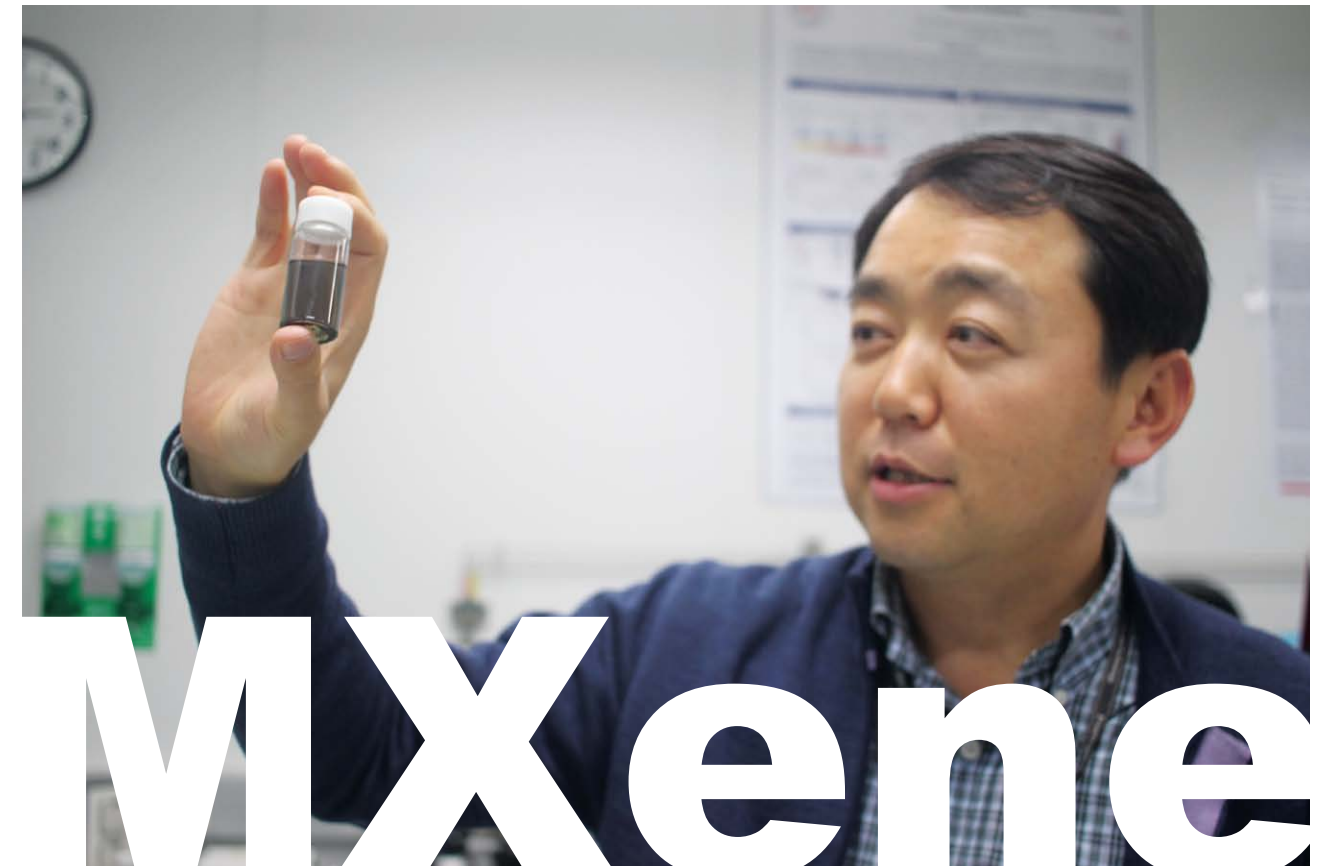
The growing problem of electromagnetic interference

On July 17, 1996, Trans World Airlines flight 800, en route from New York's John F. Kennedy International Airport to Paris, crashed into the Atlantic Ocean off the coast of Long Island, resulting in the deaths of all 230 aboard.

Subsequent investigation narrowed the possible causes of the accident to structural failure, a missile or explosive device, or the explosion of a fuel-air mixture inside the central fuel tank next to the wings. However, experts raised the possibility that mechanical malfunction

due to electromagnetic interference was the cause, an opinion that raised much controversy at the time.

Electromagnetic interference is invisible, but is a phenomenon that can happen at any time in the components of electronic products. This threat is caused by unnecessary electromagnetic signals or electrical noise from one device that can negatively affect, or even shut down, another device or system. As the number of electronic devices multiplies, it is increasingly likely that malfunctions caused by electromagnetic interference among mobile phones, laptop computers, and our many other devices will occur.



Electromagnetic interference is suspected as being the cause of numerous accidents, including the September 1998 Swiss Air crash which killed 229 and the Egypt Air crash of October 1999 that killed 217. Incidents other than air traffic accidents include cases involving automobiles and the malfunction of military weapons.

Electromagnetic waves can also have harmful effects on humans. The World Health Organization (WHO) has classified electromagnetic radiation as a cause of cancer and recommends minimal exposure to electromagnetic radiation. Exposure to electromagnetic interference (EMI) is inevitable today given the large number of electronic devices we use on a daily basis. One scientist

who is engaged in research and development to deal with this problem is Dr. Jong Min Koo, head of KIST's Center for Materials Architecturing.

According to Dr. Koo, research and development in EMI shielding materials is critical at this time because, "We use large numbers of electronic appliances. High density integration and the reduction in the size and thickness of electronic appliances lead to the integration of large numbers of devices in a single appliance, thus increasing the problem of electromagnetic interference."

The search to improve conventional EMI shielding materials

EMI shielding isn't a new technology. However, conventional technologies require supplementation. Metals such as silver or copper are conventionally used, but these are dense, expensive to manufacture, heavy, and prone to corrosion. Another disadvantage is the difficulty of manipulating these materials, thus limiting their utility in next-generation mobile electronic and communication appliances.

A material recently developed by Dr. KOO and his team is designed to resolve these issues. It has outstanding electrical conductivity and workability, but remains light and inexpensive to produce. The material is composed of a metal-free polymer complex utilizing a transition metal carbide known as "MXene." It represents a significant improvement over previous shielding materials and has attracted considerable attention due to its outstanding electrical conductivity and workability, light weight and low cost.

The material is multi-layered with a structure similar to that of graphite. It has a two-dimensional lamellar structure comprised of carbon (C) atoms as well as atoms of a heavy metal such as titanium (Ti). It has a thickness of 1 nanometer and a length of a few micrometers.

"To turn MXene into an EMI shielding material, it was necessary to make it into a polymer complex and work it into the desired shape. The problem was that it was highly likely that we would lose the good properties

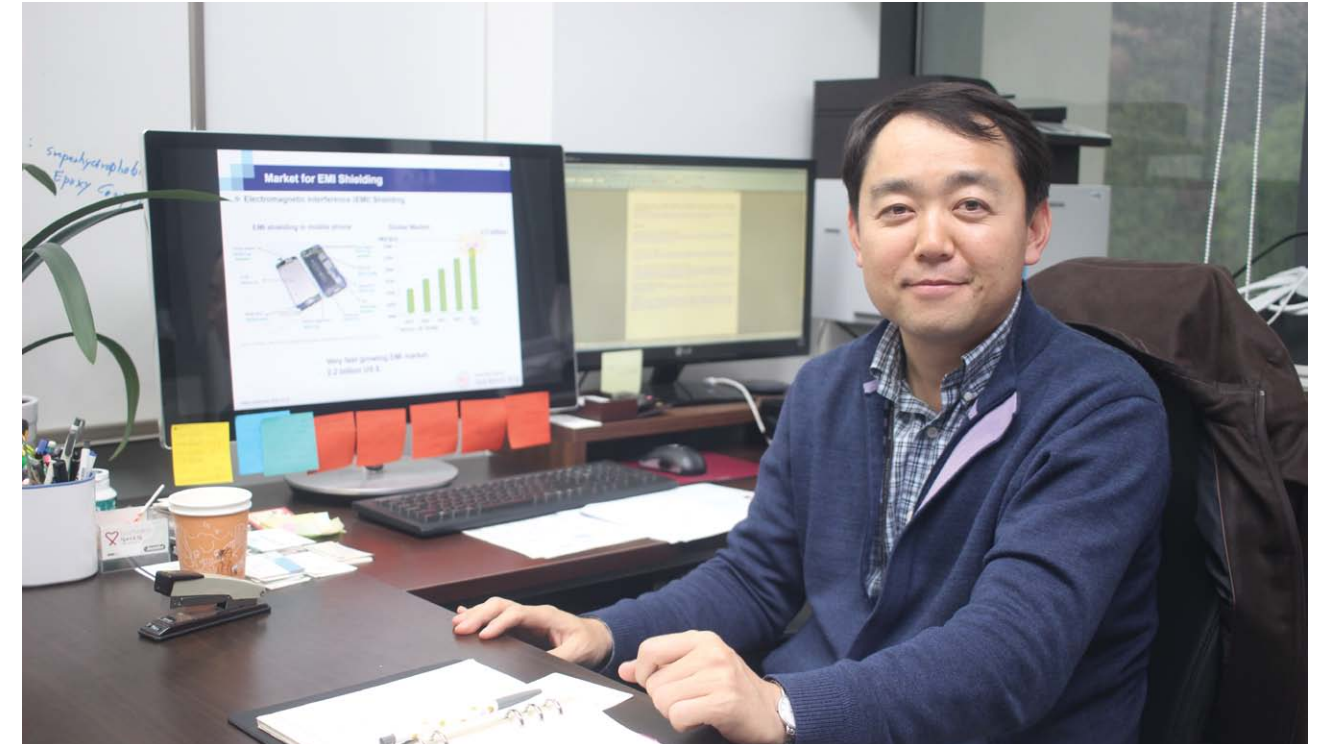
of MXene. It was key to choose a polymer that goes well with MXene, and luckily enough, we were able to find just the one. You could say we got lucky with the single most challenging problem facing our research."

Every research and development task has its challenges. Choosing a suitable for processing MXene into an EMI shielding material proved especially difficult for the team. The problem was to select a polymer capable of creating a polymer complex that would retain the electrical conductivity of MXene. The choice needed to be made carefully, as selecting a polymer that was not compatible with MXene could potentially cause its advantageous properties to deteriorate.

"We made many attempts to select the right polymer. It was a very demanding task, but fortunately, we were able to produce a complex with optimal workability properties using a polymer (sodium alginate) which was both environmentally friendly and easy to machine. It was a difficult task that we were able to overcome with a bit of good luck."

Dr. KOO's shielding material can be produced through a more convenient and inexpensive manufacturing process than other nanomaterials. Comprised of large numbers of hydrophilic groups (atomic groups characterized by high affinity with water) on the surface, it is easy to dissolve in solvent and form into a polymer complex. Its superior electrical

MXene



conductivity is a property advantageous to its application in various film and coating products where electrical conductivity is a requirement.

The team has confirmed that the developed material exhibits superior EMI shielding properties even when reduced to extremely narrow thicknesses. This allows for shaping of the material into various films, and it can also be used in various coating applications such as spin coating and spray coating, a substantial advantage in successful commercialization of the material.

The technology is being readied for transfer to corporations for commercialization. While a challenge in itself and involving many difficult issues, commercialization of the technology is expected in the not-too-distant future. In describing the process, Dr.

KOO explained, "As this is an applied EMI shielding technology consisting of the production and use of a new type of nanomaterial, we will need new manufacturing processes and the installation of new equipment. This means that corporations will play a large role in the technology's commercialization, and we will, accordingly, dedicate our efforts toward collaborating with these companies in follow-up research for commercialization."

The study was conducted jointly with a team led by Dr. Yury GOGOTSI at Drexel University in the United States. The results of the research project were published in the online version of *Science* on September 9, 2016.

Future directions for the Center for Materials Architecturing

Dr. KOO was appointed head of the Center for Materials Architecturing in March of this year. The center works primarily on developing plural and multi-dimensional convergence materials to overcome structural and functional limitations. Researchers in the fields of polymers, ceramics, and metals work together to develop next-generation devices through dimension control, size control, and functional group control for each material.

As the center is engaged in developing next-generation devices, most of the studies conducted are basic research and upstream studies. Although the center focuses more on long-term research than short-term results, the ripple effects of a single achievement are often far-reaching.

Some of the more influential achievements of the center include the development of a MXene device by Dr. KOO and his team, development by the team of Dr. Heon Pil HA of the world's first low-temperature denitrification catalyst for ship engines, and technology transfers for an environmental catalyst for exhaust emissions and air purification, an LED packaging material, polymer pattern materials, and a polymer electrolyte material.

The center plans to engage in the study of 4U (ultra-light, ultra-strong, ultra-electrical conductive, ultra-thermal conductive) composite materials. In multiple interviews with the press in March, President Byung Gwon LEE, of KIST announced plans to increase the amount of weight the institute places on 4U research.

In response to this policy, Dr. KOO commented, "Our center is at the forefront of 4U composite materials research, an area stressed by the president." And he added, "We will focus on developing nanomaterials with high electrical and heat conductivity and the study of polymer composite using these materials."

In closing, Dr. KOO said, "While until now I have dedicated my efforts to enhancing my own research abilities, from now on I intend to work on improving our research abilities as a whole." Quoting the Turkish proverb, "If you want to go quickly, go alone. If you want to go far, go together," he expressed hopes that the center would carry out large research projects needed by the country as well as humanity in general. "We will apply ourselves to collaborative research tasks, national agenda research tasks, and research aimed at resolving problems suffered by humanity on a global scale."



Cover image :

Electromagnetic Interference Shielding with 2D Transition Metal Carbides

The 2D structure combined with high electrical conductivity and good electronic coupling between the layers are responsible for the extremely high EMI shielding efficiency of MXenes.

Editorial Information

Editor-in-Chief
Tae Hoon LIM

Editorial Board Members
Il Joo CHO
Bradley BAKER
Hyun Kwang SEOK
Hyung Jun KIM
Jong Ho LEE
Seok Won HONG
Young Soon UM
Eui Seong KIM
Gi Hong YEUM

Managing Editor
Jin Soo KIM
jinsoojs.kim@kist.re.kr
+82-2-958-6155
Web Address
www.kist.re.kr/en

English Advisory Services
Anne CHARLTON
The Final Word Editing
Services
the_final_word@live.com

KIST Korea Institute of
Science and Technology

5, Hwarang-ro 14-gil, Seongbuk-gu, Seoul 02792,
Republic of Korea
Tel +82-2-958-6039 www.kist.re.kr/en
E-mail jinsoojs.kim@kist.re.kr

KIST Gangneung Institute of Natural Products

Promoting Well-Being Through Natural Products

KIST Gangneung was established in May 2003 at the Gangneung Science Industrial Complex the purpose of nurturing specialized industries. We have taken an initiating role in the region's science and technology innovation and produced research outcomes including technology transfers, and patent.

The main goal of our institute is to become a leading global institute not only in the field of natural products research but also in agricultural research.

We will continue to support technology transfer to SMEs and promote commercialization of such technologies. In addition, as a national S&T institute, we will become the local think-tank that fosters excellent research manpower and spreads scientific culture through activities that will support S&T development in the Gangneung Region.

Focus Areas

- Development of plant growth regulation, modeling technology and large-scale production technology for medicinal plants
- Research on bioactive natural compounds, natural products diversity, and biological chemistry for secondary metabolites of living resources
- Mechanism study on biosynthesis and bioactivity of natural products
- Development of smart farm solutions and related HW/SW technology for sustainable horticulture

